

UW-Madison.  
SSEC Publication No.94.12.W2.

THE SCHWERDTFEGER LIBRARY  
1225 W. Dayton Street  
Madison, WI 53706

**Report to**

**Philips Laboratory  
United States Air Force  
Hanscom Air Force Base**

**For Grant F19628-91-K-0007**

**Radiative Characteristics of Clouds Measured From Satellites**

**for the period of 2 April, 1991 thru 30 November, 1994**

**Submitted by**

**Donald P. Wylie  
Principal Investigator**

**Space Science and Engineering Center  
at the University of Wisconsin-Madison  
1225 West Dayton Street  
Madison, WI 53706  
Phone: 608 263 7458  
Fax: 608 262 5974  
E-mail: donw@ssec.wisc.edu**

**December 1994**

Data collection has continued from both the polar orbiting NOAA satellites and the geostationary GOES satellite. The collection of these data and cloud analyses are done automatically on the McIDAS at the University of Wisconsin-Madison. Two analyses of these data have been completed in the last year which will be discussed in this report.

A paper summarizing the global cloud statistics entitled "Four Years of Global Cirrus Cloud Statistics Using HIRS" will be printed in the December, 1994, issue of the Journal of Climate. A draft of this paper is enclosed as Appendix A. The data collected and method of analysis are also discussed in that paper. The significant findings reported in this paper are:

- 1) Cirrus clouds are very common and were found in 42% of the satellite data. There are seasonal changes in the locations of the most frequent cirrus which follow seasonal changes in convective clouds. However, very thin cirrus occurred at least 10% of the time in all areas. The diurnal cycle of cirrus was very small over the oceans. The diurnal cycle of cirrus over land was found to follow the diurnal cycle convective clouds in a previous study using the GOES data.
- 2) A large increase in cirrus and high cloud cover was found in 1991. This cloud cover increase appeared with the strong El Nino Southern Oscillation climatic event. A volcanic eruption also occurred in 1991 which may have enhanced this cloud cover change. It should be noted that the total cloud cover of all cloud forms did not change during this period. Cloud free observations continued to be 23% of the data before and after the high cloud change.

Summaries of these cloud data have been given to Al Boehm of STC and to Ian Robinson and Donald Rudy of the Aerospace Corporation for their studies of cloud cover. Their analyses of these data were published in Aerospace Report No. ATR-94(8019-1), "Frequency of Cloud Cover at Altitude: Implications for Surveillance Systems" by Robinson, Rudy and Gonzalez. A copy of that report is included in Appendix B.

A comparison of our cloud data is also being made to two other satellite cloud climatologies with similar and complementary information. The International Satellite Cloud Climatology Project (ISCCP) has compared their cloud statistics to ours. A paper is being drafted by a NASA group on this comparison. The conclusions will be that we find similar geographical distributions of cirrus along with similar seasonal changes. However, the frequency of cirrus and other cloud forms are less in the ISCCP analysis than ours.

A comparison with the Stratospheric Aerosol and Gas Experiment (SAGE) cloud data is being made. The first results show similar frequencies of high clouds in both data sets.

We have compared our satellite data to lidar observations of clouds. A paper describing the first results of this comparison is included in Appendix C. It shows that the optical depth calculations from satellite infrared data agree with similar optical depths measured in visible wavelengths by the lidar. This study also found the cloud height calculated from the CO2 Slicing Algorithm represents indicates the denser part of semi-transparent cirrus clouds rather than the height of the cloud top. This cloud level is more useful for radiative transfer calculations than the cloud top height.

# Appendix A

## FOUR YEARS OF GLOBAL CIRRUS CLOUD STATISTICS USING HIRS

Donald P. Wylie

Space Science and Engineering Center  
University of Wisconsin-Madison

W. Paul Menzel and Harold M. Woolf  
Satellite Applications Laboratory

NOAA/NESDIS

Madison, Wisconsin 53706

Kathleen I. Strabala

Space Science and Engineering Center  
University of Wisconsin-Madison

submitted July 1993

revised January 1994

## Abstract

Trends in global upper tropospheric transmissive cirrus cloud cover are beginning to emerge from a four year cloud climatology using NOAA polar orbiting HIRS multispectral infrared data. Cloud occurrence, height, and effective emissivity are determined with the CO<sub>2</sub> slicing technique on the four years of data (June 1989 - May 1993). There is a global preponderance of transmissive high clouds, 42% on the average; about three fourths of these are above 500 hPa and presumed to be cirrus. In the ITCZ a high frequency of cirrus (greater than 50%) is found at all times; a modest seasonal movement tracks the sun. Large seasonal changes in cloud cover occur over the oceans in the storm belts at mid-latitudes; the concentrations of these clouds migrate north and south with the seasons following the progressions of the subtropical highs (anticyclones). More cirrus is found in the summer than in the winter in each hemisphere.

A significant change in cirrus cloud cover occurs in 1991, the third year of the study. Cirrus observations increase from 35% to 43% of the data, a change of 8 percentage points. Other cloud forms, opaque to terrestrial radiation, decrease by nearly the same amount. Most of the increase is thinner cirrus with infrared optical depths below 0.7. The increase in cirrus happens at the same time as the 1991-92 El Nino/Southern Oscillation (ENSO) and the eruption of Mt. Pinatubo. The cirrus changes occur at the start of the ENSO and persist into 1993 in contrast to other climatic indicators which return to near pre-ENSO and volcanic levels in 1993.

## 1. Introduction

Cirrus clouds are crucially important to global radiative processes and the thermal balance of the Earth; they allow solar heating while reducing infrared radiation cooling to space. Models of climate changes must simulate these clouds correctly to account for radiometric effects properly in the Earth's energy budget. Past estimates of the variation of cloud cover and the Earth's outgoing longwave radiation have been derived primarily from longwave infrared window (10-12 microns) radiances observed from polar orbiting and geostationary satellites (Rossow and Lacis, 1990; Gruber and Chen, 1988; Stowe et al., 1988). The occurrence of transmissive clouds has been under-estimated in these single band approaches. Recently, multispectral techniques have been used to better detect cirrus in global (Wu and Susskind, 1990) and North American (Wylie and Menzel, 1989; Menzel et al., 1992) cloud studies.

This paper reports on the investigation of seasonal changes in semi-transparent or cirrus global cloud cover with multispectral observations from polar orbiting HIRS (High resolution Infrared Radiation Sounder). Clouds partially transparent to terrestrial radiation are separated from opaque clouds in four year statistics of cloud cover (Wylie and Menzel, 1989). Transmissive or cirrus clouds are found in roughly 40% of all satellite observations.

The HIRS observations in the carbon dioxide absorption band at 15 microns are used to calculate these cloud statistics. The CO<sub>2</sub> slicing algorithm calculates both cloud top pressure and effective emissivity from radiative transfer principles. Various CO<sub>2</sub> algorithms have been described in the literature (Chahine, 1974; Smith et al., 1974; McCleese and Wilson, 1976; Smith and Platt, 1978; Wielicki and Coakley, 1981; Menzel et al., 1983) and applications to data from the geostationary sounder VAS (VISSR Atmospheric

Sounder) and the polar orbiting sounder HIRS have been published (Wylie and Menzel, 1989; Menzel et al., 1986; Susskind et al., 1987; Menzel et al., 1989; Eyre and Menzel, 1989).

## 2. Technique

Cirrus clouds often appear warmer in the infrared window band than the ambient air temperature at their altitude because they are transmitting radiation from below. This occurs in more than 40% of the satellite data, of which roughly half is often misinterpreted as lower non-cirrus clouds. The CO<sub>2</sub> slicing technique is capable of correctly identifying most of these clouds. Using the HIRS infrared bands with partial CO<sub>2</sub> absorption, cloud top pressure and effective emissivity are calculated for each observational area. CO<sub>2</sub> slicing does not estimate cloud base pressure. Partially transmissive clouds are distinguished during daylight and night over water and land. The description of the technique and details of its application with HIRS data are presented in Menzel et al. (1986 and 1989) and are repeated in Appendix A of this paper; there are similarities to the application with VAS data described in Wylie and Menzel (1989).

Effective emissivity refers to the product of the fractional cloud cover,  $N$ , and the cloud emissivity,  $\epsilon$ , for each observational area (roughly 20 km by 20 km). When  $N\epsilon$  is less than unity, HIRS may be observing broken cloud ( $N < 1$ ,  $\epsilon = 1$ ), overcast transmissive cloud ( $N = 1$ ,  $\epsilon < 1$ ), or broken transmissive cloud ( $N < 1$ ,  $\epsilon < 1$ ). All of these possibilities imply an observation where the HIRS radiometer detects radiation from below a cloud layer as well as radiation from the cloud layer top. All observations where the effective emissivity is less than 0.95 are labelled as "cirrus" in this

paper. Effective emissivity observations greater than 0.95 are considered to be opaque clouds.

Cirrus usually are transmissive and exhibit spatial variations at scales ranging from hundreds of kilometers to smaller than the field of view (FOV) of the instrument. The assumption is that more of the semi-transparency for a given field of view is due to cloud emissivity being less than one than due to the cloud not completely covering the field of view. Comparison of Advanced Very High Resolution Radiometer (AVHRR) one kilometer resolution cloud data and HIRS 20 kilometer resolution cloud effective emissivity determinations supports this. For effective emissivity determinations greater than 0.50, almost all of the variation from one FOV to another is caused by changes in emissivity and not cloud fraction. For effective emissivities less than 0.50, most of the variation is still being caused by changes in cloud emissivity fraction but some is now being caused by changes in cloud fraction. Appendix B presents this comparison. Thus for most synoptic regimes, especially in the tropics and subtropics, this assumption appears reasonable and it is supported in the literature (Wielicki and Parker, 1992; Baum et al., 1992).

In multiple cloud layers, the technique is limited to finding the height of only the highest cloud layer. Multiple layers often can be inferred from inspection of neighboring pixels where holes in the upper layer occur. Comparison to cloud reports from ground observers indicate that 50% of the time when the CO<sub>2</sub> technique detects an upper tropospheric cloud, one or more lower cloud layers also is present (Menzel and Strabala, 1989). When an opaque cloud underlies a transmissive cloud, the height of the transmissive cloud is estimated to be too low by as much as 100 hPa (Menzel et al., 1992). The largest error occurs when the underlying opaque layer is in the middle troposphere (400-700 hPa) and the upper cirrus layer is very thin. The error

is small when the opaque cloud is near the surface or close to the upper transmissive layer. The error in effective emissivity of the transmissive cloud increases as the opaque layer approaches the transmissive layer; when they are coincident the effective emissivity is set to one.

The processing procedure is briefly outlined here. More details are given in Appendix A. CO<sub>2</sub> slicing cloud top pressures are calculated when the cloud forcing (clear minus cloudy radiance is greater than five times the instrument noise level); otherwise the infrared window temperature is used to determine an opaque cloud top pressure. Fields of view are determined to be clear if the moisture corrected 11.1 micron brightness temperature is within 2.5 C of the known surface temperature (over land this is inferred from the NMC Medium Range Forecast (MRF) model analysis; over the oceans this is the NOAA NESDIS sea surface temperature analysis).

In this four year study, HIRS data from NOAA 10, 11, and 12 are sampled to include only data from every third FOV on every third line with zenith angle less than 10 degrees. With two satellites, about one half of the Earth is sampled each day. Morning orbits over land are rejected from the data because a good guess of the morning land surface temperature is unavailable and therefore discerning cloudy from clear FOVs is difficult. In the Arctic and Antarctic, the HIRS bands are inspected for the presence of surface temperature inversions which are assumed to be indicators of clear sky.

### 3. Global Cloud Statistics

A statistical summary of over 15 million cloud observations from HIRS between June 1989 through May 1993 is shown in Table 1. High clouds above 400 hPa comprise 24% of the observations. 27% of the observations are of clouds between 400 hPa and 700 hPa. Low clouds below 700 hPa are found 26% of the



time. Cloud free conditions are found 23% of the time. Cirrus and transmissive clouds (with effective emissivities less than 0.95) are found in 42% of our observations; they range from 100 to 800 hPa. The 12% transmissive observations below 500 hPa are most likely broken clouds. Clouds opaque to infrared radiation (with effective emissivities greater than 0.95) are found 35% of the time. The global average cloud effective emissivity (global average of  $N\epsilon$ ) is found to be 0.54; Warren et al. (1988) report a global cloud fraction of 0.61 from ground observations.

The frequency of different cloud observations is used to indicate the probability that a given HIRS field of view is found to contain a certain type of cloud. The frequency of all clouds over land is 67% versus 79% over ocean; the frequency of cirrus clouds over land is 39% versus 43% over ocean. High clouds above 500 hPa prefer land over ocean (37% versus 34%). Thin clouds ( $N\epsilon < 0.50$  or infrared optical depth  $\tau < 0.7$ ) prefer ocean over land (22% versus 18%).

As the satellite views from above the atmosphere, high clouds are found in preference to low clouds. Broken low cloud fields are reported as opaque low clouds because the CO<sub>2</sub> slicing technique is unable to estimate the cloud fraction below the sensitivity peaks in the CO<sub>2</sub> bands. Transmissive clouds cover the range of effective emissivities from 0.0 to 0.95 fairly uniformly.

The CO<sub>2</sub> slicing technique is subject to some errors that have been discussed in Menzel et al. (1992). The large observation area (20 km by 20 km) produces results where transmissive cloud observations are over-estimated; cloud edges and clear sky within a FOV are incorrectly estimated to be transmissive cloud in roughly 5% of the FOVs. Conversely, the HIRS lack of sensitivity to very thin clouds in roughly 5% of the FOVs causes transmissive clouds to be incorrectly classified as lower opaque clouds (Wylie and Menzel,

1989). And finally, the top down view of the satellite reveals high clouds in preference to lower occluded clouds. These errors are largely offsetting. Overall, the frequency of clear sky observations in Table 1 is believed to be valid within 3%.

A similar multispectral analysis of transmissive clouds was previously published for continental United States using GOES/VAS data (Wylie and Menzel, 1989; Menzel et al., 1992). A comparison of the CO<sub>2</sub> slicing analysis of coincident data from both the GOES/VAS and NOAA/HIRS is shown in Appendix C. The two analyses find similar frequency of clear sky. However, the HIRS data produce more transmissive cloud observations than the VAS. We suspect that these differences appear because the radiance noise of the HIRS is less than that of the VAS and hence HIRS cloud parameters for thin clouds will be determined more often from CO<sub>2</sub> slicing and less often from the infrared window. When observed and clear FOV radiance observations differ by less than five times the noise in the radiometric measurements, low opaque clouds are inferred. The smaller radiometric noise of the HIRS allows it to produce CO<sub>2</sub> slicing solutions for thin clouds more consistently. In addition the larger HIRS FOV reduces the ability of the HIRS to find breaks or holes in the upper level cloud fields. The VAS with a smaller FOV is able to report more of these holes whereas the HIRS averages them in with the cloud field. These two differences would cause the HIRS to indicate more transmissive cloud than the VAS.

Comparison with the results of the International Satellite Cloud Climatology Project (ISCCP) reveal that this HIRS multispectral analysis is finding roughly twice as many transmissive clouds than the ISCCP visible and infrared window analysis. Jin and Rossow (1994) studied collocated ISCCP and HIRS results for four months (July 1989, October 1989, January 1990, and April

1990); HIRS finds 76% cloud cover (80% over water and 65% over land) while ISSCP finds 63% cloud cover (68% over water and 51% over land). Most of this difference is attributed to HIRS detection of optically thin clouds (infrared optical depth less than 0.7); HIRS finds 17% while ISSCP finds only 7%. However HIRS finds about 3% less low opaque cloud than ISSCP (22% versus 25% respectively). Hartmann et al. (1992) present one year (March 1985 -February 1986) of ISSCP data and find semi-transparent cloud (visible optical depth less than 9.4 which corresponds roughly to infrared optical depth less than 4.7) 21% of the time; HIRS finds 42% in the four years of this study (June 1989 - May 1993). HIRS finds twice as much semi-transparent cloud than ISSCP high in the atmosphere (21% to 10% respectively) and at mid-levels (21% to 11% respectively). HIRS finds less opaque cloud at high and middle levels above 700 hPa than ISSCP (10% to 15% respectively), but the low cloud detection is comparable (25% to 26% respectively). HIRS finds less clear sky in the four years than the one year of ISSCP that Hartmann et al. (1992) studied (23% to 36% respectively). Both of these comparisons point to the ISSCP difficulty in detecting thin transmissive clouds; if one were to exclude clouds with infrared optical depths less than 0.7 from the HIRS data (roughly 20% of the observations) and increase the frequency of low opaque clouds in the HIRS data (adding roughly 5%), all adjusted HIRS cloud categories would agree with Jin and Rossow (1994) and Hartmann et al. (1992) to within a few percent.

#### 4. Seasonal and Geographical Trends

Table 2 presents the seasonal variation of clouds by classifications of clear sky, thin clouds ( $N\epsilon < 0.5$ ), thick clouds ( $0.5 < N\epsilon < 0.95$ ), and opaque clouds ( $N\epsilon > 0.95$ ) and by height categories of high (cloud pressure less than 400 hPa), middle (cloud pressure between 400 and 700 hPa), and low (cloud

pressure greater than 700 hPa). The all season four year summary is also included for comparison. Little variation is found in the global boreal summer versus winter cloud statistics. A few percent more cirrus and less clear sky are found in the boreal winter. Hartmann et al. (1992) report similar seasonal statistical differences.

Figure 1 shows the geographical distribution of cirrus clouds in the summer and winter seasons (darker regions indicate more frequent cloud occurrence). The months of December, January, and February were summarized for the boreal winter (austral summer) and the months of June, July, and August were used for the boreal summer (austral winter). The seasonal summaries were compiled using a uniformly spaced grid of 2 degree latitude by 3 degree longitude. Each grid box for each season has at least 500 observations.

The major features of the four year summary have not changed appreciably from those reported in the two year summary (Wylie and Menzel, 1991). The Inter-Tropical Convergence Zone (ITCZ) is readily discernible as the region of more frequent cirrus (darker band in the tropics); the mid-latitude storm belts are also evident. The ITCZ is seen to move north with the sun. This seasonal migration is also apparent in the latitudinal summaries shown in Figure 2. The subtropical high pressure systems are seen in the region of less frequent cirrus cover (white band in the subtropics). Over the Indonesian region the ITCZ expands in latitudinal coverage from boreal winter to summer. In the central Pacific Ocean, the ITCZ shows both a southern and northern extension during the boreal winter months.

In the southern hemisphere, the eastern Pacific Ocean off South America and the eastern Atlantic Ocean off Africa remain relatively free of cirrus clouds throughout the year. The southern hemispheric storm belt is evident

throughout the year. In the northern hemisphere mid-latitude storm belts, the frequency of cirrus clouds increases during the winter with the strengthening of the Aleutian Low in the north Pacific Ocean and the Icelandic Low in the north Atlantic Ocean. The North American cirrus cloud cover shows little seasonal change, agreeing with a previous GOES/VAS analysis (Menzel et al., 1992). Large convective development occurs during the austral summer (boreal winter) in South America and Africa, which is readily apparent in the increased occurrence of high cirrus clouds.

A large seasonal change is found over Antarctica, where few clouds of any altitude are reported in the austral winter. The HIRS data do not show polar stratospheric clouds, which occur commonly over Antarctica in the months of June, July, and August. Polar stratospheric clouds apparently do not attenuate the HIRS bands sufficiently to mask out the strong inversions below them.

These seasonal changes in geographical distribution of global transmissive clouds are largely in agreement with the one year ISSCP results shown in Hartmann et al. (1992). The ITCZ expands in the Indonesian region in the boreal summer, the Icelandic low creates more cirrus in the boreal winter, convective development in South America and Africa is obvious in the austral summer, and the eastern Atlantic and Pacific Oceans in the southern hemisphere stay mostly free of cirrus clouds year round. As discussed previously, the ISSCP data indicate about half the transmissive clouds that the HIRS data does.

Upper tropospheric clouds (above 500 hPa) are discussed in the following paragraphs. Figure 2 shows the zonal distribution of high clouds, which includes both the transmissive and opaque clouds (30% and 5% of all observations respectively). The frequent occurrence of high clouds in the

ITCZ is prominent as the central maximum; the mid-latitude storm belts are evident in the secondary maxima. Seasonal shifts in the ITCZ are apparent over both land and ocean, as the ITCZ moves north and south with the sun. The frequency of high clouds over land increases strongly from the equator to 30 S during the austral summer. The main contributors are the Amazon Basin of South America and the Congo of Africa. The high clouds over the southern hemispheric storm belt, primarily over the oceans from 30 S to 70 S, remain constant throughout the year. The northern hemispheric land masses from 45 N to 65 N also show little seasonal change in high cloud cover. Jin and Rossow (1994) indicate that the HIRS zonal distribution of high cloud is in very good agreement with the ISSCP data, when clouds with infrared optical depth less than 0.7 are omitted from the HIRS data.

Light cirrus show smaller seasonal changes. The latitudinal distribution of thin transmissive ( $N_{\epsilon} < 0.5$  or infrared optical depth  $\tau < 0.7$ ) clouds over ocean and over land is shown in Figure 3. The occurrence is somewhat more likely over ocean; this disagrees with Warren et al. (1988) who found more cirrus over land than ocean in their ground based observations. A modest peak from 10 S to 10 N is evident both over land and ocean. Thin transmissive clouds appear globally with a frequency of 5 to 40%.

## 5. Trends in the Four Years

The progression of cloud cover from year 1 (June 1989 - May 1990) to year 2 (June 1990 - May 1991), from year 2 to year 3 (June 1991 - May 1992), and from year 3 to year 4 (June 1992 - May 1993), is shown in Table 3. Thin clouds refer to  $N_{\epsilon} < 0.5$  (infrared optical depth  $\tau < 0.7$ ), thick refers to  $0.5 < N_{\epsilon} < 0.95$  ( $0.7 < \tau < 3.0$ ). The change from year 1 to year 2 is imperceptible. The change from year 2 to year 3 is large and very obvious;

opaque clouds decrease by 7% and cirrus increases by 8%. Cirrus appears much more frequently in the year 3 data than in previous years; conversely opaque cloud appears much less frequently. The probability of clear sky remains stable. The change from year 3 to year 4 is small; cloud cover increases by approximately 3%.

The geographical distribution of the difference in the probability of cirrus occurring in the boreal summer of 1990 minus boreal summer 1989 is shown in Figure 4a (upper left panel). Differences greater than 12% are scattered about, with no discernible pattern. Coherent changes are apparent only in the Timor Sea off the northwest coast of Australia (where a decrease of cirrus occurs) and in the Pacific Ocean east of Papua New Guinea (where an increase of cirrus occurs). Figure 4b shows the corresponding difference for the boreal winters of 1990-91 minus 1989-90 (upper left panel). Again there is not very much difference. The only features are the increase of cirrus in the Coral and Timor Seas and the decrease of cirrus in the Indian Ocean west of Australia (representing a westward shift from Fig 4a).

A change in cirrus coverage in the summer of 1991 with respect to the summer of 1990 is obvious (Figure 4a upper right panel). Coherent increases of cirrus greater than 12% are apparent along the southern edge of the ITCZ, in the southern mid-latitudes, the Indian Ocean, and in eastern Africa. Decreasing cirrus is indicated in the higher latitudes of the southern hemisphere. The boreal winter 1991-92 shows an even stronger increase in cirrus with respect to the winter 1990-1991 (Figure 4b upper right panel). The largest increases are in the central Pacific Ocean, in the Indian Ocean, and the northern hemisphere mid-latitudes. The central Pacific Ocean is also the location of an El Nino event where sea surface temperature anomalies greater than 2.0 C were reported in January 1992.

The patterns of increasing cirrus in the boreal summer 1991 are consistent with the decrease in net radiation from ERBE for August 1991 observations compared to the August average for the previous five years, especially over the Amazon, the central Atlantic Ocean, the African Congo, off the east African coast, the southern Indian Ocean, and the central Pacific Ocean (Minnis et al., 1993). In this HIRS study, more thin cirrus was found after the eruption of Mt. Pinatubo at the expense of opaque cloud. This is consistent with the hypothesized indirect effect of aerosols, which would cause more high thin cirrus cloud to be produced and to be longer lasting (Sassen, 1992).

In the fourth summer of this study, a slight cirrus decrease (Figure 4a lower left panel) is found in the southerly latitudes (50 S to 75 S) and in the Atlantic Ocean off the east coast of Africa. Elsewhere there is no recognizable pattern. Finally, Figure 4b (lower left panel) shows the difference for the boreal winters 1992-93 minus 1991-92. Cirrus probability decreases noticeably in the central Pacific Ocean (the location of a dramatic increase in sea surface temperature the previous winter), in the Gulf of Mexico and Central America (in contrast to the increase in the previous year), and off the west coast of Australia in the Indian Ocean (again the location of a noticeable increase the previous year). This last winter appears to be compensating for the local increases in cirrus from the previous winter.

The cirrus increase in 1991 (year 2 to year 3) is in concert with two major global events that effected most climatic data. They are summarized in Halpert and Ropelewski (1993). The first major event started in April 1991, when an increase in eastern Pacific Ocean temperatures signaled the start of an El Nino/Southern Oscillation (ENSO) event. Subsequently by October 1991, Outgoing Longwave Radiation (OLR) measurements from satellites and 850 hPa



wind observations showed large anomalies from climatic means. By January 1992, sea surface temperature anomalies in the eastern equatorial Pacific Ocean were greater than 2.0 C (NOAA, 1992). The second major event came in June 1991 with the eruption of Mt. Pinatubo, which set new records for ash and aerosol in the stratosphere. Aerosol optical depth measurements by Stowe et al. (1992) showed a dramatic increase in the tropics in the following months. This aerosol later spread to higher latitudes by the end of the year.

Figure 5 shows the monthly changes in these HIRS high cloud data for the four years. A major increase in global high clouds (solid line in Figure 5) begins in April 1991 coincident with the change in eastern Pacific Ocean temperatures. The frequency of high cloud observations (above 500 hPa) increases from 32% in March 1991 to 37% in June 1991 to 39% in December 1991. The largest high cloud increases are in the tropics (20 S to 20 N). Tropical high cloud frequency increases from 34% in March 1991 to 40% in June 1991 (long dash in Figure 5), while tropical light cirrus ( $N_{\epsilon} < 0.5$  or  $\tau < 0.7$ ) increases even more from 23% in March 1991 to 31% in June 1991 (short dash in Figure 5). Examination of the local region in the eastern Pacific Ocean (10 S to 10 N, 110 W to 170 W) reveals even more dramatic changes (dot dash in Figure 5). Light cirrus observations change from near 25% frequency during the winter to over 40% in the summer. Seasonal and monthly changes are evident. In the boreal winter (December 1991 to February 1992) frequencies of 55-60% are found, well in excess of the previous years.

Changes in the satellite system are not the cause of the increased detection of cirrus and high cloud. In June 1991, NOAA 12 replaced NOAA 10 as the sunrise and sunset satellite. NOAA 11, the midday and midnight satellite, maintained continuous operation through this entire four year period. Examination of NOAA 11 data only reveals the same changes. Thus we

conclude that the change in satellites had no effect on the trends evident in this data. The increase in stratospheric aerosol also should not have affected the cloud observations. The CO<sub>2</sub> sounding bands are in the 13 to 15 micron region of the infrared spectrum, which is beyond the portion of the spectrum affected by these very small stratospheric particles (Ackerman and Strabala, 1994).

It is also significant that the increase in cirrus and high cloud observations continue into 1993 with reduction only in small areas. The other climatic indicators such as the eastern Pacific Ocean temperatures, OLR, and 850 wind anomalies revert back to near normal (average) levels by July 1992. The increased detection of cirrus in the HIRS data persists beyond 1992 into 1993. We don't have an explanation for this persistence, but suggest that forces that cause and maintain cirrus (as described in Menzel et al. (1992)) are subtle and could be present even after other climatic anomalies have subsided.

## 6. Diurnal Trends

Diurnal variations in cloud cover are examined using the four observations from the two NOAA satellites each day. NOAA 11 passes over a given location at approximately 0200 to 0300 a.m. and p.m. local time (midnight and midday) every day while NOAA 10 and 12 have an overpass from 0700 to 0800 a.m. and p.m. local time (sunrise and sunset). These observations are analyzed in four time blocks of 6 hours each. Differences in the frequency of cloud observations from the daily mean are presented in Figure 6. The diurnal anomalies are expressed as the difference of the frequency of observation of cloud from the mean frequency using all observations at all times. Diurnal variations in cloud cover are discussed

only over water. Over land, two of the four satellite passes are not analyzed each day because the NMC model analysis does not track the strong diurnal variations in surface temperatures, especially in many desert areas. Over the ocean, the diurnal surface temperature change is presumed to be insignificant and the same NOAA/NESDIS sea surface temperature analysis is used for each satellite pass in this cloud analysis.

A diurnal cycle in all cloud observations (Figure 6), both cirrus and lower altitude cloud forms, is found mainly outside of the ITCZ. Maxima occur in the midnight overpass. Geographical diurnal variations (not shown) are strongest in the southeastern Atlantic and Pacific Oceans. Some variations are present in the northeastern Pacific Ocean, near the coasts of California and Baja, and in the central Atlantic Ocean to the African coast. The cycle appears to be stronger during the summer and is dominated by lower cloud forms, mostly marine stratus.

High clouds (above 500 hPa) show little diurnal pattern (see Figure 7). The frequency of these clouds changes by  $\pm 3$  percentage points during the day at all latitudes. The largest diurnal variation is found near the ITCZ from the Equator to 15 N in the boreal summer. Thin cirrus ( $N_c < 0.5$  or  $\tau < 0.7$ ) exhibit even smaller diurnal variations with no obvious pattern.

## 7. Summary and Conclusions

There continues to be a global preponderance of transmissive clouds 42% on the average for the four years covered by June 1989 to May 1993. About three fourths of these are above 500 hPa and presumed to be cirrus. In the ITCZ a high frequency of cirrus (greater than 50%) is found at all times; a modest seasonal movement tracks the sun. Large seasonal changes in cloud cover occur over the oceans in the storm belts at mid-latitudes; the

concentrations of these clouds migrate north and south with the seasons following the progressions of the subtropical highs (anticyclones). More cirrus is found in the summer than in the winter in each hemisphere (largely due to the ITCZ).

Large changes in cirrus and high cloud cover are found beginning in the spring-summer 1991. These cloud frequency increases occur in concert with the 1991-1992 ENSO and the Mt. Pinatubo volcanic eruption. Associated changes include an increase in sea surface temperature starting April 1991, anomalies in Outgoing Longwave Radiation and 850 hPa winds around October 1991, and a dramatic increase in stratospheric aerosol after June 1991. The cirrus and high cloud increase starts before Mt. Pinatubo's eruption and persists beyond the summer of 1992, at which time the ENSO anomalies are mostly gone and stratospheric aerosol measurements are near their pre-eruption levels. Decreases in cirrus are seen in local regions, but higher occurrence of cirrus in the global average remains. There is no obvious explanation, other than thin cirrus are statistically persistent and do not exhibit large seasonal changes outside of the tropics whereas other cloud forms do show large seasonal variations.

The increase in cirrus and high cloud is accompanied by a corresponding decrease in satellite observations of lower altitude opaque clouds; overall cloudiness changed very little during this period. Obviously, a satellite detects lower cloud forms less when higher clouds become more prevalent. However, the trend reported in this paper of more transmissive high cloud and less low opaque cloud is loosely supported by appreciable decreases in precipitation in many regions of the world (Halpert and Ropelewski, 1993) during the 1991-1992 ENSO and volcanic period.

A similar increase in cloud cover also was reported in the 1982-83 ENSO by Weare (1992) using the NIMBUS-7 infrared analysis of Stowe et al. (1988). An increase in both the amount of cloud (all altitudes) and the average cloud height was found. The height increase indicated more high cloud in late 1982 and most of 1983 during the height of the ENSO. This is a similar trend which this HIRS analysis finds for the 1991-92 ENSO. We have no explanation for these changes in global cloud cover. This is the topic of future studies.

#### Appendix A. Technique Description

The HIRS radiometer senses infrared radiation in eighteen spectral bands that lie between 3.9 and 15 microns at 20 to 35 km resolution (depending upon viewing angle) in addition to visible reflections at the same resolution. The four bands in the CO<sub>2</sub> absorption band at 15 microns are used to differentiate cloud altitudes and the longwave infrared window band identifies the effective emissivity of the cloud in the HIRS FOV.

The CO<sub>2</sub> slicing technique is derived from the calculation of radiative transfer in an atmosphere with a single cloud layer. For a single level cloud element in a FOV the radiance observed at the satellite,  $R(\eta)$ , in spectral band  $\eta$  can be written

$$R(\eta) = (1 - N\epsilon) \left\{ B(\eta, T(P_S)) \tau(\eta, P_S) + \int_{P_S}^{P_C} [B(\eta, T(p)) d\tau/dp] dp \right\} + N\epsilon B(\eta, T(P_C)) \tau(\eta, P_C) + \int_{P_C}^0 [B(\eta, T(p)) d\tau/dp] dp \quad (1)$$

where  $\tau(\eta, P)$  is the transmittance through the atmosphere for band  $\eta$ ,  $N\epsilon$  is the effective emissivity of the cloud in the FOV, and  $B(\eta, T(P))$  is the Planck function for band  $\eta$  and temperature  $T$  at pressure level  $P$ .  $P_S$  is the surface pressure while  $P_C$  is the cloud top pressure. The four terms in Equation (1)

are the radiation emitted from the surface, the contribution from the atmosphere below the cloud, the cloud contribution, and the contribution from the atmosphere above the cloud. For a clear FOV ( $N\epsilon = 0$ ), the satellite measured radiance  $R_{clr}$  is

$$R_{clr}(\eta) = B(\eta, T(P_S)) \tau(\eta, P_S) + \int_{P_S}^0 [B(\eta, T(p)) d\tau/dp] dp . \quad (2)$$

Subtracting the clear FOV radiance  $R_{clr}(\eta)$  from the cloudy FOV radiance  $R(\eta)$  yields the following result.

$$R(\eta) - R_{clr}(\eta) = - N\epsilon B(\eta, T(P_S)) \tau(\eta, P_S) - N\epsilon \int_{P_S}^{P_C} [B(\eta, T(p)) d\tau/dp] dp + N\epsilon B(\eta, T(P_C)) \tau(\eta, P_C) . \quad (3)$$

This is the cloud signal in the satellite measured radiances for spectral band  $\eta$ ; it is the radiance difference of the cloudy FOV from neighboring clear FOVs. A simplified equation, after integration by parts, is

$$R(\eta) - R_{clr}(\eta) = N\epsilon \int_{P_S}^{P_C} [\tau(\eta, p) dB(\eta, T(p))/dp] dp . \quad (4)$$

Following the work of Smith and Platt (1978), the ratio of the cloud signal for two spectral bands of frequency  $\eta_1$  and  $\eta_2$  viewing the same FOV can be written as

$$\frac{R(\eta_1) - R_{clr}(\eta_1)}{R(\eta_2) - R_{clr}(\eta_2)} = \frac{N\epsilon_1 \int_{P_S}^{P_C} [\tau(\eta_1, p) dB(\eta_1, T(p))/dp] dp}{N\epsilon_2 \int_{P_S}^{P_C} [\tau(\eta_2, p) dB(\eta_2, T(p))/dp] dp} . \quad (5)$$

If the frequencies are close enough together, then  $N\epsilon_1$  approximates  $N\epsilon_2$ , and one has an expression by which the pressure of the cloud ( $P_C$ ) within the FOV can be calculated without apriori knowledge of the emissivity.

The left side of Equation (5) is determined from the satellite observed radiances in a given FOV and the clear air radiances inferred from spatial analyses of satellite clear radiance observations. The right side of Equation (5) is calculated from a temperature profile  $T(p)$  and the profiles of atmospheric transmittance for the spectral bands  $\tau(\eta, P)$  as a function of  $P_c$ , the cloud top pressure. The calculation uses global analyses of temperature and moisture fields from the National Meteorological Center (NMC) and is performed at 50 hPa intervals from 1000 hPa to 100 hPa. For a given spectral band pair, the solution for  $P_c$  is the best match of observed and calculated ratios.

Once a cloud height has been determined, an effective emissivity (also referred to as effective cloud amount in this paper) is evaluated from the infrared window band data using the relation

$$N\epsilon = \frac{R(w) - R_{clr}(w)}{B[w, T(P_c)] - R_{clr}(w)} \quad (6)$$

Here  $N\epsilon$  is the effective cloud amount observed in the window band,  $w$  represents the window band frequency, and  $B[w, T(P_c)]$  is the opaque cloud radiance in the window band.

Using the ratios of radiances of the four  $CO_2$  spectral bands, four separate cloud top pressures can be determined (14.2/14.0, 14.0/13.7, 14.0/13.3, and 13.7/13.3). Whenever  $(R - R_{clr})$  is within five times the noise response of the instrument (conservatively estimated at roughly 1  $mW/m^2/ster/cm^{-1}$ ), the resulting  $P_c$  is rejected. Using the measured infrared window radiance and the four cloud top pressures, four calculations of effective emissivity are also made. As described by Menzel et al. (1983), the most representative cloud height and effective emissivity are those that best satisfy the radiative transfer equation for the four  $CO_2$  spectral bands.

If no ratio of radiances can be reliably calculated because  $(R-R_{clr})$  is within five times the instrument noise level, then a cloud top pressure is calculated directly from the comparison of the HIRS observed 11.1 micron infrared window band brightness temperature with an in situ temperature profile and the effective emissivity is assumed to be unity. In this way, all clouds are assigned a cloud top pressure either by  $CO_2$  or infrared window calculations.

Fields of view are determined to be clear or cloudy through inspection of the 11.1 micron brightness temperature with an 8.3 or 12.0 micron band correction for moisture absorption. The band differences (11.1 - 8.3 micron for NOAA 10 and 12, or 11.1 - 12.0 micron for NOAA 11) were used to lower the threshold for clear-cloudy decisions in areas where water vapor affected the window band. This threshold change varied from 0 C near the poles in dry air masses to as high as 7 C in the moist tropical atmospheres. If the moisture corrected 11.1 micron brightness temperature is within 2.5 C of the known surface temperature (over land this is inferred from the NMC Medium Range Forecast (MRF) model analysis; over the oceans this is the NOAA/NESDIS sea surface temperature analysis), then the FOV is assumed to be clear ( $P_c = 1000$  hPa) and no cloud parameters are calculated.

The HIRS data are calibrated and navigated by NOAA/NESDIS. These data are transmitted daily to the Man computer Interactive Data Access System (McIDAS) at the University of Wisconsin-Madison. The HIRS data from NOAA 10, 11, and 12 are sampled to make the processing more manageable. Every third pixel on every third line is used. The data are also edited for zenith angle, eliminating data over  $10^\circ$  to assure top down viewing of the clouds and to minimize any problems caused by the increased path length through the atmosphere of radiation upwelling to the satellite. The resulting coverage is



restricted to approximately the center one third of the orbit swath. With two satellites, about one half of the Earth is sampled each day.

Morning orbits over land are not used because the surface temperature analysis over subtropical deserts is often warmer than the HIRS data; this causes cloud free areas to be mistaken as clouds. However, morning orbits over the oceans are used because no diurnal temperature change of the surface is assumed.

In the Arctic and Antarctic, the HIRS bands are inspected for the presence of surface temperature inversions. Over high altitude areas of Antarctica and Greenland, the HIRS 700 hPa band is often warmer than the window band. We assume that this indicates the presence of surface inversions from radiative cooling under clear skies. Surface inversions normally cannot be seen by the HIRS, but over polar high altitude continents the thermal contrast between 700 hPa and the elevated surface is often large enough to be detected. When the 700 hPa band is warmer than the window band, the observation is classified as cloud free. When the 700 hPa band is within 2.0 C of the window band, we assume that both bands saw the top of a cloud and the observation is classified as cloudy.

#### Appendix B. Comparison of AVHRR and HIRS cloud fractions.

In classifying transmissive cloud observations where the HIRS radiometer detects radiation from below a cloud layer as well as radiation from the cloud layer itself, we assume that more of the semi-transparency for a given field of view is due to cloud emissivity being less than one than due to the cloud not completely covering the HIRS 20 km field of view. In order to investigate this assumption more thoroughly, the effective emissivities  $N\epsilon_H$  from the HIRS

CO<sub>2</sub> slicing are compared to cloud fractions  $N_A$  inferred from 1 km Advanced Very High Resolution Radiometer (AVHRR) data.

Figure 8 shows the plot of AVHRR cloud fraction  $N_A$  (determined from the number of AVHRR FOVs where the moisture corrected infrared window brightness temperatures is 2 C colder than NOAA/NESDIS sea surface temperature analysis within a collocated HIRS FOV) versus the HIRS CO<sub>2</sub> slicing effective emissivity  $N\epsilon_H$ . Roughly 100 comparisons are made for data from 6 and 12 January 1994 covering 20 N to 40 N in the western Atlantic Ocean (Figure 9 shows the AVHRR infrared window image for 6 January 1994). FOVs with clouds tops below 700 hPa are not included in the comparison because the CO<sub>2</sub> slicing algorithm is not used below that altitude. These data include subtropical clouds, high clouds from a cold front, and post cold frontal clouds.

Three-fourths of the HIRS CO<sub>2</sub> cloud observations are found to be completely cloud covered in the AVHRR data ( $N_A$  between 0.90 and 1.00.). This is in good agreement with the work of Baum et al. (1992), where 60% of the HIRS FOVs were found to be completely cloud covered in the AVHRR data. The remaining fourth of the HIRS cloudy FOVs, where  $N_A$  is less than 0.90, have  $N\epsilon_H$  less than 0.45. It appears that for thick cloud ( $N\epsilon_H > 0.50$ ) the FOV is always completely cloud covered ( $N_A = 1.0$ ); for thin cloud ( $N\epsilon_H < 0.50$ ) the FOV is almost always more than half covered with cloud ( $0.50 < N_A < 1.0$ ). Wielicki and Parker (1992) also found that cirrus clouds have considerable spatial coherence and that most of the effect of sensor resolution is very weak on cirrus cloud cover estimates.

Figure 8 confirms the assertion that cloud emissivity and not cloud fraction is the dominant parameter in FOVs observed to have transmissive clouds. If cloud fraction,  $N$ , dominates and emissivity,  $\epsilon$ , of the cloud is not significant in the CO<sub>2</sub> slicing determination, then all points would lie on

the  $N_A = N\epsilon_H$  line. If  $\epsilon$  variation from FOV to FOV dominates  $N$  variation, then the points would lie on or close to the  $N_A = 1.0$  ordinate line. Clearly for  $0.5 < N\epsilon_H < 1.0$ , the cloud emissivity is the dominate cause of semi-transparency. Cloud fraction causes little change in observed radiance from one FOV to another. For  $0.0 < N\epsilon_H < 0.5$ , the cloud emissivity is the major cause, but cloud fraction is responsible for some of the variation.

#### Appendix C. Comparison of the NOAA/HIRS and the GOES/VAS cloud analyses.

The  $CO_2$  slicing technique has been used to process cloud parameters with GOES/VAS data for four years prior to the start of the NOAA/HIRS analysis reported here (see Wylie and Menzel, 1989, and Menzel et al., 1992). The GOES/VAS algorithm uses the same equations as shown in Appendix A. However, there are differences in the data and methods used in handling of the data.

(1) The GOES/VAS has three bands in the  $CO_2$  absorption region of the spectrum whereas the HIRS has four bands; the VAS does not have the 13.7 micron band which has additional mid-level sensitivity. (2) The GOES/VAS FOV (10 X 10 km) is smaller than the HIRS FOV (20 X 20 km); the VAS algorithm averages three FOVs for each cloud determination representing a  $300 \text{ km}^2$  observation area and a sample noise of roughly  $0.8 \text{ mW/m}^2/\text{ster/cm-1}$ , while the HIRS algorithm uses a single FOV representing a  $400 \text{ km}^2$  observation area with sample noise roughly  $0.2 \text{ mW/m}^2/\text{ster/cm-1}$ . (3) Surface topographic heights are used in the HIRS algorithm, while they are not in the VAS algorithm; the surface pressure in Equation (5) of Appendix A is determined from topography for the HIRS solutions while all VAS solutions assume a surface of 1000 hPa. This affects the VAS results over the Rocky Mountains by 50 hPa or less. (4) A separate sea surface temperature analysis is used in the HIRS processing while the VAS processing uses the same MRF model surface temperature analysis both over land

and water. The VAS land surface temperatures are corrected using the SVCA hourly reports, whereas the HIRS are not. This will affect the determination of low cloud with the window band, but it will have almost no effect on CO<sub>2</sub> algorithm solutions since only one of the bands sees the ground.

Single FOV comparisons of HIRS and VAS cloud parameter determinations are attempted. For several days during the 1986 FIRE (First International Satellite Cloud Climatology Project Experiment) in transmissive cloud conditions, over 100 collocated single FOV observations within 15 minutes were accomplished. CO<sub>2</sub> slicing cloud heights determined by the HIRS are 20 hPa larger (lower altitude) on the average than those from the VAS in the single FOV comparison; effective emissivities average 0.05 higher on the VAS than the HIRS. Fluctuations are on the order of 100 hPa for cloud top pressure and 0.30 for effective emissivity. In this single FOV study, the VAS and HIRS cloud parameters compare within the estimated errors (Menzel et al., 1992). However, these results, while reassuring, must be viewed with some caution. Collocation over the same cloud element is very difficult as the satellite sensors have different FOVs, viewing times, and viewing angles.

A more meaningful comparison of HIRS and VAS cloud analyses is the seasonal average of the frequencies of cloud observations over North America for the four years of the HIRS study (June 1989 to May 1993). Table 4 shows the summary of the four winter seasons (December, January, February) and four summer seasons (June, July, August) of the HIRS cloud observations covering the North American region (29 N to 49 N and 70 W to 130 W) as well as the corresponding seasonal summary of the VAS over the same area and time period. Both HIRS and VAS find roughly the same amount of seasonal cloud cover (70% HIRS and 73% VAS in the summer and 76% HIRS and 78% VAS in the winter). However, HIRS reports more transmissive cirrus in both winter and summer, 45%

HIRS to 33% VAS in winter and 35% HIRS to 27% VAS in summer. In particular, HIRS has 10 to 15% more mid-level (400 to 700 hPa) transmissive observations than the VAS. On the other hand VAS has 10% more low level opaque cloud observations. This is caused primarily by the larger noise in the VAS sensor which inhibits CO<sub>2</sub> slicing solutions for smaller cloudy versus clear radiance contrasts and identifies the cloud as low opaque in the infrared window solution.

The geographical distribution of the probabilities of high clouds above 500 hPa in each season computed from VAS and HIRS are presented in Figure 10. The cloud cover patterns are similar. In the winter, both the HIRS and VAS show higher probability of cloud cover over the Pacific northwest, the Rocky Mountains, and along the Gulf of Mexico and the eastern shore (40 to 60%), while they indicate a lower probability (20 to 40%) in the southwest over Baja Mexico. There is some disagreement in the northeast where VAS sees 20% more clouds than HIRS; this may be attributed to the large viewing angle of the VAS. In the summer, the cloud cover reduces (down by 20%) along the west coast and in the southern states, but it persists in the Rocky Mountains and along the eastern shore in both HIRS and VAS. Again there is disagreement in the northeast, where HIRS now sees 20% more cloud. Some of the moderate disagreement in both seasons over the oceans can be attributed to the difference in the sea surface temperature analysis used for HIRS versus VAS (as mentioned above).

In summary, the HIRS finds more mid-level (400-700 hPa) transmissive clouds and fewer low level opaque clouds than the VAS, but agrees with it in overall cloud reports. The geographical distribution of cloud reports from HIRS is similar to that from VAS, especially when a small VAS view angle is maintained.

## Acknowledgments

This work was supported by Grants N00014-85-K-0581 and N00014-87-K-0436 of the Office of Naval Research and Grant NAG1-553 and Contract NAS5-31367 from the National Aeronautics and Space Administration and Grant ATM-8703966 from the National Science Foundation and Contract 50-WCNE-8-06058 from the National Oceanic and Atmospheric Administration and Grant F19628-91-K-0007 from the United States Air Force Geophysics Laboratory.

## References

- Ackerman, S. A. and K. I. Strabala, 1994: Satellite remote sensing of H<sub>2</sub>SO<sub>4</sub> aerosol using the 8-12 micron window region: application to Mount Pinatubo. submitted to *J. Appl. Meteor.*
- Baum, B. A., B. A. Wielicki, and P. Minnis, 1992: Cloud-property retrieval using merged HIRS and AVHRR data. *J. Appl. Meteor.*, **31**, 351-369.
- Chahine, M. T., 1974: Remote sounding of cloudy atmospheres. I. The single cloud layer. *J. Atmos. Sci.*, **31**, 233-243.
- Eyre, J. R., and W. P. Menzel, 1989: Retrieval of cloud parameters from satellite sounder data: A simulation study. *J. Appl. Meteor.*, **28**, 267-275.
- Gruber, A., and T. S. Chen, 1988: Diurnal variation of outgoing longwave radiation. *J. Clim. Appl. Meteor.*, **8**, 1-16.
- Hartmann, D. L., M. E. Ockert-Bell, and M. L. Michelsen, 1992: The effect of cloud type on the Earth's energy balance: global analysis. *J. Climate*, **5**, 1281-1304.
- Halpert, M. S. and C. F. Ropelewski, 1993: Fourth Annual Climate Assessment, 1992. U. S. Dept of Commerce NOAA-NWS Climate Analysis Center, 90 pp.

- Jin, Y. and W. B. Rossow, 1994: Investigation and Comparison of ISCCP and HIRS high level clouds. Eighth Conference on Atmospheric Radiation held 22-28 January 1994 in Nashville, TN, AMS publication, 64-65.
- McCleese, D. J. and L. S. Wilson, 1976: Cloud top height from temperature sounding instruments. *Quart. J. R. Met. Soc.*, 102, 781-790.
- Menzel, W. P., W. L. Smith, and T. R. Stewart, 1983: Improved cloud motion wind vector and altitude assignment using VAS. *J. Clim. Appl. Meteor.*, 22, 377-384.
- Menzel, W. P., D. P. Wylie, and A. H.-L. Huang, 1986: Cloud top pressures and amounts using HIRS CO<sub>2</sub> channel radiances. Technical Proceedings of the Third International TOVS Study Conference, 13-19 August 1986, Madison, WI, 173-185.
- Menzel, W. P. and K. I. Strabala, 1989: Preliminary report on the demonstration of the VAS CO<sub>2</sub> cloud parameters (cover, height, and amount) in support of the Automated Surface Observing System (ASOS). NOAA Tech Memo NESDIS 29.
- Menzel, W. P., D. P. Wylie, and K. I. Strabala, 1989: Characteristics of global cloud cover derived from multispectral HIRS observations. Technical Proceedings of the Fifth International TOVS Study Conference, 24-28 July 1989, Toulouse, France, 276-290.
- Menzel, W. P., D. P. Wylie, and K. I. Strabala, 1992: Seasonal and diurnal changes in cirrus clouds as seen in four years of observations with the VAS. *J. Appl. Meteor.*, 31, 370-385.
- Minnis, P., E. F. Harrison, L. L. Stowe, G. G. Gibson, F. M. Denn, D. R. Doeling, and W. L. Smith, Jr., 1993: Radiative climate forcing by the Mount Pinatubo eruption. *Science*, 259, 1411-1415.

- NOAA, Climate Analysis Center, 1992: Near real time analysis ocean/atmosphere for January 1992. Climate Diagnostics Bulletin No. 92/1, Kousky, V. E. (ed)
- Rossow, W. B., and A. A. Lacis, 1990: Global and seasonal cloud variations from satellite radiance measurements. Part II: Cloud properties and radiative effects. *J. Climate*, 3, 1204-1253.
- Sassen, K., 1992: Evidence of liquid phase cirrus cloud formation from volcanic aerosols: Climatic implications. *Science*, 257, 516-519.
- Smith, W. L., H. M. Woolf, P. G. Abel, C. M. Hayden, M. Chalfant, and N. Grody, 1974: Nimbus 5 sounder data processing system. Part I: Measurement characteristics and data reduction procedures. NOAA Tech. Memo. NESS 57, 99pp.
- Smith, W. L., and C. M. R. Platt, 1978: Intercomparison of radiosonde, ground based laser, and satellite deduced cloud heights. *J. Appl. Meteor.*, 17, 1796-1802.
- Stowe, L. L., G. G. Wellemeier, T. F. Eck, H. Y. M. Yeh, and the Nimbus-7 Cloud Data Processing Team, 1988: Nimbus-7 global cloud climatology. Part I: Algorithms and validation. *J. Climate*, 1, 445-470.
- Stowe, L. L., R. M. Carey, and P. Pellegrino, 1992: Monitoring the Mt. Pinatubo aerosol layer with NOAA/11 AVHRR data. *Geo. Res. Letters*, 19, 159-162
- Susskind, J., D. Reuter, and M. T. Chahine, 1987: Cloud fields retrieved from analysis of HIRS/MSU sounding data. *J. Geophys. Res.*, 92, 4035-4050.
- Warren, S. G., C. J. Hahn, J. London, R. M. Chervin, and R. L. Jenne, 1988: Global distribution of total cloud over and cloud type amounts over the ocean. NCAR/TN-317+STR [Available from the National Center for Atmospheric Research, Boulder, CO, 80307]



- Weare, B. C., 1992: Variations in Nimbus-7 cloud estimates. Part I: zonal averages., *J. Climate*, 5, 1496-1505.
- Wielicki, B. A., and J. A. Coakley, 1981: Cloud retrieval using infrared sounder data: error analysis. *J. Appl. Meteor.*, 20, 157-169.
- Wielicki, B. A., and Parker, 1992: On the determination of cloud cover from satellite sensors: the effect of sensor spatial resolution. *J. Geophys. Res.*, 97, 12799-12823.
- Wu, M. L. and J. Susskind, 1990: Outgoing longwave radiation computed from HIRS2/MSU soundings. *J. Geophys. Res.*, 95D, 7579-7602.
- Wylie, D. P., and W. P. Menzel, 1989: Two years of cloud cover statistics using VAS. *J. Clim. Appl. Meteor.*, 2, 380-392.
- Wylie, D. P. and W. P. Menzel, 1991: Two years of global cirrus cloud statistics using HIRS. Technical Proceedings of the Sixth International TOVS Study Conference held 1-6 May 1991 in Airlie, VA, 344-353.

Table 1: HIRS four year global cloud statistics (June 1989 to May 1993) of the frequency of cloud observations for different heights and effective emissivities ( $N\epsilon$ ).  $N\epsilon < 0.25$  corresponds to infrared optical depth  $\tau < 0.3$ ;  $N\epsilon < 0.5$ ,  $\tau < 0.7$ ;  $N\epsilon < 0.75$ ,  $\tau < 1.4$ ; and  $N\epsilon < 0.95$ ,  $\tau < 3.0$ . Percentages are of the total number of observations, clear and cloudy combined. Clouds were not detected in 23.4% of the observations.

LEVEL	ALL CLOUDS	EFFECTIVE EMISSIVITY				
		<0.25	<0.50	<0.75	<0.95	>0.95
<200 hPa	3.5%	1.2%	0.4%	0.3%	0.7%	0.9%
<300 hPa	9.6	2.3	1.9	1.6	2.1	1.7
<400 hPa	10.8	2.5	2.3	2.2	2.4	1.4
<500 hPa	11.0	2.3	2.5	2.6	2.5	1.1
<600 hPa	8.2	1.4	2.2	2.5	0.7	1.4
<700 hPa	7.8	0.6	1.2	1.7	0.7	3.6
<800 hPa	7.6	0.2	0.4	0.4	0	6.6
<900 hPa	11.5	0	0	0	0	11.5
<1000 hPa	6.8	0	0	0	0	6.8
Total	76.8	10.5	10.9	11.3	9.1	35.0

Table 2a: The HIRS global cloud cover from all four years (June 1989 - May 1993).  $N\epsilon$  refers to effective emissivity and  $\tau$  refers to the corresponding infrared optical depth. Numbers are frequency of cloud cover; over 15,000,000 observations are included.

LEVEL	EFFECTIVE EMISSIVITY (IR OPTICAL DEPTH)			
	None	Thin	Thick	Opaque
		$N\epsilon < 0.50$	$0.5 < N\epsilon < 0.95$	$N\epsilon > 0.95$
		$\tau < 0.7$	$0.7 < \tau < 3.0$	$\tau > 3.0$
hi < 400 hPa		11	9	4
mid < 700 hPa		10	11	6
low < 1000 hPa		1	0	25
Total	23	42		35
	(clear)	(cirrus)		(opaque)

Table 2b: The HIRS global cloud cover in the boreal summer from all four years (June 1989 - May 1993).  $N\epsilon$  refers to effective emissivity and  $\tau$  refers to the corresponding infrared optical depth. Numbers are frequency of cloud cover; over 3,300,000 observations are included.

LEVEL	EFFECTIVE EMISSIVITY (IR OPTICAL DEPTH)			
	No	Thin	Thick	Opaque
		$N\epsilon < 0.50$	$0.5 < N\epsilon < 0.95$	$N\epsilon > 0.95$
		$\tau < 0.7$	$0.7 < \tau < 3.0$	$\tau > 3.0$
hi < 400 hPa		11	9	4
mid < 700 hPa		10	10	5
low < 1000 hPa		0	0	26
Total	25	40		35
	(clear)	(cirrus)		(opaque)

Table 2c: The HIRS global cloud cover in the boreal winter from all four years (June 1989 - May 1993).  $N\epsilon$  refers to effective emissivity and  $\tau$  refers to the corresponding infrared optical depth. Numbers are frequency of cloud cover; over 3,600,000 observations are included.

EFFECTIVE EMISSIVITY (IR OPTICAL DEPTH)				
	No	Thin	Thick	Opaque
		$N\epsilon < 0.50$	$0.5 < N\epsilon < 0.95$	$N\epsilon > 0.95$
		$\tau < 0.7$	$0.7 < \tau < 3.0$	$\tau > 3.0$
LEVEL				
hi < 400 hPa		11	10	4
mid < 700 hPa		10	11	7
low < 1000 hPa		0	0	24
Total	23		42	35
	(clear)		(cirrus)	(opaque)

Table 3a: The change in HIRS global cloud cover from year 1 (June 1989 - May 1990) to year 2 (June 1990 - May 1991).  $N\epsilon$  refers to effective emissivity and  $\tau$  refers to the corresponding infrared optical depth. Numbers are frequency of cloud cover in summer and winter of year 2 minus the same in year 1; negative numbers indicate a decrease in cloudiness while positive numbers indicate an increase.

LEVEL	EFFECTIVE EMISSIVITY (IR OPTICAL DEPTH)		
	Thin	Thick	Opaque
	$N\epsilon < 0.50$	$0.5 < N\epsilon < 0.95$	$N\epsilon > 0.95$
	$\tau < 0.7$	$0.7 < \tau < 3.0$	$\tau > 3.0$
hi < 400 hPa	0	1	-1
mid < 700 hPa	0	-1	0
low < 1000 hPa	0	0	0
Total	0	0	-1

Table 3b: The change in HIRS global cloud cover from year 2 (June 1990 - May 1991) to year 3 (June 1991 - May 1992). Numbers are frequency of cloud cover in summer and winter of year 3 minus the same in year 2.

LEVEL	EFFECTIVE EMISSIVITY (IR OPTICAL DEPTH)		
	Thin	Thick	Opaque
	$N\epsilon < 0.50$	$0.5 < N\epsilon < 0.95$	$N\epsilon > 0.95$
	$\tau < 0.7$	$0.7 < \tau < 3.0$	$\tau > 3.0$
hi < 400 hPa	4	1	0
mid < 700 hPa	2	1	-2
low < 1000 hPa	0	0	-5
Total	6	2	-7

Table 3c: The change in HIRS global cloud cover from year 3 (June 1991 - May 1992) to year 4 (June 1992 - May 1993). Numbers are frequency of cloud cover in summer and winter of year 4 minus the same in year 3.

LEVEL	EFFECTIVE EMISSIVITY (IR OPTICAL DEPTH)		
	Thin	Thick	Opaque
	$N\epsilon < 0.50$	$0.5 < N\epsilon < 0.95$	$N\epsilon > 0.95$
	$\tau < 0.7$	$0.7 < \tau < 3.0$	$\tau > 3.0$
hi < 400 hPa	0	0	0
mid < 700 hPa	2	-1	0
low < 1000 hPa	0	0	2
Total	2	-1	2



Table 4a: The HIRS cloud cover in the boreal summer from all four years (June 1989 - May 1993) over North America (29 to 49 N, 70 to 130 W).  $N\epsilon$  refers to effective emissivity and  $\tau$  refers to the corresponding infrared optical depth. Numbers are frequency of cloud cover; over 600,000 observations are included.

	EFFECTIVE EMISSIVITY (IR OPTICAL DEPTH)			
	None	Thin	Thick	Opaque
		$N\epsilon < 0.50$ $\tau < 0.7$	$0.5 < N\epsilon < 0.95$ $0.7 < \tau < 3.0$	$N\epsilon > 0.95$ $\tau > 3.0$
LEVEL				
hi < 400 hPa		9	9	6
mid < 700 hPa		9	8	8
low < 1000 hPa	30	0	0	21
Total	30		35	35
	(clear)		(cirrus)	(opaque)

Table 4b: The VAS cloud cover in the boreal summer from all four years (June 1989 - May 1993) over North America (29 to 49 N, 70 to 130 W).  $N\epsilon$  refers to effective emissivity and  $\tau$  refers to the corresponding infrared optical depth. Numbers are frequency of cloud cover; over 2,200,000 observations are included.

	EFFECTIVE EMISSIVITY (IR OPTICAL DEPTH)			
	None	Thin	Thick	Opaque
		$N\epsilon < 0.50$ $\tau < 0.7$	$0.5 < N\epsilon < 0.95$ $0.7 < \tau < 3.0$	$N\epsilon > 0.95$ $\tau > 3.0$
LEVEL				
hi < 400 hPa		10	12	3
mid < 700 hPa		2	3	10
low < 1000 hPa	27	0	0	33
Total	27	27		46
	(clear)	(cirrus)		(opaque)

Table 4c: The HIRS cloud cover in the boreal winter from all four years (June 1989 - May 1993) over North America (29 to 49 N, 70 to 130 W).  $N\epsilon$  refers to effective emissivity and  $\tau$  refers to the corresponding infrared optical depth. Numbers are frequency of cloud cover; over 600,000 observations are included.

	EFFECTIVE EMISSIVITY (IR OPTICAL DEPTH)			
	None	Thin	Thick	Opaque
		$N\epsilon < 0.50$ $\tau < 0.7$	$0.5 < N\epsilon < 0.95$ $0.7 < \tau < 3.0$	$N\epsilon > 0.95$ $\tau > 3.0$
LEVEL				
hi < 400 hPa		9	12	5
mid < 700 hPa		9	15	12
low < 1000 hPa	24	0	0	14
Total	24	45		31
	(clear)	(cirrus)		(opaque)

Table 4d: The VAS cloud cover in the boreal winter from all four years (June 1989 - May 1993) over North America (29 to 49 N, 70 to 130 W).  $N\epsilon$  refers to effective emissivity and  $\tau$  refers to the corresponding infrared optical depth. Numbers are frequency of cloud cover; over 2,600,000 observations are included.

		EFFECTIVE EMISSIVITY (IR OPTICAL DEPTH)			
		None	Thin	Thick	Opaque
			$N\epsilon < 0.50$	$0.5 < N\epsilon < 0.95$	$N\epsilon > 0.95$
			$\tau < 0.7$	$0.7 < \tau < 3.0$	$\tau > 3.0$
LEVEL					
hi < 400 hPa			10	15	4
mid < 700 hPa			2	6	20
low < 1000 hPa	22		0	0	21
Total	22		33		45
	(clear)		(cirrus)		(opaque)

## Figure Captions

Figure 1: (a) The geographic frequency of transmissive clouds for the boreal summers (June, July, August) during the observation period June 1989 thru May 1993. The left margin of the figure coincides with the International Date Line.

Figure 1: (b) The geographic frequency of transmissive clouds for the boreal winters (December, January, and February) during the observation period June 1989 thru May 1993.

Figure 2: The frequency of high clouds (cloud pressure  $< 500$  hPa) over ocean is shown in the upper panel as a function of latitude for the boreal summers (June, July, August) of 1989-92 and winters (December, January, February) 1989-93 expressed as a fraction of all satellite observations, clear and cloudy combined. The same over land is shown in the lower panel.

Figure 3: The frequency of thin transmissive clouds ( $N_{\epsilon} < 0.5$ ,  $\tau < 0.7$ ) over ocean is shown in the upper panel as a function of latitude as a fraction of all satellite observations, clear and cloudy combined. Land is shown in the lower panel.

Figure 4: (a) The geographical distribution of the difference in the probability of cirrus in the four boreal summers, 1990 minus 1989 upper left panel, 1991 minus 1990 upper right and 1992 minus 1991 in the lower left. The boreal summer includes the months of June, July, and August.

Figure 4: (b) The geographical distribution of the difference in the probability of cirrus occurring in the four boreal winters. Winter 1990-91

minus winter 1989-90 is the upper left panel, winter 1991-92 minus 1990-91 is the upper right panel and winter 1992-93 minus 1991-92 is the lower left panel. Boreal winter includes the months of December, January, and February.

Figure 5: Monthly time series of high cloud (over 500 hPa) observations from 65 S to 65 N latitude (solid line), light cirrus with  $N_{\epsilon} < 0.5$ ,  $\tau < 0.7$  in the tropics from 20 S to 20 N (triple dash), all high clouds (over 500 hPa) in the tropics, 20 S to 20 N (dash), and light cirrus ( $N_{\epsilon} < 0.5$ ,  $\tau < 0.7$ ) in the eastern Pacific Ocean from 10 S to 10 N, 110 W to 170 W (dash dot).

Figure 6: The diurnal change from the seasonal mean of all cloud observations expressed as a change in percentage points of the total clear and cloudy observations. Midnight represents the NOAA 11 evening pass which actually occurred between 0100 and 0300 a.m. local time. Sunrise is the morning NOAA 10 or 12 pass nominally from 0700 to 0800 a.m. local time. Local Noon is the afternoon NOAA 11 pass from 0100 to 0300 p.m. Sunset is the evening NOAA 10 or 12 pass from 0700 to 0800 p.m.

Figure 7: Same as Figure 6 for the change in the frequency of high cloud observations (pressure less than 500 hPa).

Figure 8: Plot of AVHRR cloud fraction  $N_A$  (determined from infrared brightness temperature comparison to surface temperature within a collocated HIRS FOV) versus the HIRS CO<sub>2</sub> slicing effective emissivity  $N_{\epsilon_H}$  for 6 and 12 January 1994 over the Atlantic Ocean.

Figure 9: AVHRR infrared window image from 6 January 1994 over the Atlantic Ocean from which the cloud fraction versus effective emissivity study was made. HIRS CO<sub>2</sub> cloud pressures are indicated in hPa divided by ten.

Figure 10: The frequency of high cloud observations (cirrus and opaque above 500 hPa) reported by VAS and HIRS during four years (June 1989 to May 1993) in the boreal winter months (December, January, and February) and in the boreal summer months (June, July, and August). Grey shades indicate changes of 20%.

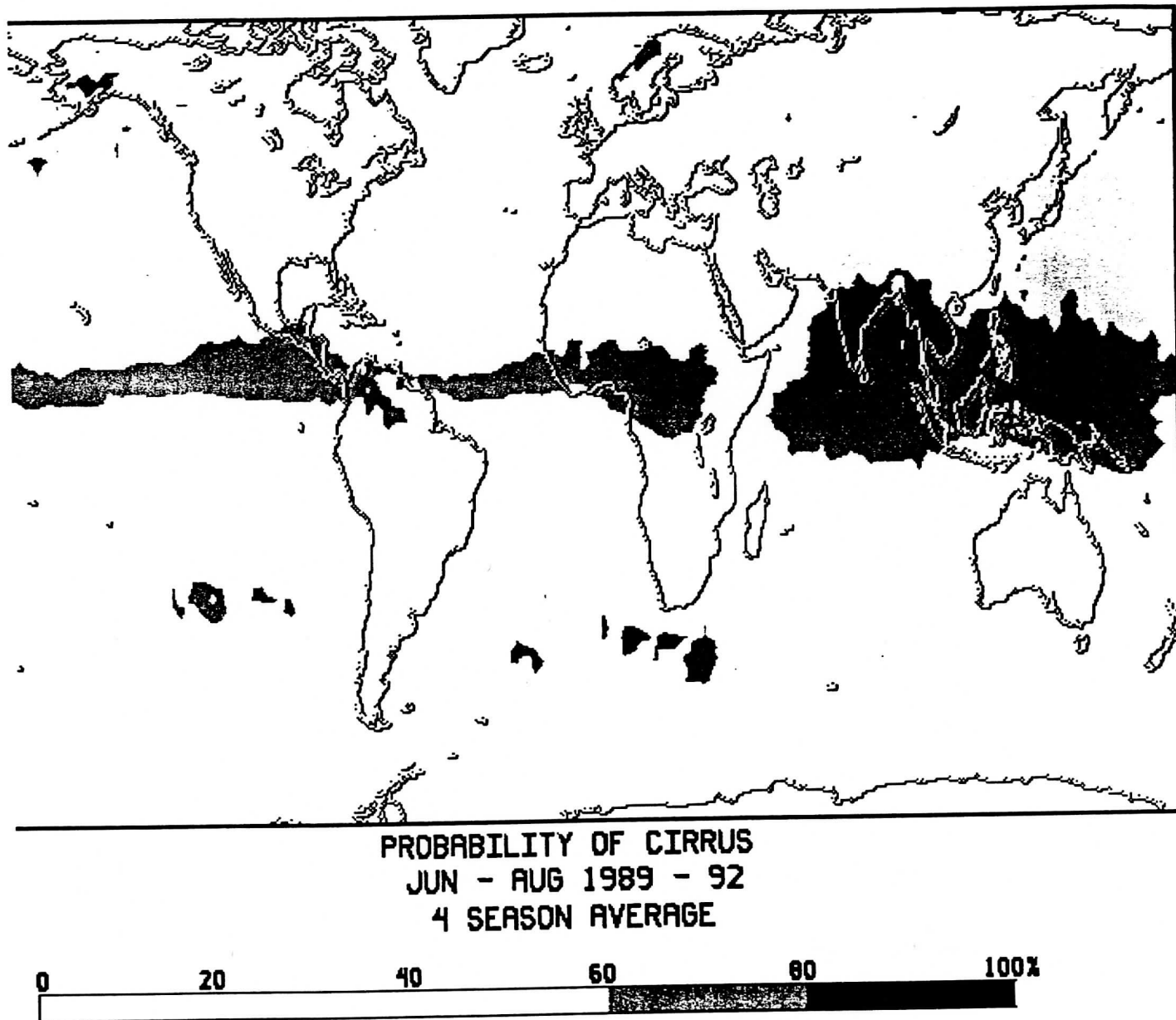


Figure 1: (a) The geographic frequency of transmissive clouds for the boreal summers (June, July, August) during the observation period June 1989 thru May 1993. The left margin of the figure coincides with the International Date Line.



FREQUENCY OF CLOUD COVER AT ALTITUDE: IMPLICATIONS FOR  
SURVEILLANCE SYSTEMS

Prepared by

I. S. ROBINSON and D. J. RUDY  
Sensing & Exploitation Department  
Sensor Systems Subdivision  
Electronic Systems Division  
Engineering and Technology Group

M. M. GONZALEZ  
Electromagnetic Techniques Department  
Communication Systems Subdivision  
Electronic Systems Division  
Engineering and Technology Group

September 1994


Engineering and Technology Group  
THE AEROSPACE CORPORATION  
El Segundo, CA 90245-4691

Prepared for

VICE PRESIDENT  
ENGINEERING AND TECHNOLOGY GROUP  
THE AEROSPACE CORPORATION  
EL Segundo, CA 90245-4691

FREQUENCY OF CLOUD COVER AT ALTITUDE:  
IMPLICATIONS FOR SURVEILLANCE SYSTEMS

Approved by

  
M. L. Bolla, Principal Director  
Sensor Systems Subdivision  
Electronic Systems Division  
Engineering and Technology Group

## Abstract

The communities involved with space- and air-based infrared (IR) surveillance have recently experienced a surge of interest in understanding the frequency with which clouds obscure target vehicles flying at various altitudes. There has also been interest in ascertaining the frequency of cloud-induced IR clutter levels that can impair detection by space-based systems. Both of these issues depend strongly on the frequency of occurrence of clouds at different altitudes and the properties of those clouds. The issue of obscuration is highly relevant to the viability of detection of low altitude targets and to the altitude at which airborne sensors may be based.

Several data sets containing statistics of global cloud cover have been examined over the past year. High altitude clouds have the greatest affect on both IR clutter and target obscuration. The cloud climatology based on measurements with the best sensitivity for detecting and estimating the altitude of clouds comes from the University of Wisconsin (UW).

Good agreement has been found between the UW data and other sources in the geographic and seasonal distribution of high clouds. There is substantial disagreement in the absolute frequency of occurrence for high clouds. The UW climatology reports higher frequency of occurrence of all clouds, but particularly high clouds, than most of the other data sets. We consider the UW climatology to have been developed with superior techniques for cloud detection and estimation of cloud altitude. With a few adjustments, the UW data will represent "truth" in cloud frequency of occurrence at altitude.

Data derived from the Stratospheric Aerosol and Gas Experiment-II (SAGE-II) are considered to have fidelity, comparable to the UW data, in reporting high clouds. The SAGE-II data (not selected as the primary data source because of poorer sampling and spatial resolution than the UW data) report a greater frequency of occurrence of high clouds than the UW data. A case is shown where the two data sets agree when a proposed correction is made to the UW data.

This report is limited in detail in order to expedite the dissemination of high fidelity cloud data. A future report will provide quantitative comparisons of the UW data with other cloud data sets. It will provide tabular data of cloud cover, at altitude, for regions of interest. The future report will describe the geometric and spectral dependencies of cloud-free line-of-sight (CFLOS).

## Acknowledgment

The authors would like to gratefully acknowledge Dr. Donald Wylie of the University of Wisconsin for generously providing his global cloud climatology and thorough documentation of both the data and techniques used to create the climatology.

# Contents

Abstract.....	iii
Acknowledgment.....	iv
1. Introduction .....	1
2. Cloud Climatologies .....	2
2.1 Introduction to Cloud Climatologies.....	2
2.2 SAGE-II Data.....	4
2.3 University of Wisconsin Data .....	4
2.4 Limitations of the UW Data.....	5
2.5 Biases and Errors in the UW Data.....	15
3. Global High Cloud Data .....	16
3.1 High Clouds .....	16
3.2 Seasonal Variations.....	16
3.3 Altitudinal Variations.....	18
3.4 Cloud Opacity .....	19
4. Cloud Obscuration and Clutter.....	22
4.1 Clouds at Altitude.....	22
4.2 Dependence of Obscuration on Spectral Band .....	23
4.3 Dependence of Obscuration on Zenith Angle .....	23
4.4 Clutter Induced by Clouds.....	25
5. Summary and Future Plans.....	27
6. References.....	28

## Figures

1.	Frequency of cloud cover in summer at altitudes at or above 6 km; clouds of all thicknesses.....	6
2.	Frequency of cloud cover in winter at altitudes at or above 6 km; clouds of all thicknesses.....	7
3.	Frequency of cloud cover in spring at altitudes at or above 6 km; clouds of all thicknesses.....	8
4.	Frequency of cloud cover in fall at altitudes at or above 6 km; clouds of all thicknesses.....	9
5.	Frequency of cloud cover in summer at altitudes at or above 10 km; clouds of all thicknesses.....	10
6.	Frequency of cloud cover in winter at altitudes at or above 10 km; clouds of all thicknesses.....	11
7.	Frequency of cloud cover in summer at altitudes at or above 4 km; clouds of all thicknesses.....	12
8.	Frequency of cloud cover in summer at altitudes at or above 8 km; clouds of all thicknesses.....	13
9.	Frequency of cloud cover in summer at altitudes at or above 6 km; clouds with transmissivity of less than 50% at wavelength 11.1 $\mu\text{m}$ only are included.....	14
10.	Satellite coordinate system.....	21

## Table

1.	Cloud Frequency of Occurrence Above Altitude.....	19
----	---	----

## 1. Introduction

The communities involved with space- and air-based infrared (IR) surveillance have recently experienced a surge of interest in understanding the frequency with which clouds obscure target vehicles flying at various altitudes. There has also been interest in ascertaining the frequency of cloud-induced IR clutter levels that can impair detection by space-based systems. Both of these issues depend strongly on the frequency of occurrence of clouds at different altitudes and the properties of those clouds. The issue of obscuration is highly relevant to the viability of detection of low altitude targets and to the altitude at which airborne sensors may be based.

This report is based on results developed under an Aerospace Sponsored Research Project (ASR), initiated in FY '94, to acquire the highest fidelity cloud data sets available to investigate cloud frequency of occurrence at altitude. As part of the ASR, the attributes of many cloud climatologies were examined. The data set selected as having the best combination of characteristics was derived from the High Resolution Infrared Radiation Sounder-2 (HIRS-2) flying on the NOAA polar orbiting weather satellites by researchers at the University of Wisconsin (UW).

The UW cloud climatology shows that clouds are present in some amount, at some time of year, over almost every point on the globe. The presence of clouds at different altitudes is strongly dependent on the time of year and geographic location. Thus, targets at lower altitudes will be far less accessible to an IR sensor in some regions than others. Not all clouds are completely opaque. The opacity of clouds depends on their composition, physical thickness, the spectral band of interest and the angle at which the cloud is viewed.

This report provides an overview of the method used at UW to derive global cloud statistics and some of its limitations. Global maps displaying the frequency of cloud cover at representative altitudes as a function of location, season, and altitude are provided. Obscuration by clouds and the clutter caused by clouds for different surveillance missions are discussed.

We have not provided discussion in significant detail in order to expedite both the dissemination of high fidelity data and an understanding of the data to the surveillance communities. A future report will provide quantitative comparisons of the UW data with other cloud data sets. It will provide tabular data of cloud cover at altitude for regions of interest. The future report will also examine the geometric and spectral dependencies of cloud-free line-of-sight (CFLOS).

## 2. Cloud Climatologies

This section will provide a brief description of the techniques used to create cloud climatologies, including their strengths and weaknesses. A cloud climatology from the UW data set has been chosen as having the best combination of attributes to assess frequency of occurrence of clouds at different altitudes. With modifications described, the UW data is proposed as "truth". The contents of the climatology are discussed. The techniques used to create the UW climatology, its limitations, and possible errors in the data are discussed.

### 2.1 Introduction to Cloud Climatologies

Cloud climatologies are collections of cloud cover information as a function of location and time of year. They are based on observations taken by satellites, ships, aircraft, and ground personnel. Many such data sets have been accumulated in the last 20 years (some earlier) with varying degrees of global sampling, cloud detection sensitivity, capability to estimate cloud opacity and "brokenness", and substantial variability in the fidelity of cloud altitude estimation. References 1 through 3 provide an extensive list of these data sets.

Satellites provide a unique capability to cover large areas of the globe in a short period of time. They have a simple limitation in that they are primarily sensitive to the highest altitude clouds along a line-of-sight (LOS). Similarly, cloud statistics based on ground, ship, or airplane observations (collectively called surface observations or SOBS) will see only the bottom of the lowest level cloud along a LOS. Ground observers also have a limitation in that they directly sense only the altitudes of cloud bottoms. Information on cloud top height must be estimated or inferred from measurements of transmission or radiance from the cloud. SOBS are further limited in that only (small) regions within the observer's local horizon may be covered. Because our interest is focused on cloud (top) cover at high altitude, often over remote territories, the discussion emphasizes data sets derived from satellite measurements.

The majority of satellite-based global cloud data sets are built using measurements of clouds in one or a few spectral regions intended to provide high transmission from space to ground (e.g. visible, long wave IR). Techniques based on these spectral bands have weaknesses in the detection and altitude estimation of many high altitude clouds which are primarily composed of ice. In general, cloud detection, and estimation of both cloud thickness and altitude, depend on estimating temperature of the cloud and computing differences from the expected ground temperature. Small errors in the conversion of radiance to temperature, the assumed temperature profile of the atmosphere, or in knowledge of the ground temperature can result in missed cloud detections or underestimates of cloud altitude. A frequent error is misidentification of temperature resulting from



small amounts of radiance from warmer sources (e.g. ground or lower level clouds) scattering through the clouds.

The International Satellite Cloud Climatology Project (ISCCP) uses visible and long wave IR (LWIR) data from virtually all geostationary and two U. S. polar-orbiting satellites to create detailed global climatologies of cloud cover. The ISCCP attempts to correct the temperature retrieved from IR measurements by assessing cloud opacity in the visible (see Ref. 4). The ISCCP reports a higher frequency of high clouds than other climatologies created with similar data. The innate sensitivity to assumptions of cloud-free radiance levels brings into question the value of the ISCCP climatology for our purposes. We have acquired one year's worth of ISCCP data and will be performing comparisons between it, the UW data, and a climatology derived from SAGE-II.

The UW data are derived from several techniques including the CO<sub>2</sub> slicing technique. Cloud/no-cloud decisions are based on apparent temperatures in the 11.1 μm channel. Cloud altitude estimation is performed using data in four narrow spectral channels of the HIRS-2. The HIRS-2 sensor is described in Reference 5. These channels are located at increasing distance from the 15 μm CO<sub>2</sub> atmospheric absorption band; they are centered at 13.3, 13.7, 14.0, and 14.3 μm, respectively. These channels do not provide high transmission to the ground but are each designed to have a peak response to emissions at a different altitude in the lower atmosphere. Altitude estimation does not require conversion to temperature, nor is precise knowledge of ground temperature needed. The UW cloud estimates are much less sensitive to a priori knowledge of prevailing conditions than most data sets.

University of Wisconsin uses a very small difference (2.5°C) between predicted and measured temperature to detect clouds. In comparison, ISCCP data reports cloud presence when observed brightness temperatures differ from expectation by 3°C over ocean and 6° over land. Dr. Don Wylie at UW justifies the use of a small temperature threshold because another HIRS-2 channel in the LWIR is used to correct the 11.1 μm data for moisture absorption. He also claims that "false" detections in the 11.1 μm channel will be rejected in the CO<sub>2</sub> slicing processing. A sample that is rejected in the CO<sub>2</sub> slicing step is assumed to have unity emissivity at the temperature measured in the 11.1 μm channel. Such a false detection will result in the report of a very low altitude cloud and is not relevant for our purposes (see Ref. 7).

The techniques used to create the UW data provide an excellent combination of cloud detection and cloud altitude estimation. The UW data also provides substantial information on partially transmissive clouds. Measurements from two polar orbiting satellites provide high frequency of coverage on a global basis. This combination of factors is the basis for selecting the

UW as our primary data source. Only one other data set, described below, has comparable fidelity for characterizing the presence of high altitude clouds.

## **2.2 SAGE-II Data**

A data set derived from measurements by the second Stratospheric Aerosol and Gas Experiment (SAGE-II) also avoids the conversion of radiance to temperature as a crucial step in the cloud detection process. SAGE-II, and its predecessor, SAGE (Ref. 6), are solar occultation experiments. SAGE-II, in continuous operation for about 10 years, views the sun through the lower atmosphere on a continuing basis. When sunlight is attenuated below a given threshold then it is known that a cloud is present along the LOS. The angle above-the-horizon (ATH) at which the LOS is obscured, allows a very precise altitudinal (lower bound) estimate of the cloud.

SAGE-II is considered to have sensitivity to detect virtually any cloud at high altitude and provides excellent altitudinal information. Unfortunately, SAGE-II only takes data along the LOS between the sensor and the sun providing only sparse spatial sampling of cloud conditions. The SAGE-II data are not used as our primary climatology because of the instrument's poor spatial coverage, and the fact that little information on broken cloud fields or on partially transmissive clouds is provided.

## **2.3 University of Wisconsin Data**

The data we are using was provided by Dr. Don Wylie of the UW, Madison. The techniques used to develop the data base, error sources, and several characteristics of the data are described in publications by Dr. Wylie, Dr. Kathleen Strabala (also of UW), and Dr. Paul Menzel (of the NOAA/NESDIS Satellite Applications Lab); see References 8 and 9.

The data set is provided in four files and represents over 15,000,000 observations. Each file contains averages over a season (e.g. Summer spans June, July, and August) for the period of June 1989 through February 1993. The data is mapped to a global grid (latitudes beyond  $\pm 83^\circ$  are excluded) with each point spanning  $2^\circ$  of latitude by  $3^\circ$  of longitude; about 250 km on a side in the mid-latitude regions. Figures 1 through 9 are maps created from the UW data, each containing roughly 10,000 spatial locations. For each location, the percentage of observations in which clouds were present is given for the specified season. Cloud presence is further described by the fraction of time cloud tops were present at nine distinct atmospheric pressure (altitude) levels. Lastly, for each location and altitude level the cloud cover is separated into five divisions of area-emissivity ( $N\epsilon$ ) product.

The spatial resolution of the HIRS-2 is about 18 km at nadir. Data are taken from within a swath of  $\pm 45^\circ$  of nadir by the HIRS-2. Wylie et al have only used data taken within  $10^\circ$  of nadir in the current data set; an average pixel size of 20 km is assumed.  $N\epsilon$  is the product of the emissivity,  $\epsilon$ , measured in the 11.1  $\mu\text{m}$  channel of the HIRS-2 and,  $N$ , the fraction of the 20 km HIRS-2 pixel filled by clouds. This product bounds the opacity of the clouds and the fractional cloud cover.

## 2.4 Limitations of the UW Data

As mentioned in the previous section, each data point represents the frequency of occurrence of clouds in a  $2^\circ$  by  $3^\circ$  box, averaged over a season. Frequency of occurrence is determined by the fraction of time a 20 km HIRS-2 pixel contains a cloud with the altitude/emissivity combination of interest. The spatial and temporal averaging performed results in an ambiguity in the interpretation of cloud frequency of occurrence. A location reported to have 40% frequency of occurrence may have been 40% covered with clouds for the entire 3-month period, or it may have been 100% cloudy for 40% of the season, or some in-between combination. The cloud cover reported is a spatial-temporal average for the location specified and the season. The UW data provide a lower bound on the fraction of time clouds are present.

Another limitation is the ambiguity that results in the interpretation of an  $N\epsilon$  product of less than unity. There is no way to discern whether there are partially transmissive clouds filling the entire (20 km) pixel, opaque clouds filling a portion of the HIRS-2 pixel, or some combination.

The data set now resident at Aerospace contains multi-year averages. Reference 7 shows that there can be substantially different amounts of high cloud cover in a given location from year-to-year. For example, the multi-year average of clouds probability at or above 6 km in the neighborhood of North Korea is about 50%. A number of locations in this area show year-to-year variations of  $\pm 12.5\%$  and a few spots differ by 25%, or more, in successive years.

In the future we plan to obtain separate data sets for each year averaged over monthly periods. This will enable us to better quantify variations and extremes. For the present, the frequency of occurrence values shown in the Figures 1 through 9 should be understood to represent annual, seasonal averages with a standard deviation of  $\sim \pm 20\%$  of the value shown.

University of Wisconsin HIRS-2 Cloud Climatology  
Summer, Cloud Frequency of Occurrence at 6 Km and Above, All Thicknesses

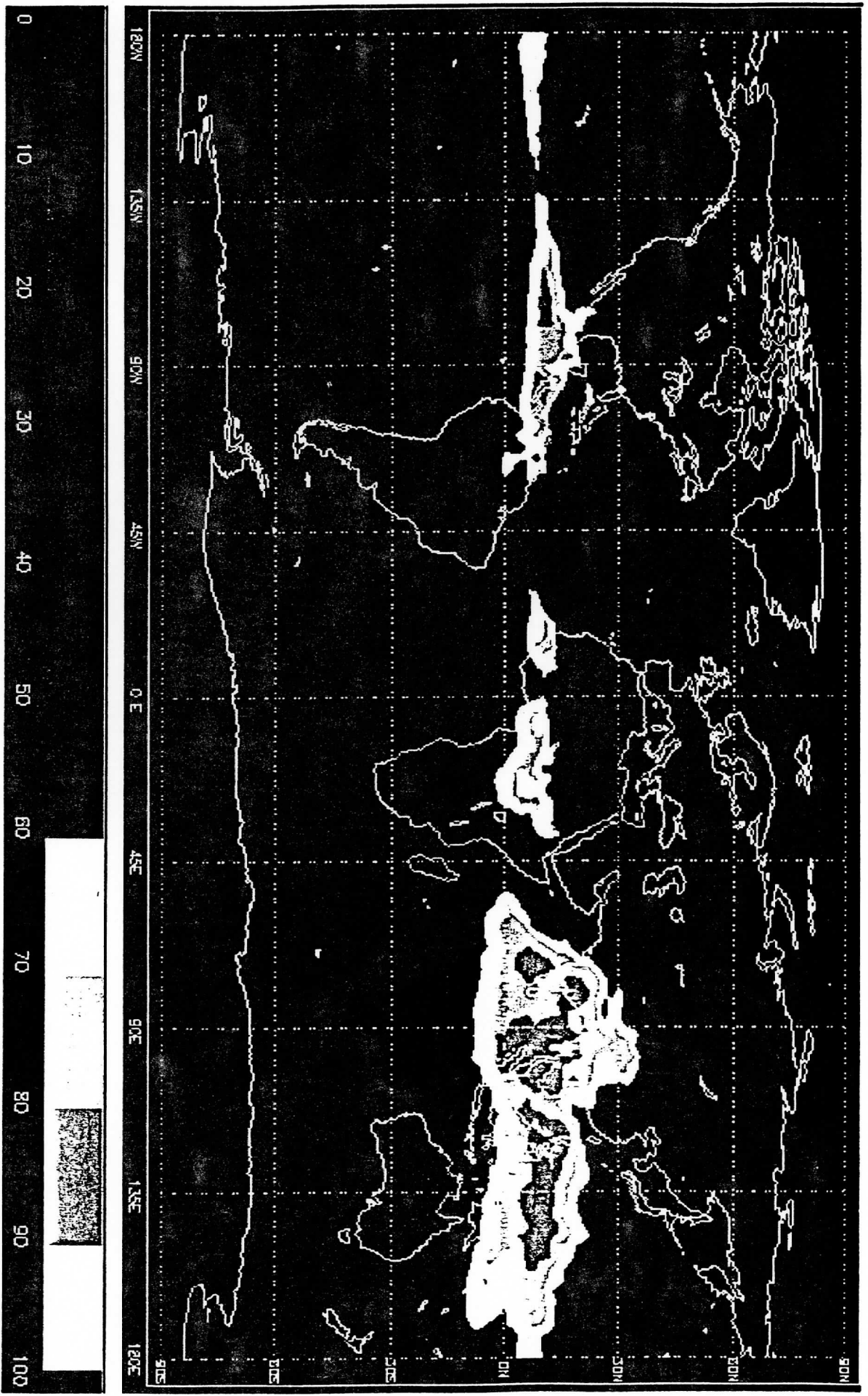


Figure 1

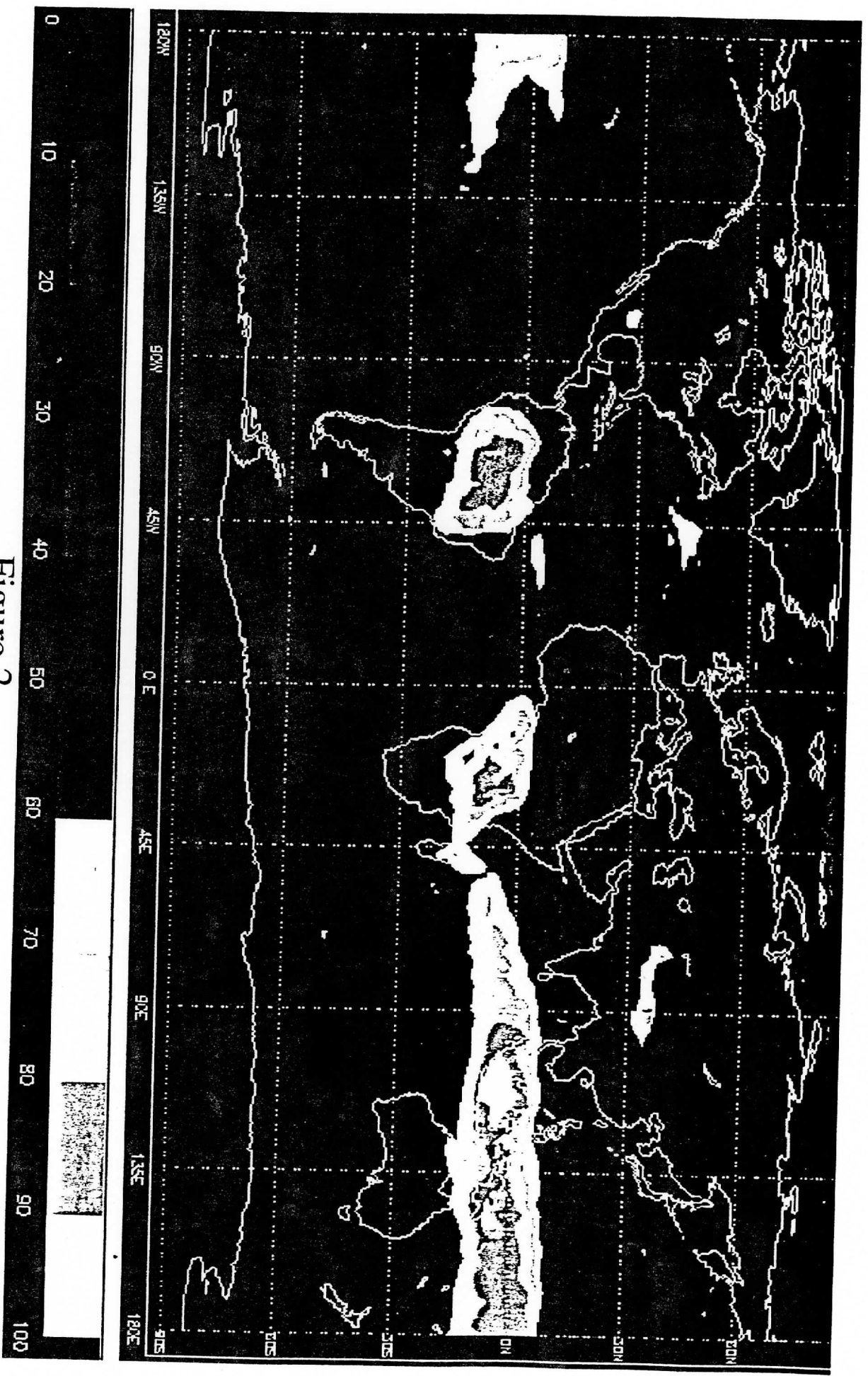


Figure 2

University of Wisconsin HIPS-2 Cloud Climatology  
Spring, Cloud Frequency of Occurrence at 6 Km and Above, All Thicknesses

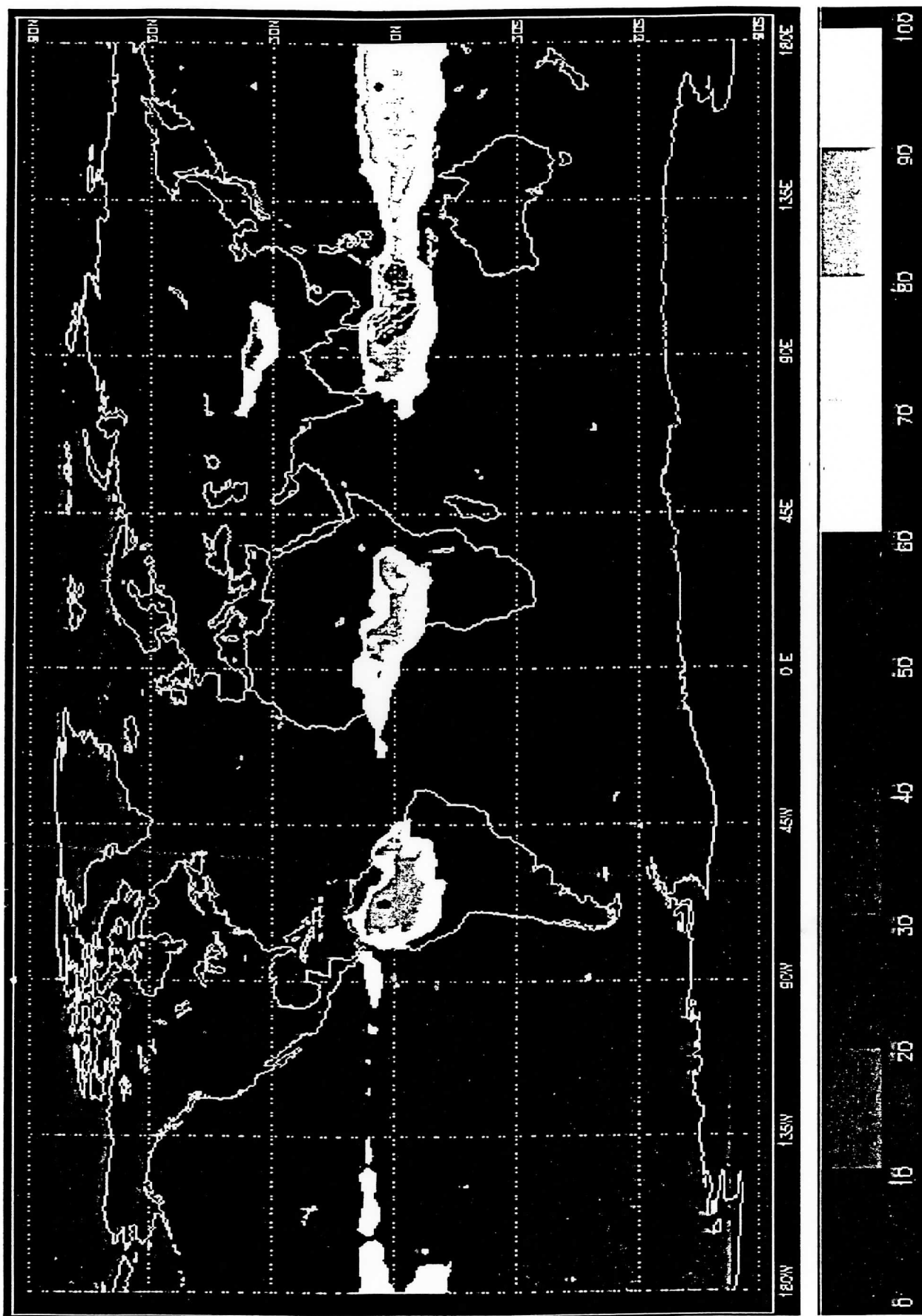


Figure 3

# University of Wisconsin HIRS-2 Cloud Climatology Fall, Cloud Frequency of Occurrence at 6 Km and Above, All Thicknesses

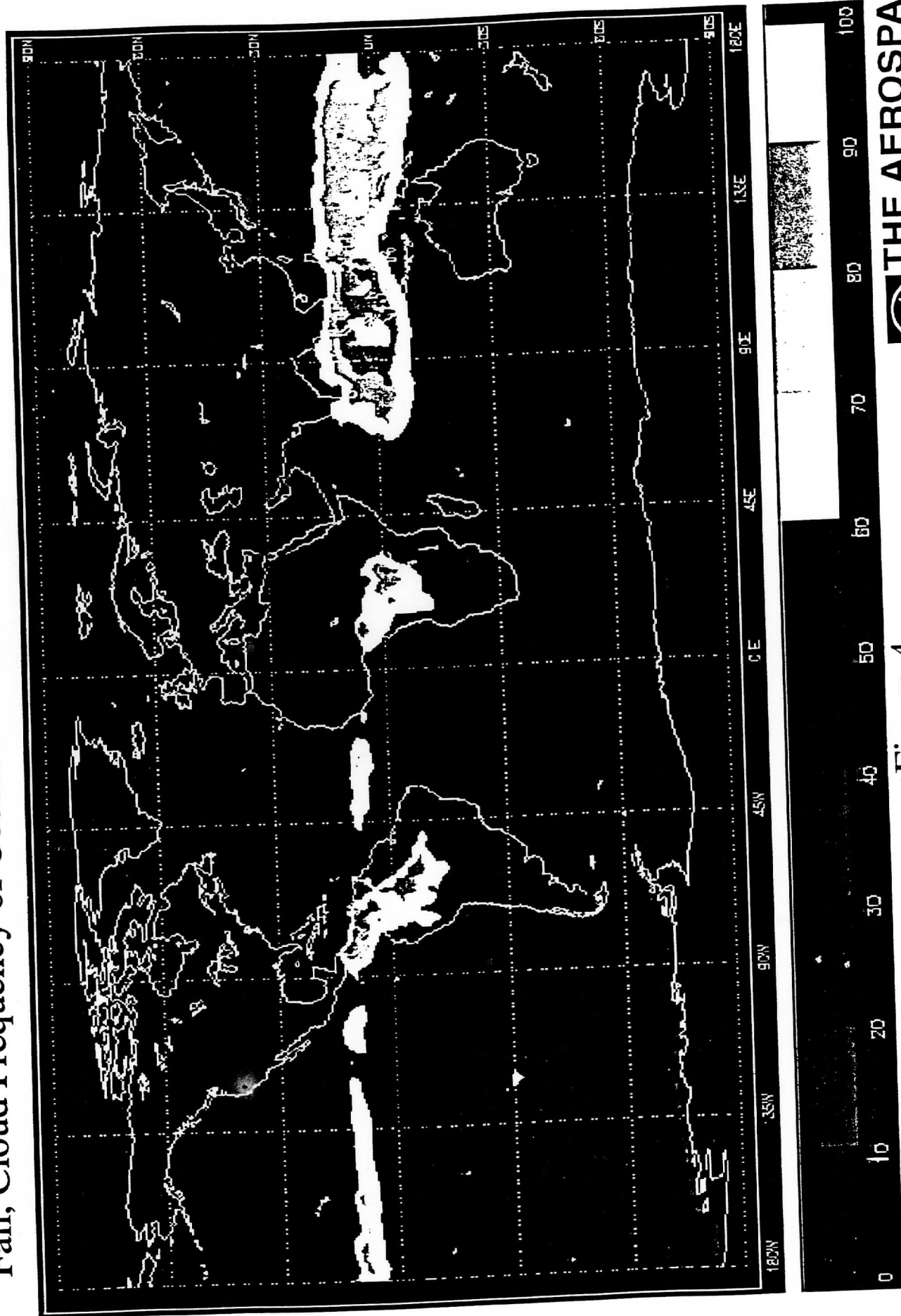


Figure 4

University of Wisconsin-Madison - Center for Global Change Science  
Summer, Cloud Frequency of Occurrence at 10 Km and Above, All Thicknesses

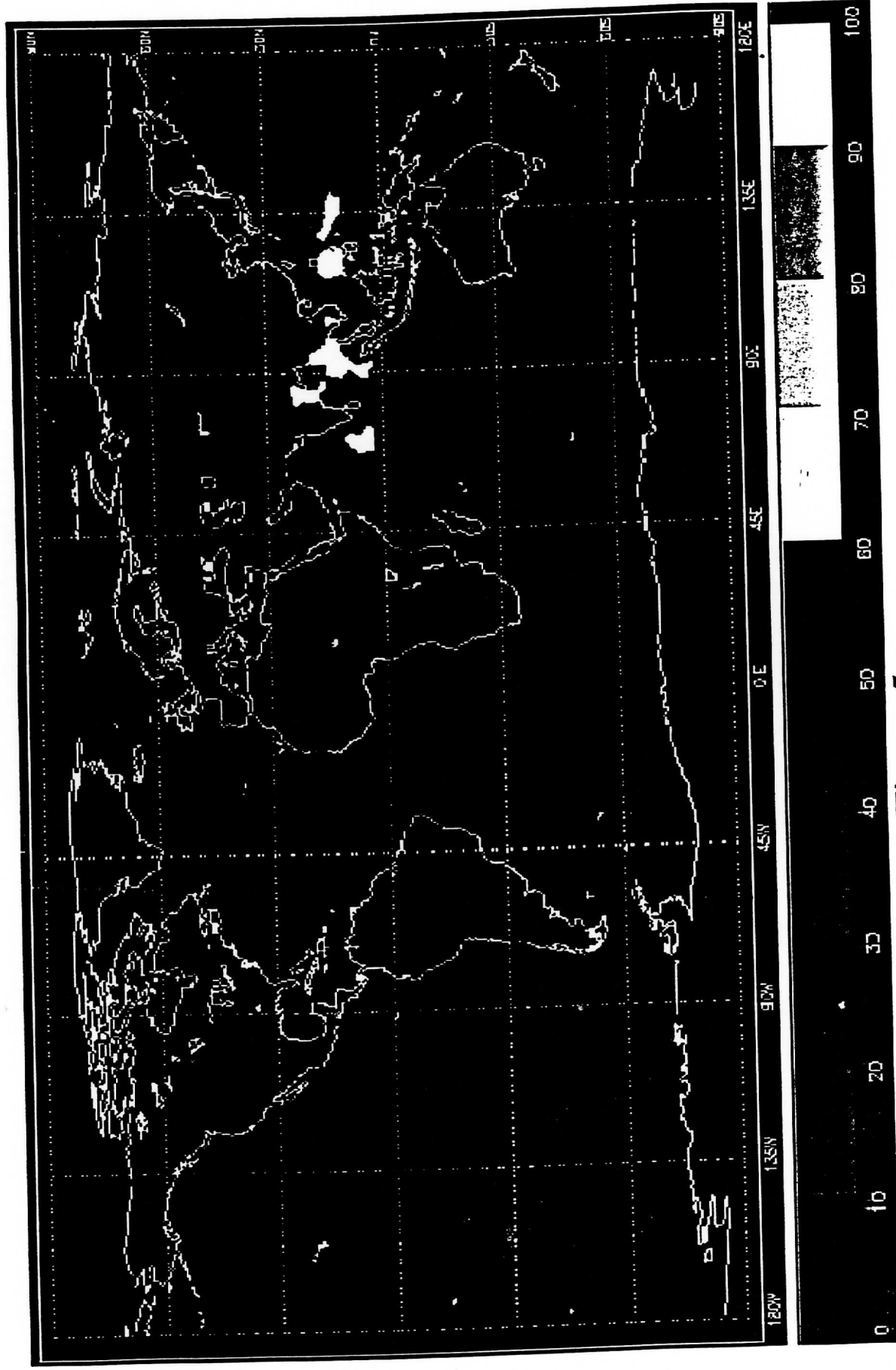


Figure 5



University of Wisconsin-MRC 2 Cloud Climatology  
Winter, Cloud Frequency of Occurrence at 10 Km and Above, All Thicknesses

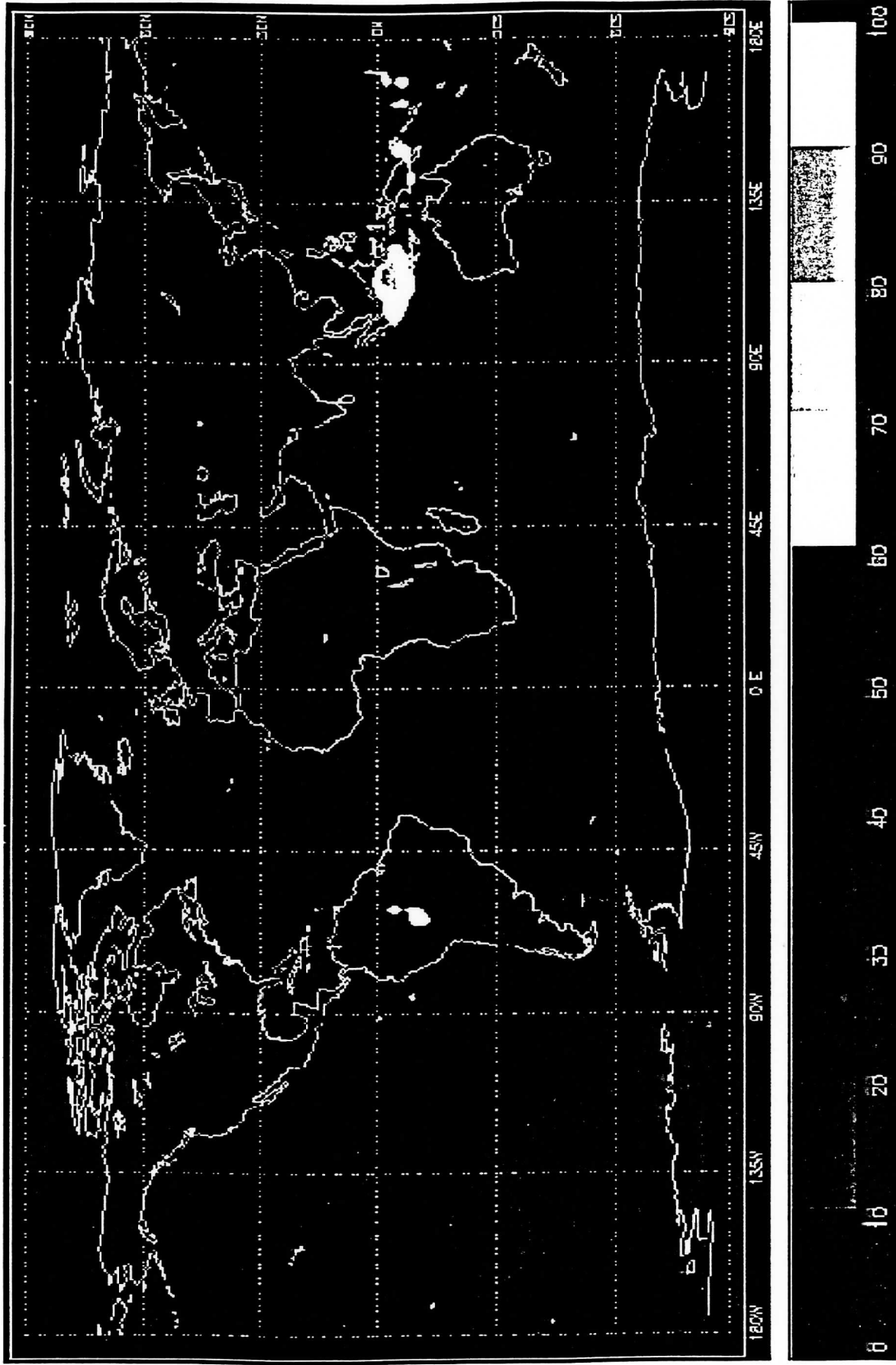


Figure 6

University of Wisconsin HIRS-2 Cloud Climatology  
Summer, Cloud Frequency of Occurrence at 4 Km and Above, All Thicknesses

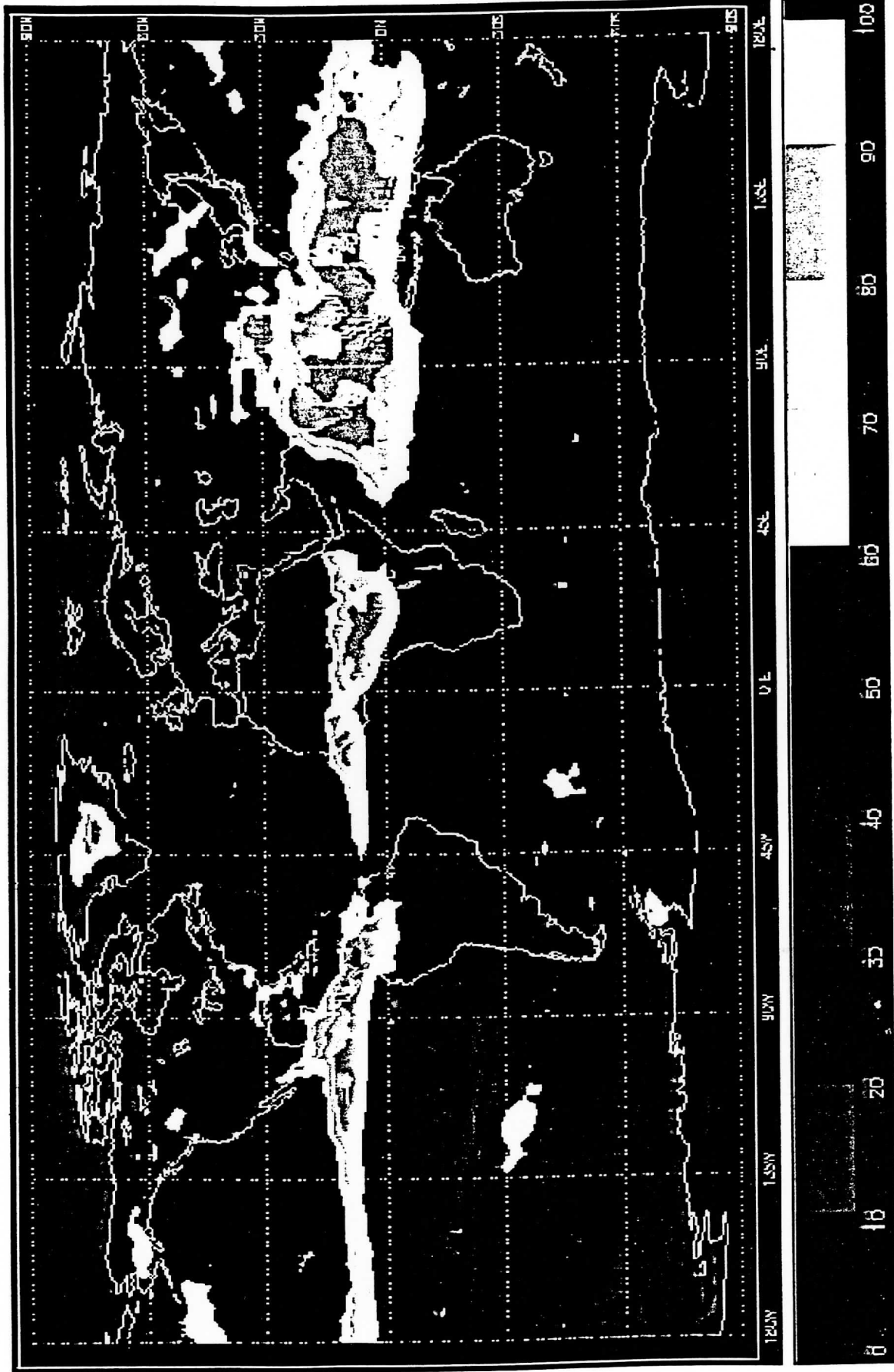


Figure 7

University of Wisconsin-Milwaukee HIRS-2 Cloud Climatology  
Summer, Cloud Frequency of Occurrence at 8 Km and Above, All Thicknesses

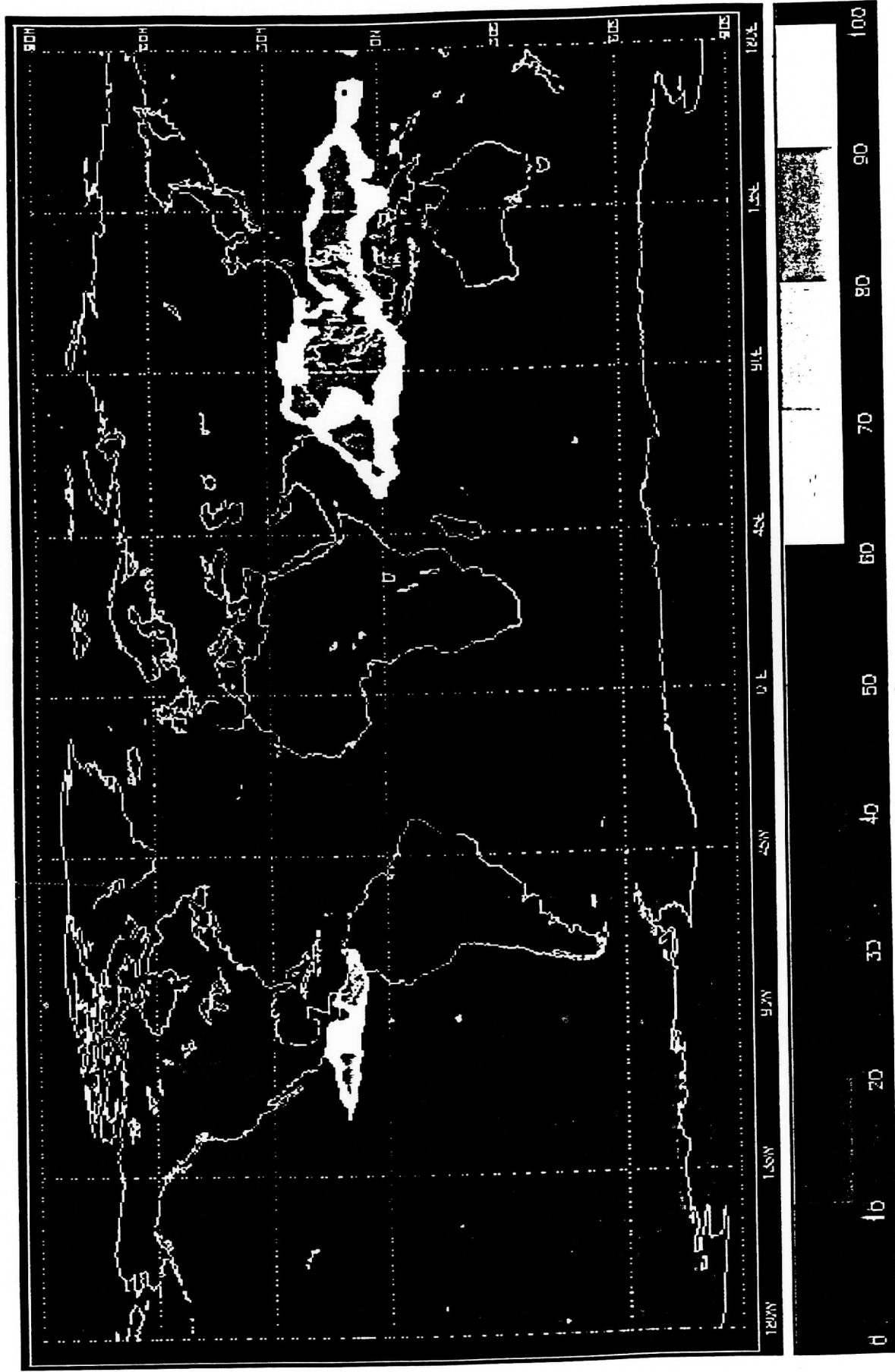


Figure 8

University of Wisconsin-MRC 2 Cloud Climatology  
Summer, Cloud Frequency of Occurrence at 6 Km and Above, Emissivity > 50%

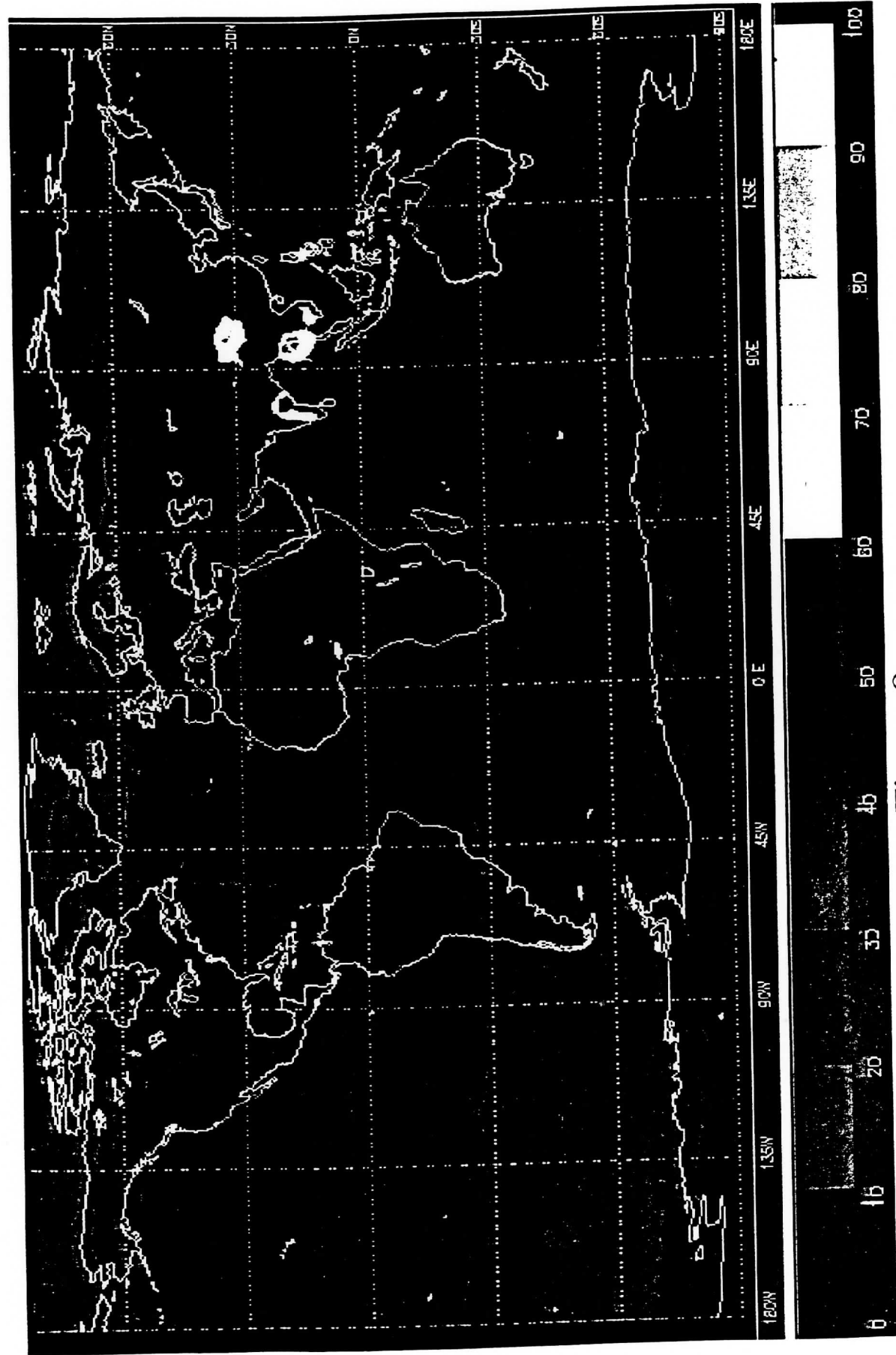


Figure 9

## **2.5 Biases and Errors in the UW Data**

References 9 and 10 describe a number of minor errors and biases that may result in the processing of the HIRS-2 data. The two most important findings are a 70 mb average error in cloud top pressure estimates as compared to lidar data (taken with only single cloud layers present) and a variable 50 to 150 mb error when partially transmissive clouds are present above lower altitude clouds (estimated to occur 50% of the time clouds are present). Lidar signals are routinely used to develop three-dimensional profiles of clouds and provide very precise cloud top information.

The cause of the 70 mb bias is not known, but may represent the difference between the exact cloud top, measured by lidar, and the average altitude of cloud emissions sensed by the HIRS-2. The multi-layer error occurs only when the top layer is not fully opaque. The size of this error, in mb, decreases with the altitude and opacity of the upper cloud layer, and increases with the altitude of the lower cloud level.

It may be possible using the HIRS-2 channels already included, or by adding some of the other 16 HIRS-2 channels to the analysis, to identify when multi-layer clouds are present and causing an error. If the lower altitude clouds can be identified, then the error can be eliminated and the characteristics of the lower cloud level can be reported.

### 3. Global High Cloud Data

This section describes the types of clouds found at high altitude and discusses the geographic and seasonal variations in cloud presence at different altitudes. Several color maps are included to aid in the visualization of cloud distributions. Cloud frequency distributions are shown at altitudes thought to be relevant to current surveillance requirements. Any combination of cloud altitudes and emissivities/transmissivities can be mapped or tabulated with an on-line tool at Aerospace.

#### 3.1 High Clouds

There does not seem to be a definition of high clouds unanimously agreed upon in the meteorological community. For the purpose of this report clouds at and above 6 km will be considered as high clouds. Clouds above 6 km tend to be dominated by ice particles rather than water droplets, which is not surprising when one considers the low temperature of air at these heights. The majority of clouds in this regime are cirrus (Ci) clouds.

The term cirrus cloud encompasses a vast array of cloud shapes, thicknesses, and particle types. Ci clouds are generally categorized as having low to moderate optical depths. Depending on the angle through which IR radiation passes, and the wavelength of the radiation, multiple scattering processes may allow a measurable amount of target signal to be transferred through a Ci cloud.

In the visible part of the spectrum, ice and liquid water have essentially zero absorptivity and ground observers may readily image the sun or the moon through Ci clouds. The reader's judgment of cloud opacity should not be biased by visual observations through clouds. At wavelengths longer than  $\sim 1.5 \mu\text{m}$  the material properties of both ice and water are drastically different than in the visible; with the absorptivity of each water droplet or ice particle increased many orders of magnitude over the absorptivity in the visible. Cloud opacity is discussed in Section 3.4.

The other type of cloud found at high altitudes is the cumulonimbus (Cb) cloud. In regions of very high convective activity, cells of moisture with significant vertical extent can ascend to very high altitudes. These cells may be capped with ice. The significant vertical extent and high water content of Cb clouds renders them effectively opaque.

#### 3.2 Seasonal Variations

The distribution of high altitude clouds is correlated with the amount of heat and moisture available in an area. In general, higher amounts of high clouds are reported in local summer than in other seasons. Similarly, higher levels of high clouds are present above land areas than above ocean regions. The regions with the highest frequency of high clouds (and the highest clouds) are equatorial zones.

Figures 1, 2, 3, and 4 show the global frequency of occurrence for clouds at or above 6 km in summer (June, July, August), winter, spring, and fall, respectively. In each figure, the statistics include clouds of all opacities. To create these seasonal maps, the number of clouds whose tops were at pressures below 500 mb totaled at each grid point. Frequency of occurrence is determined by dividing each total by the number of observations. All maps have been smoothed using bilinear interpolation to remove the pixelization inherent to the display.

The altitude corresponding to 500 mb in a mid-latitude summer atmosphere (Ref. 11) is about 5.7 km. Recognizing that a ~70 mb bias may be inherent to the data, we have adjusted the 5.7 km value upward to an integer height of 6 km, an adjustment less than 70 mb. Had we modified the 500 mb level by 70 mb, so that Figures 1 through 4 represent clouds whose tops are at pressure levels less than 430 mb, Figures 1 through 4 would be labeled as clouds at 7.0 km and above. No adjustment has been made for possible errors due to the presence of multiple cloud layers. Given the known biases and errors of the data, the reader should consider the lower bound of cloud altitude in Figures 1 through 4 to be greater than 6 km.

Figures 1 through 4 show that high clouds are most prevalent in regions within 20° of the equator. Figure 1 shows that in summer, southern Asia frequently has clouds at or above 6 km. Significant portions of India, Pakistan, China, Vietnam, and North Korea experience clouds at this altitude  $\geq 40\%$  of the time. Millions of square kilometers of the Earth's surface are shown to have clouds at or above 6 km at least 70% of the time. The reader is reminded that all figures display average results over a span of 4 years. Reference 7 reports year-to-year variations with significant fractions of the reported frequency in some regions.

As seasons change, the total amount of high cloud cover is relatively constant, though clear geographic differences are observed. For example, Iran and Iraq are essentially free of high clouds in summer and fall. However, in winter and spring Iran has high clouds 30 to 40% of the time while Iraq has high clouds slightly less frequently.

Figures 5 and 6 show the cloud cover at 10 km and above in summer and winter, respectively. As with the earlier figures, an altitude adjustment has been included. The frequencies shown in Figures 5 and 6 represent UW data points with cloud top pressures at less than 300 mb. In a mid latitude summer atmosphere 300 mb corresponds to ~9.5 km. Again, the lower altitude bound has been rounded up to an integer value (a 20 mb adjustment). The altitude corresponding to 230 mb is ~11.4 km.

### 3.3 Altitudinal Variations

Figures 5 and 6 show that the geographic locations with significant cloud cover above 6 km have also relatively frequent cloud cover above 10 km. Figure 5 also shows that many regions in summer, particularly those above 50° N, have clouds at 10 km or above, from 0 to 10% of the time. Figure 6 shows that in winter, the region around Iran and Iraq has clouds above 10 km, from 0 to 10% of the time, although portions of both countries are covered with clouds above 10 km in spring.

Figures 7 and 8 provide additional insight into the variation of cloud frequency with altitude, showing clouds above 4 and 8 km, respectively. Note, if one were to apply a 70 mb correction to these data, they would represent clouds above 4.7 and 9.0 km, respectively. Combined with Figures 1 and 5, they show the distribution of clouds in summer as the minimum cloud altitude changes from 4 to 10 km. The relative frequency of occurrence of clouds is well correlated between the Figures. The color contours evident in Figure 1, showing clouds 6 km and above, are clearly evident for clouds above 4 km. The latter map simply shows one decile (one color level) of percentage higher frequency of occurrence. Similarly, the difference in frequency for clouds above 6 km and as compared to 8 km is also about one decile. For example, the De-Militarized Zone (DMZ) between the Koreas drops from 50% frequency for 6 km and above, to 40% frequency for 8 km and above.

The change from 8 to 10 km is more pronounced. Most areas show ~20% lower frequency of occurrence for clouds above 10 km compared to those above 8 km. The DMZ shows about 20% frequency of occurrence for clouds above 10 km. The relative changes with altitude are similar in winter.

As discussed above, there is substantial disagreement among the various cloud climatologies as to the absolute frequency of high cloud presence. We believe the techniques used to create the UW data and the level of validation reported justify its use as "truth". The validation efforts indicate that the cloud top pressures reported in the UW climatology are low by an average of 70 mb. There are also errors, typically about 100 mb, in reported cloud top height when multiple layers of clouds are present and the upper layer is partially transmissive.

These two effects combine such that it is likely that, on average, the UW data reports cloud top pressures ~100 to 110 mb too high. Here we have summed 70 mb of bias with a 30 to 40 mb component, taken to be the average error resulting from multiple cloud layers. Multiple cloud layers occur about 50% of the time during which clouds are present, and 60 to 80 % of high clouds are partially transmissive in the vertical direction; aggregately, this error affects 30 to 40% of the UW data. When present, the typical multi-cloud error is 100 mb. Thus, a 30 to 40 mb error will result when observed over a large data sample. Refinement of the correction to the cloud altitudes is an



area for future collaboration with UW.

A. Dalcher has developed seasonal cloud climatologies using SAGE-II data from 1984 to 1990 (Ref. 11). To provide meaningful statistics, the 6-year data sets are averaged over large areas. Table 1 shows the frequency of clouds, in summer, above several altitude bounds derived from SAGE-II. The statistics are provided for the geographic region bounded in latitude by parallels at 20 and 40° N and in longitude by meridians at 80 and 130° E. This region includes the Korean peninsula and most of the People's Republic of China.

Table 1. Cloud Frequency of Occurrence Above Altitude in Summer

Lower Altitude Bound (km)	Sage-II Data at Dusk (%)	Sage -II Data at Dawn (%)	UW Data (%)
4	88	92	69
6	68	81	58
8	58	68	48
10	47	51	32
12	31	39	

A comparison of Figures 1, 5, 7, and 8 with the SAGE values shows that there is substantial variation across the region and that the SAGE-II values are somewhat higher than those mapped from the UW data. If one modifies the UW cloud altitudes according to a pressure error of 100 to 110 mb then the UW results shown in Table 1 would correspond to altitudes of 5.9, 7.6, 9.7, and 12.4 km, respectively, in a mid-altitude atmosphere model. The frequency of occurrence, at these altitudes agrees within 1% of the frequency of the SAGE Dusk data at the nearest altitude level. Detailed comparisons of different climatologies will be reported in a follow-on report.

The UW data, as supplied, does not include HIRS-2 data from the morning pass over land areas. The statistics in Table 1 are for a region almost entirely covered by land. Thus, this data is an average of nighttime and afternoon cloud cover and should be compared to SAGE data taken at local dusk. This comparison supports an adjustment to the UW altitudes corresponding to ~100 mb of atmospheric pressure. The comparison also brings to light potentially significant variations in cloud cover during the diurnal cycle. Another area of potential collaboration with UW is to examine the HIRS-2 morning data over land.

### 3.4 Cloud Opacity

The final map, Figure 9, shows the frequency of clouds above 6 km (same altitude caveat applies as for Figures 1 through 4) for those clouds of Ne product greater than 50%. Recall the

emissivity is measured at 11.1  $\mu\text{m}$  in a nearly vertical direction. Most clouds have virtually no reflective component at this wavelength. Conservation of energy argues that radiation not reflected is either absorbed or transmitted. Clouds in radiative equilibrium (assumed to be the case) will have an emissivity equal to their absorptivity. Thus, at 11.1  $\mu\text{m}$ , the transmissivity (T) of a cloud is equal to 1 minus  $\epsilon$ .

Reference 7 describes comparisons of the HIRS-2 20 km data with simultaneous 1 km imagery from the Advanced Very High Resolution Radiometer-2. In the vast majority of cases, variations from near unity in  $N\epsilon$  are due to emissivity rather than cloud fraction when  $N\epsilon$  is greater than 50%. Assuming this to be true, the UW data can be used to draw conclusions about the frequency of cloud opacity.

Clouds with emissivity of 50% or more will have transmissivity less than 50% in a vertical or zenith direction. As the angle of viewing departs from cloud zenith, the optical path through a cloud increases; resulting in an increase in apparent optical depth. The transmission level decreases geometrically with the length of the path,  $p$ , through the clouds. Equation 1 shows a good approximation for the amount of radiation scattered through the cloud for paths at the look zenith angle (LZA). The LZA is illustrated in Figure 10. Essentially, none of the radiation is directly transmitted through the clouds. The effective (also called diffuse) transmission is the fraction of radiation not absorbed nor scattered out of the LOS of a sensor.

$$T_{LZA} = T \exp(p) \tag{1}$$

$T_{LZA}$  = Effective transmission at angle LZA, an angled measured from cloud zenith  
 $T$  = Effective transmission at zenith  
 $p$  = path length at angle LZA

$$p = 1/\cos(LZA) \tag{2}$$

For example, a cloud with transmissivity of 50% at zenith will have only 25% transmissivity at an LZA of 60°. The same cloud will have about 13% transmissivity at 70° LZA, 7% transmissivity at a zenith angle of 75°, and only 2% at 80°.

Figure 9 shows the global distribution of clouds above 6 km that allow less than half of the signal from a target to penetrate the cloud in the vertical. These clouds are much less transmissive at higher LZAs. A comparison of Figures 1 and 9 shows that roughly two-thirds of the clouds above 6 km have transmissivity less than 50%. A significant number of the clouds shown in Figure 9 have

transmissivity less than 25% in the vertical. A discussion of zenith angles relevant to different surveillance systems and translation of emissivity/transmissivity from 11.1  $\mu\text{m}$  to other wavelengths is presented in the next section.

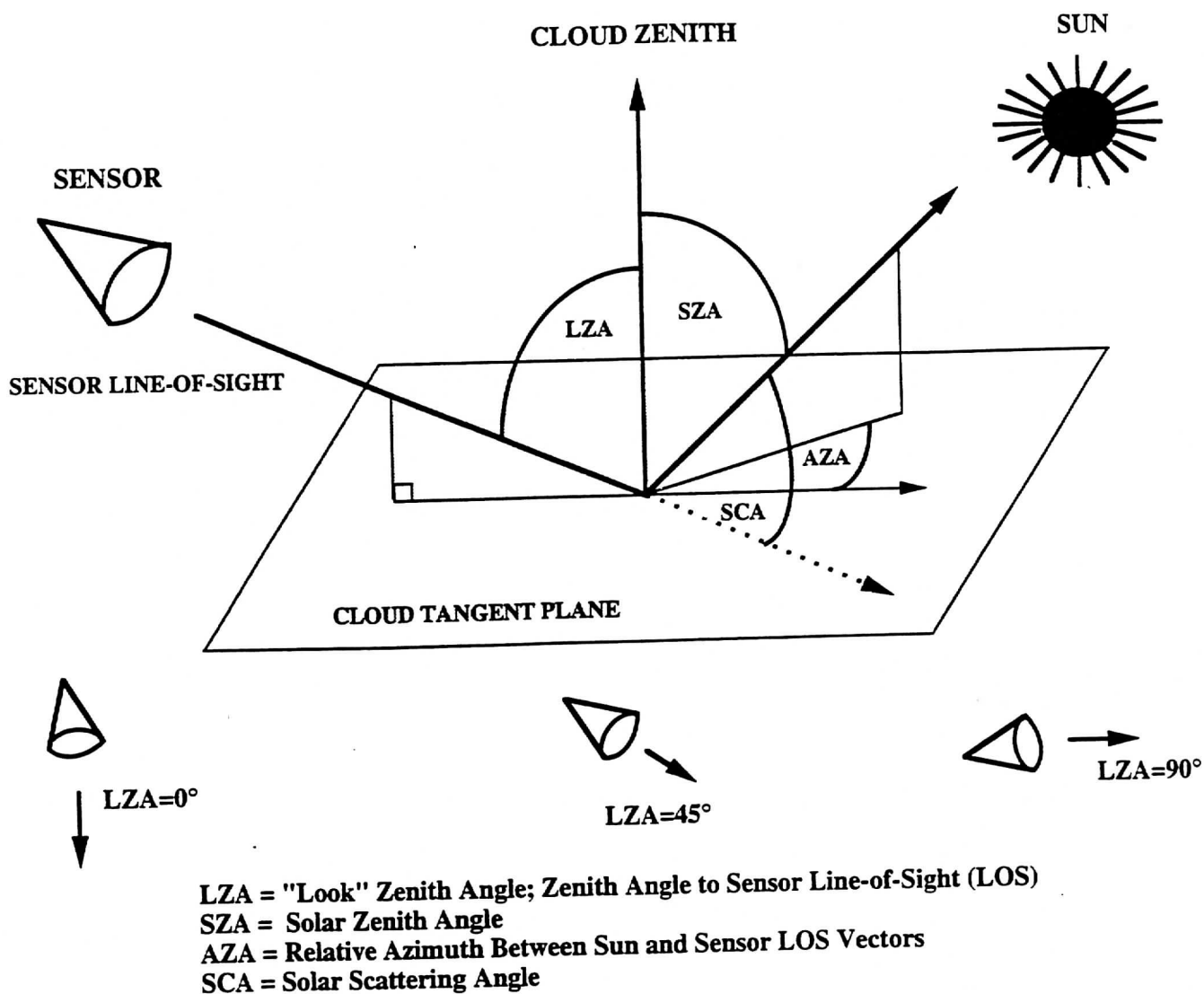


Figure 10. Satellite coordinate system.

## 4. Cloud Obscuration and Clutter

This section summarizes cloud presence at high altitude. As not all clouds are opaque, the dependence of cloud opacity on spectral band and sensor look zenith angles is discussed for different surveillance systems. Lastly, the ramification of cloud presence at altitude to frequency of occurrence of clutter is discussed.

### 4.1 Clouds at Altitude

The various maps of cloud frequency of occurrence leave no doubt that clouds at relatively high altitude are a common phenomenon. Given the year-to-year variations observed in cloud cover at high altitude, it is possible for locations near North Korea to have 6 km clouds over 60% of the summer. Similarly, in spring, portions of the Middle East could have high cloud cover 50% of the time.

Cloud presence is neither a spatially nor a temporally random phenomenon. Anyone who has looked at the weather photos shown on the nightly news knows that cloud systems may extend for over 1,000 km and persist for periods from hours to days. Atmospheric circulation may bring several systems across a region in succession.

The main message is that there are many regions of interest on the globe for which planners of IR surveillance systems should anticipate the presence of extended periods of high cloud cover. The frequency of occurrence of clouds shown in Figures 1 through 9 is a strong indicator of how often an IR sensor will not be able to detect targets below cloud level. If the user of the IR detection data demands reliability of detection beyond that which clouds will allow, then IR surveillance may not be the appropriate detection solution.

Another point to consider is that the UW data only reports the altitude of the highest cloud layer observed. Reference 6 reports that comparisons of the UW data with ground reports reveal that about one-half the time there is a lower altitude cloud deck. Thus, even if the highest layer of clouds present is partially transmissive, there is a reasonable chance that there are additional cloud obscuration sources present. In the future, we will try to report on the probable altitudes for underlying cloud layers.

For the purpose of cloud obscuration, the total cloud cover amount is of importance. Not all of the UW observations represent solid cloud decks. However, the apparent gaps between clouds diminish with LZA. In the future, we will report total amount of cloud cover and extrapolate for

different viewing angles. Analysis being performed by ISCCP personnel may prove valuable in this area.

#### **4.2 Dependence of Obscuration on Spectral Band**

The dependence of cloud opacity on wavelength results from two primary sources. First, there are pronounced variations in refractive indices of water and ice with wavelength which affect the relative amounts of reflection and absorption in clouds. Second, the efficiency of scattering and the directionality of the scatter are functions of size of cloud particles relative to the wavelength.

Ice crystals can take on a large variety of shapes and orientations. The practice of predicting the scatter in ice clouds is immature at this time and is only conducted by a few specialists in the meteorological community. For wavelengths much smaller than the sizes of cloud particles, the shape of the particle is not very important to the amount of scatter. Fortunately, for our analysis, many particles in Ci clouds are far larger than both the wavelengths of interest to the IR surveillance community, 2 to 12  $\mu\text{m}$ , and the 11.1  $\mu\text{m}$  wavelength of the UW emissivity data. For the purpose of translating emissivity from one wavelength to another in the 2 to 12  $\mu\text{m}$  waveband, we can ignore the irregular shapes and particle orientations of ice clouds. The important factors in this translation are the change in the refractive indices of ice and water over the wavelengths of interest.

Though the properties of atmospheric water vapor are markedly different between 11.1  $\mu\text{m}$  and the SWIR absorption band, the real and imaginary indices of refraction for ice and liquid water are quite similar in the two spectral regions (Ref. 12). The transmissivity of the cloud depends very strongly on the amounts of scattering and absorption within the cloud. The optical depth of a cloud,  $\tau$ , describes the average number of particle interactions, or bounces, that will occur as a beam of light passes through a cloud. The single scatter albedo,  $\omega_0$ , is the fraction of the light scattered, not absorbed, per bounce. The single scatter albedo for Ci cloud ice particles is comparable for the SWIR band and 11.1  $\mu\text{m}$ . To a good approximation, the transmissivity reported by the UW data should be considered to be a reasonable approximation to the transmissivity in the SWIR band.

There are several wavelengths between 2.0 and 2.5  $\mu\text{m}$  and within the 3 to 5  $\mu\text{m}$  band at which ice clouds are more transmissive than at 11.1  $\mu\text{m}$ . Candidate surveillance bands, exploiting higher cloud transmissivity, will be examined and reported in a follow-on report.

#### **4.3 Dependence of Obscuration on Zenith Angle**

Two primary effects occur when clouds are viewed at increasing look zenith angle. As described above, the path through the cloud increases, reducing the level of transmission. Second,

physical gaps in clouds, which may provide limited amounts of CFLOS will appear to be smaller due to geometrical foreshortening.

Space-based surveillance systems view targets and clouds at a variety of LZAs. Constellations employing orbits at or near geostationary Earth orbit (GEO) will have a different distribution of viewing angles from highly-inclined constellations based in low-Earth orbit (LEO), i.e., below 5,000 km altitude. In general, regions below 45° N latitude will be viewed at LZAs of less than 60° by a GEO constellation. Higher latitude regions, which have a much lower frequency of high clouds, are viewed at higher (worse) LZAs. The distribution of viewing angles does not vary as much with location for a LEO constellation. However, the LEO constellation will typically view regions at much higher LZAs than a GEO constellation. A significant fraction of scenarios have a LEO constellation viewing regions at LZAs greater than 70°.

The major ramification of different LZA distributions is that a LEO constellation will have a lower probability of CFLOS than a GEO constellation. The probability of CFLOS at viewing angles of LZA greater than 0° is lower than at LZA=0°. The difference in probability of CFLOS will only be significant when a small amount of cloud is viewed at very high LZA; under this circumstance the small amount then appears to be a large amount of cloud. This combination of small cloud amounts and very high LZAs occurs only a low fraction of the time. Reference 14 contains information on the change in the probability of CFLOS with LZA.

When clouds that are partially transmissive (in the vertical direction) are present, they will be effectively opaque more frequently to the LEO constellation (due to higher average LZA). Only in a small fraction of cases will clouds be sufficiently transmissive that the GEO constellation could detect a target before cloud break whereas the LEO constellation will not detect the target until it is above the clouds.

Airborne surveillance systems typically view targets near the local horizontal or near an LZA of 90°. Such viewing angles are needed to allow long-range acquisition of targets. The horizon is less than 20 km distant to a sensor flying at 10 km, pointed 20° below horizontal (LZA 70°). With near-horizontal geometries common to these systems, essentially all clouds reported in the UW data should be considered opaque. The probability of obtaining a CFLOS will be primarily determined by the altitude of the platform.

To better support selection of aircraft platforms to carry surveillance sensors, we will try to report cloud altitude information with less ambiguity in the future. It is recognized that the ceiling

limitations of some potential platforms may preclude their use, limit their endurance, or limit their payload capacity in regions with very high clouds (above ~10 km).

#### **4.4 Clutter Induced by Clouds**

Clutter is a term used to describe the interaction of the natural background with the sensor detection process. Clutter results when the natural background produces signals that are initially interpreted as targets. A primary source of clutter in the SWIR absorption band are solar reflections from clouds.

In the SWIR absorption band, the transmission of the atmosphere decreases rapidly with the altitude traversed by light. Absorption of sunlight, due to gases, occurs on the incident path from the sun to a cloud and on the path of reflection to a sensor. Thus, cloud altitude is an important factor in determining the brightness of the background. Other factors are also important such as the reflectivity of the cloud and the solar scatter angle (see Fig. 10). Indications in the literature are that clouds at higher altitudes contain less water and have particles of dimensions closer to the SWIR wavelengths. Both of these characteristics contribute to higher levels of reflection for higher clouds.

The trends in transmission and reflectivity with cloud altitude indicate that the level of SWIR clutter will be well correlated with cloud altitude. If so, then a high fidelity cloud climatology will provide information crucial to the prediction of clutter level.

A number of clutter (sensor performance) predictions have recently been performed for studies in the Space-based IR surveillance community. These predictions have emphasized backgrounds dominated by clouds at 6 and 10 km, respectively. The question of the frequency of occurrence of clouds at these altitudes has been frequently raised.

Figures 1 through 9 argue that 6 km clouds are a frequent occurrence. Clouds at or above 10 km occur often enough that they must be considered an issue over most geographical regions of interest. It is important to note that the frequencies described in the figures provide lower bounds on the amount of time clouds are present.

Acquisition sensors must typically provide very high probability of detection while limiting false detections to nearly zero. Thus, it does not take much clutter or cloud amount to produce an intolerable number of false detections. A small amount of high clouds in a region is almost as bad as if the entire region were filled with high clouds. The spatial-temporal ambiguity in the UW data described in section 2.4 is significant for estimates of clutter. If a small amount of high clouds are

present in a region most of the time then the clutter level will be worse, on average, than if the region is mostly cloudy only some of the time. We hope that by examining the UW data at its original spatial resolution that a metric can be developed to discriminate spatial variability from temporal variability in each region.



## 5. Summary and Future Plans

This section summarizes the main points covered in this report and describes additional efforts which will be documented in a future report.

The significant points presented here are that, despite some disagreement in the available cloud climatology data, we contend that clouds are prevalent at high altitude in many regions of interest. Many of these clouds are opaque in candidate IR surveillance spectral bands and will obscure targets beneath the cloud level. Those clouds which are not opaque when viewed at normal incidence become more so as the angle of viewing moves away from vertical. For both space-based and air-based surveillance systems, there are proposed platform architectures which require the sensors to view clouds at very high look zenith angles; clouds viewed in this fashion will transmit very little if any target signal. In general, targets should not be considered accessible to IR detection systems when the target is located below cloud altitudes.

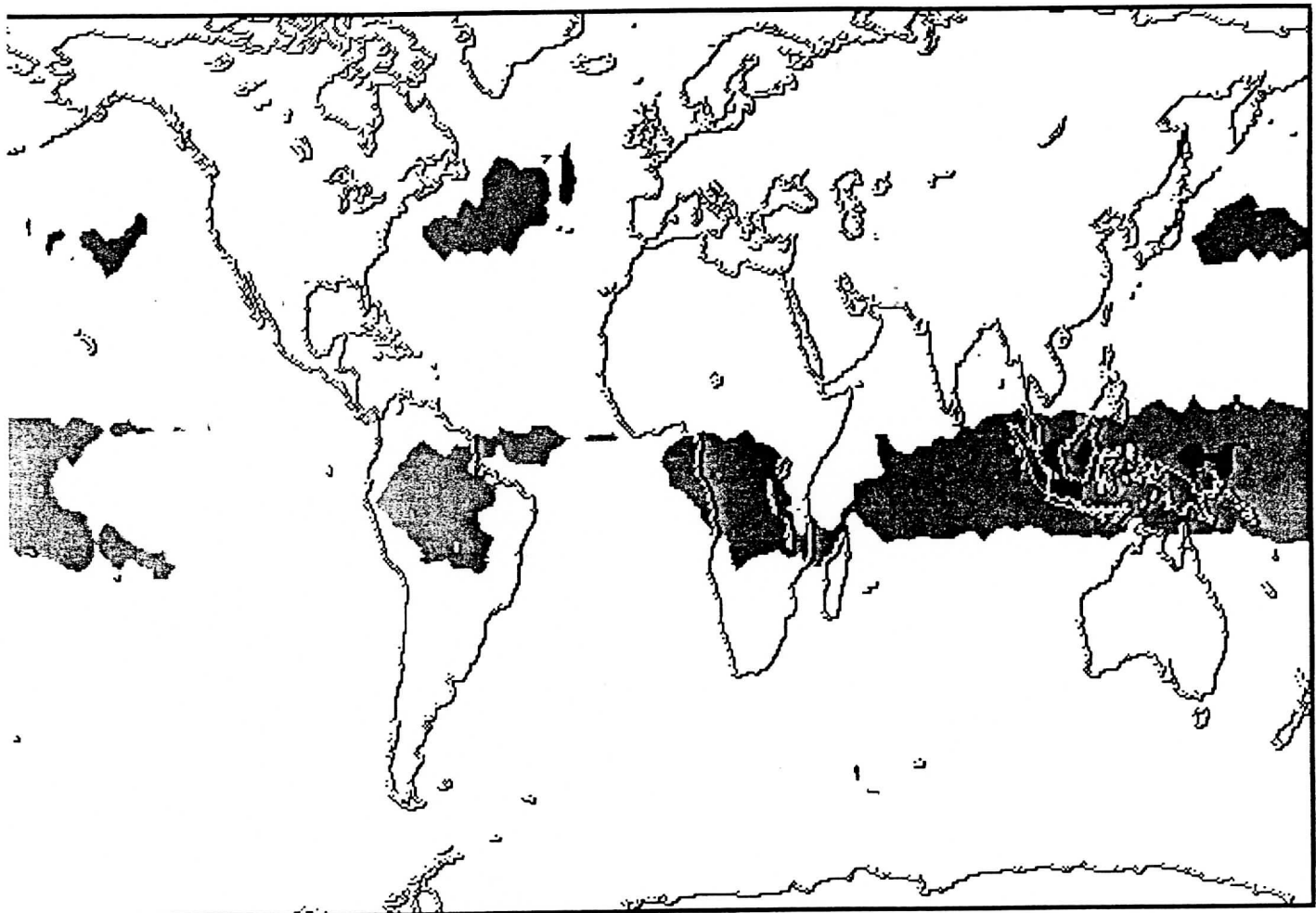
Cloud cover is highly variable in both time and location. Year-to-year variations of significant magnitude occur in many regions. There are still ambiguities in the spatial-temporal distribution of clouds and in their exact altitude distribution; both of which have system impact.

We hope to collaborate with UW to reduce ambiguities in the data and to examine cloud presence at finer spatial, temporal, and altitudinal resolution. We also plan to compare the UW to SAGE-II climatologies, to data from the ISCCP, and possibly with products of the USAF RTNeph. Comparisons will be made, where possible, with data from the same year(s), sampled at a comparable time of day. Quantitative tabulations in different regions and seasons will be provided in a follow-on report.

The follow-on report will also provide quantitative estimates of CFLOS to different altitudes as a function of zenith angle, season (or month), and location. Cloud opacity as a function of wavelength will be considered for candidate surveillance spectral bands.

## 6. References

1. Entremont, R. P. "Detection and Analysis of Cirrus Clouds Using Passive Infrared Satellite Data", in *Passive Infrared Remote Sensing of Clouds and the Atmosphere*, SPIE Volume 1934, D. K. Lynch ed., 1993.
2. Snow, J. W., "Review of Air Force Cloud Research-July 1991", in *Proc. of the Cloud Impacts on DoD Operations and Systems 1991 Conference*, D. Grantham and J. snow eds., 1991.
3. Lynch, D. K. "Subvisual Cirrus: What it is and Where you find it", in *Passive Infrared Remote Sensing of Clouds and the Atmosphere*, SPIE Volume 1934, D. K. Lynch ed., 1993.
4. Rossow, W. B. and R. A. Schiffer, *ISCCP Cloud Data Products*, BAMS Vol. 72, No. 1, January 1991.
5. Kidwell, K. B., *NOAA Polar Orbiter Data Uses Guide*, NOAA National Climatic Data Center, Satellite Data Services Division, 1991.
6. Woodbury, G. and M. McCormick, *Zonal and Geographic Distributions of Cirrus Clouds Determined From SAGE Data*, J. Geophysical Research, Vol. 91, No. D2, 2775-85, February 1986.
7. Wylie, D. , et al, *Four Years of Global Cirrus Statistics using HIRS*, Submitted to J. Climate.
8. Wylie, D. P. and Menzel, W. P. "Trends in global cirrus inferred from three years of HIRS data", in *Passive Infrared Remote Sensing of Clouds and the Atmosphere*, SPIE Volume 1934, D. K. Lynch ed., 1993.
9. Menzel, W. P., et al, *Seasonal and Diurnal Changes in Cirrus Clouds as Seen in Four Years of Observations with VAS*, J. Appl. Meteorology, Vol. 31, 370-385, April 1992.
10. Baum, B. A. and Wielicki, B. A., *Cirrus Cloud Retrieval Using Infrared Sounding Data: Multi-level Cloud Errors*, J. Appl. Meteorology, Vol. 33, 107-117, January 1994.
11. N.A., *MOSART Model Atmospheres*, Photon Research Associates Report R-106-92, 1992.
12. Dalcher, A., *Cloud-Free Line-of-Sight (CFLOS) Availability*, IOA Paper P-2655, Institute for Defense Analyses, 1992.
13. Liou, K. N., *Radiation and Cloud Processes in the Atmosphere*, Oxford University Press, New York, 1992.
14. Bauer, E., Bernstein, L., and G. Weyl, *Cirrus Clouds, some Properties and Effect on Optical Systems*, IDA Paper P-1743, Institute for Defense Analyses, January 1984.



PROBABILITY OF CIRRUS  
DEC - FEB 1989 - 93  
4 SEASON AVERAGE

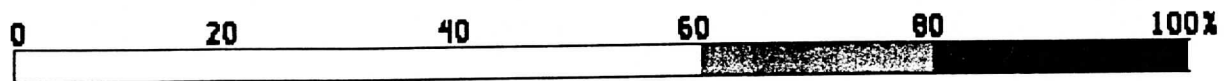


Figure 1: (b) The geographic frequency of transmissive clouds for the boreal winters (December, January, and February) during the observation period June 1989 thru May 1993.

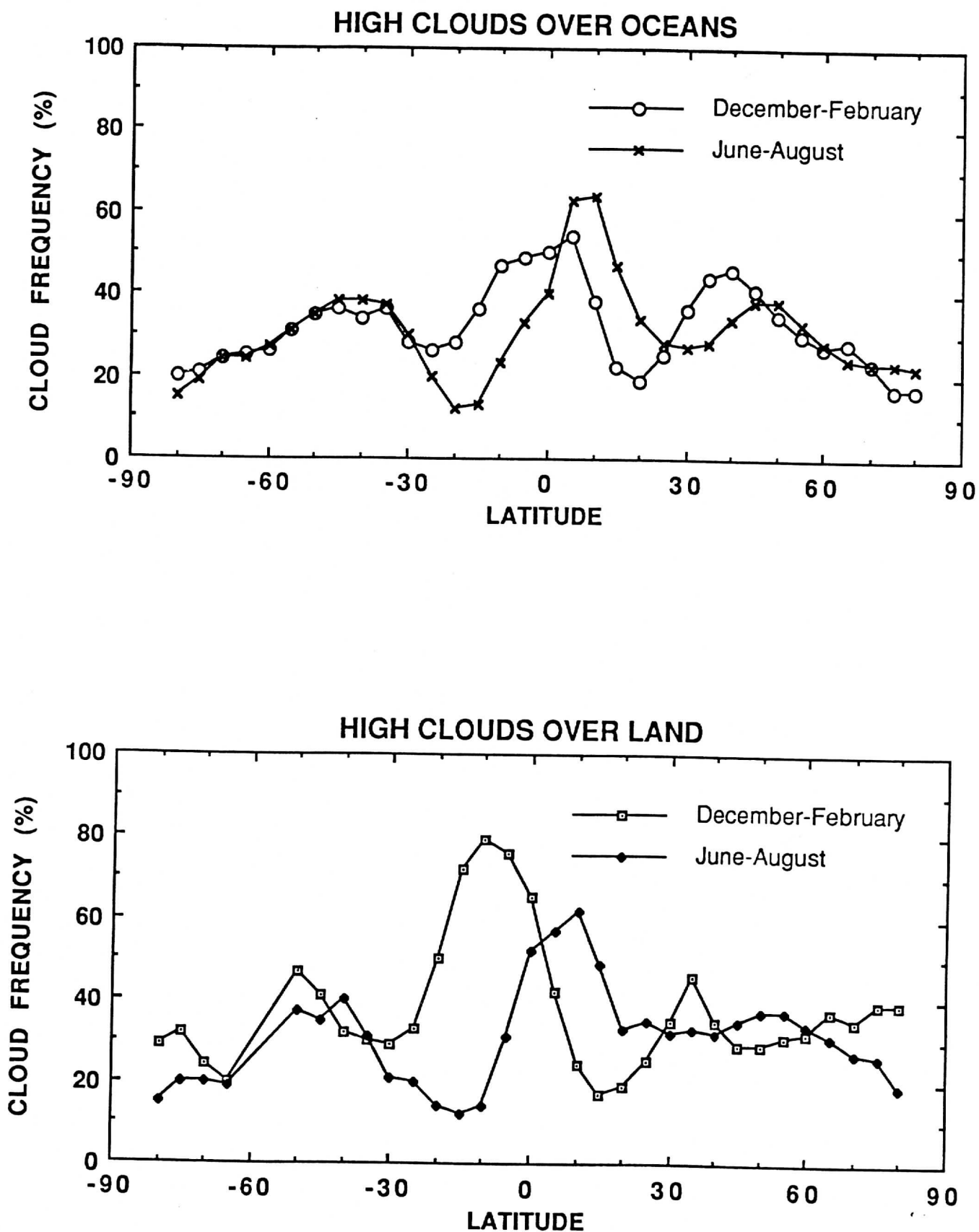


Figure 2: The frequency of high clouds (cloud pressure < 500 hPa) over ocean is shown in the upper panel as a function of latitude for the boreal summers (June, July, August) of 1989-92 and winters (December, January, February) 1989-93 expressed as a fraction of all satellite observations, clear and cloudy combined. The same over land is shown in the lower panel.

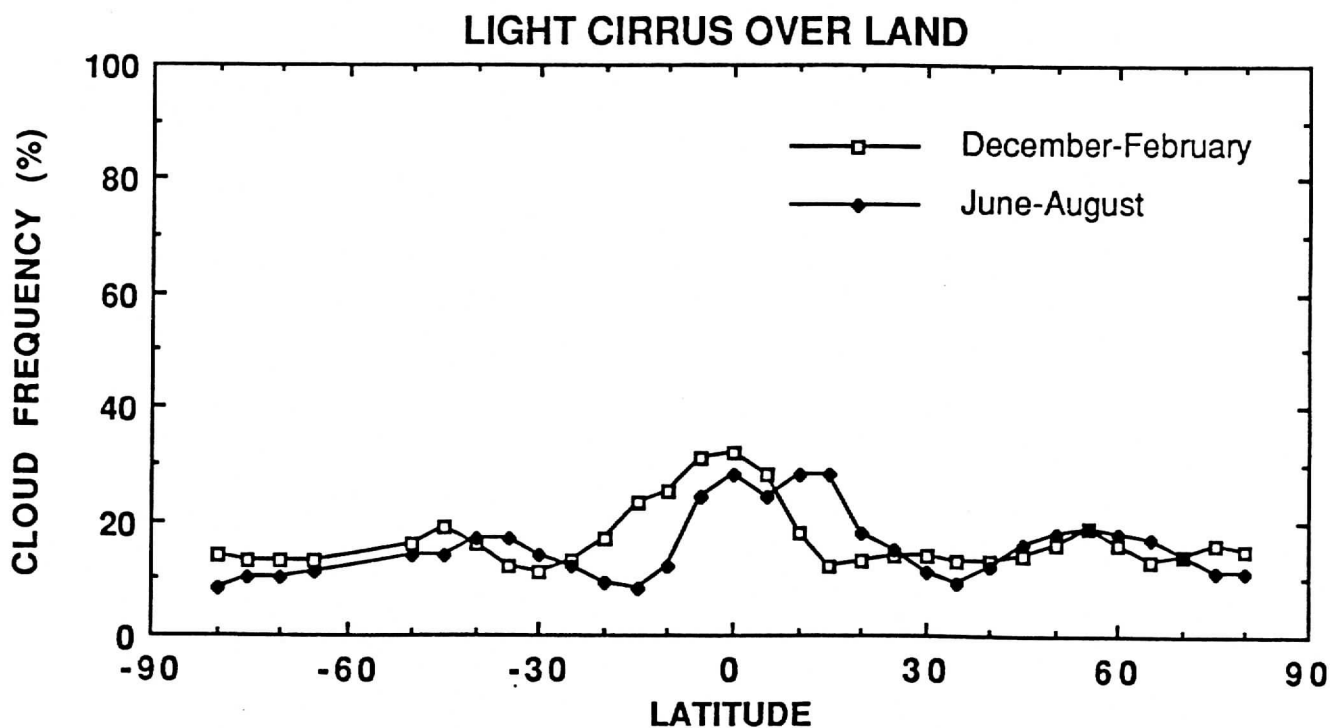
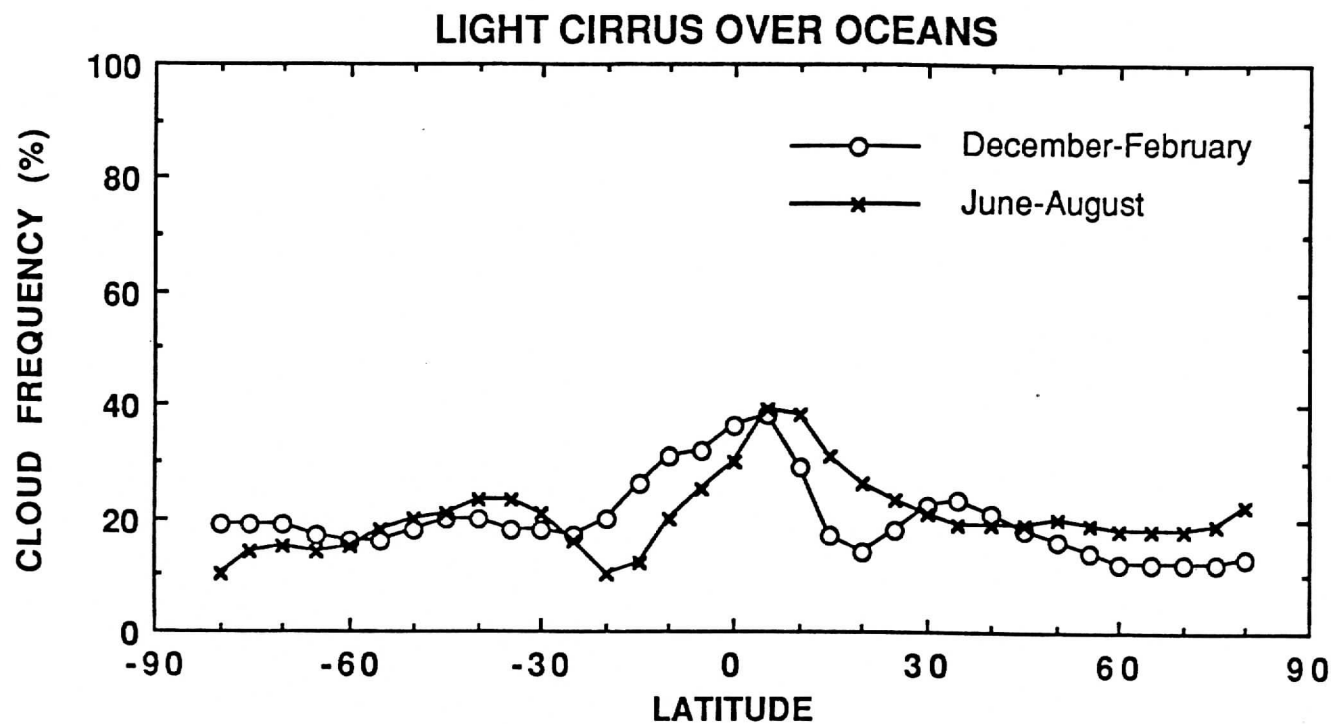
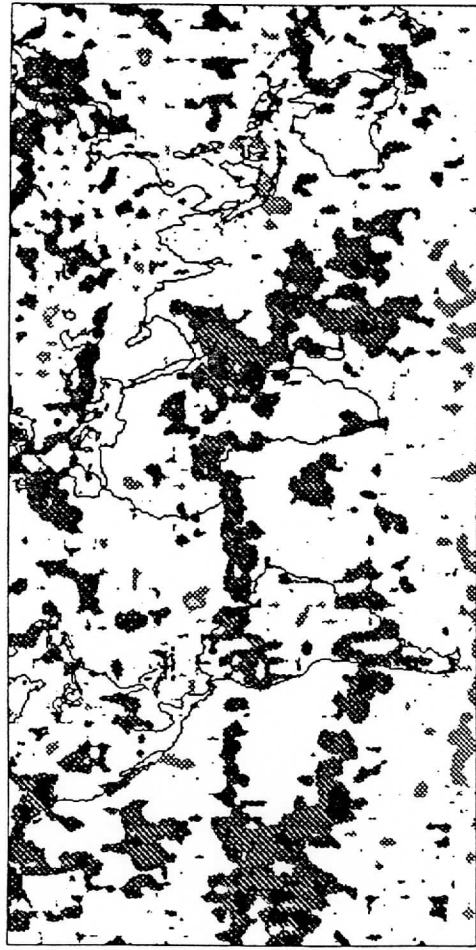


Figure 3: The frequency of thin transmissive clouds ( $N\epsilon < 0.5$ ,  $\tau < 0.7$ ) over ocean is shown in the upper panel as a function of latitude as a fraction of all satellite observations, clear and cloudy combined. Land is shown in the lower panel.

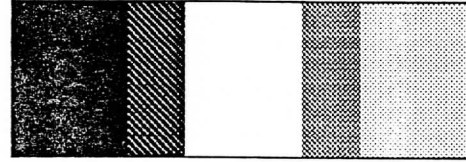
June through August 1990-1989 difference



June through August, 1991-1990 difference



June through August, 1992-1991 difference



> 25% increase

12.5% increase to 25% increase

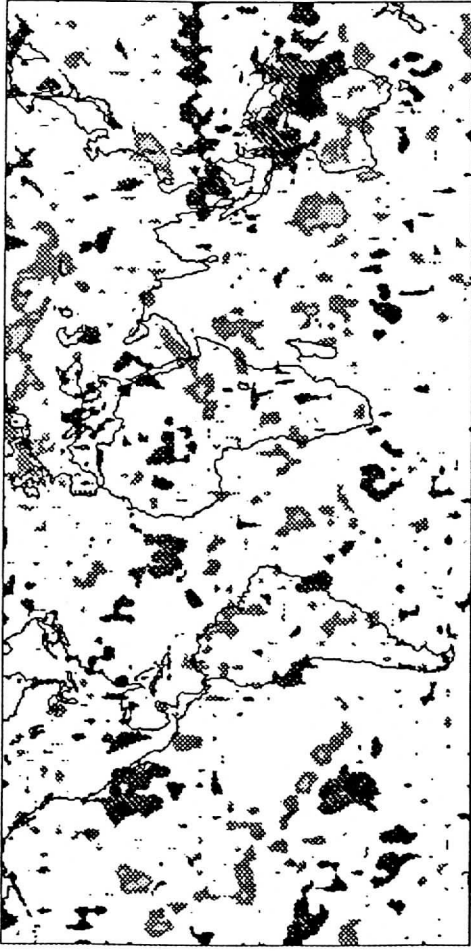
12.5% increase to 12.5% decrease

12.5% to 25% decrease

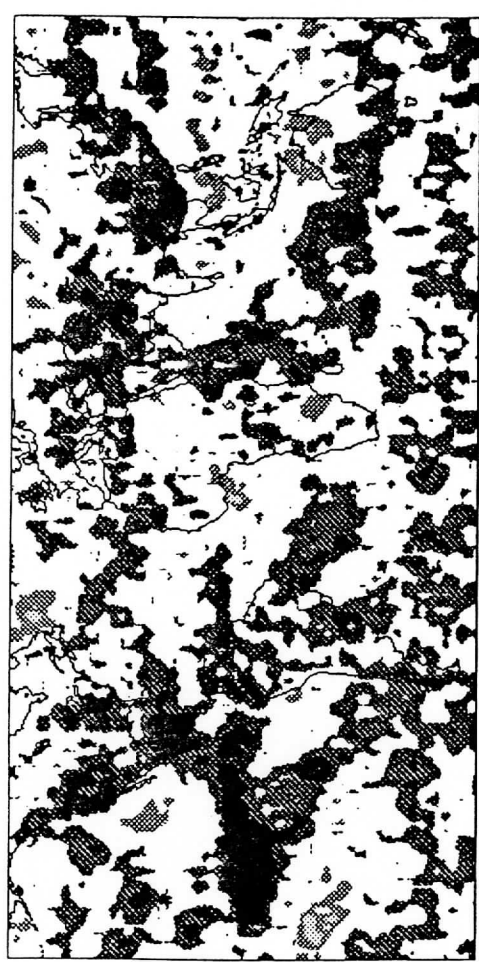
> 25% decrease

Figure 4: (a) The geographical distribution of the difference in the probability of cirrus in the four boreal summers, 1990 minus 1989 upper left panel, 1991 minus 1990 upper right and 1992 minus 1991 in the lower left. The boreal summer includes the months of June, July, and August.

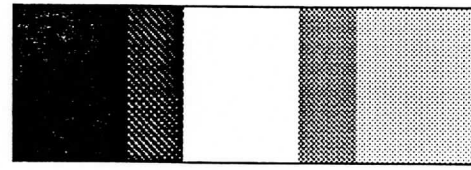
Dec. through Feb., ('90-'91)-('89-'90) difference



Dec. through Feb., ('91-'92)-('90-'91) difference



Dec. through Feb., ('92-'93)-('91-'92) difference



> 25% increase  
 12.5% increase to 25% increase  
 12.5% increase to 12.5% decrease  
 12.5% to 25% decrease  
 > 25% decrease

Figure 4: (b) The geographical distribution of the difference in the probability of cirrus occurring in the four boreal winters. Winter 1990-91 minus winter 1989-90 is the upper left panel, winter 1991-92 minus 1990-91 is the upper right panel and winter 1992-93 minus 1991-92 is the lower left panel. Boreal winter includes the months of December, January and February.

High Clouds      Light Ci      High Clouds      Light Ci  
 65°S - 65°N      20°S - 20°N      20°S - 20°N      E. Pacific

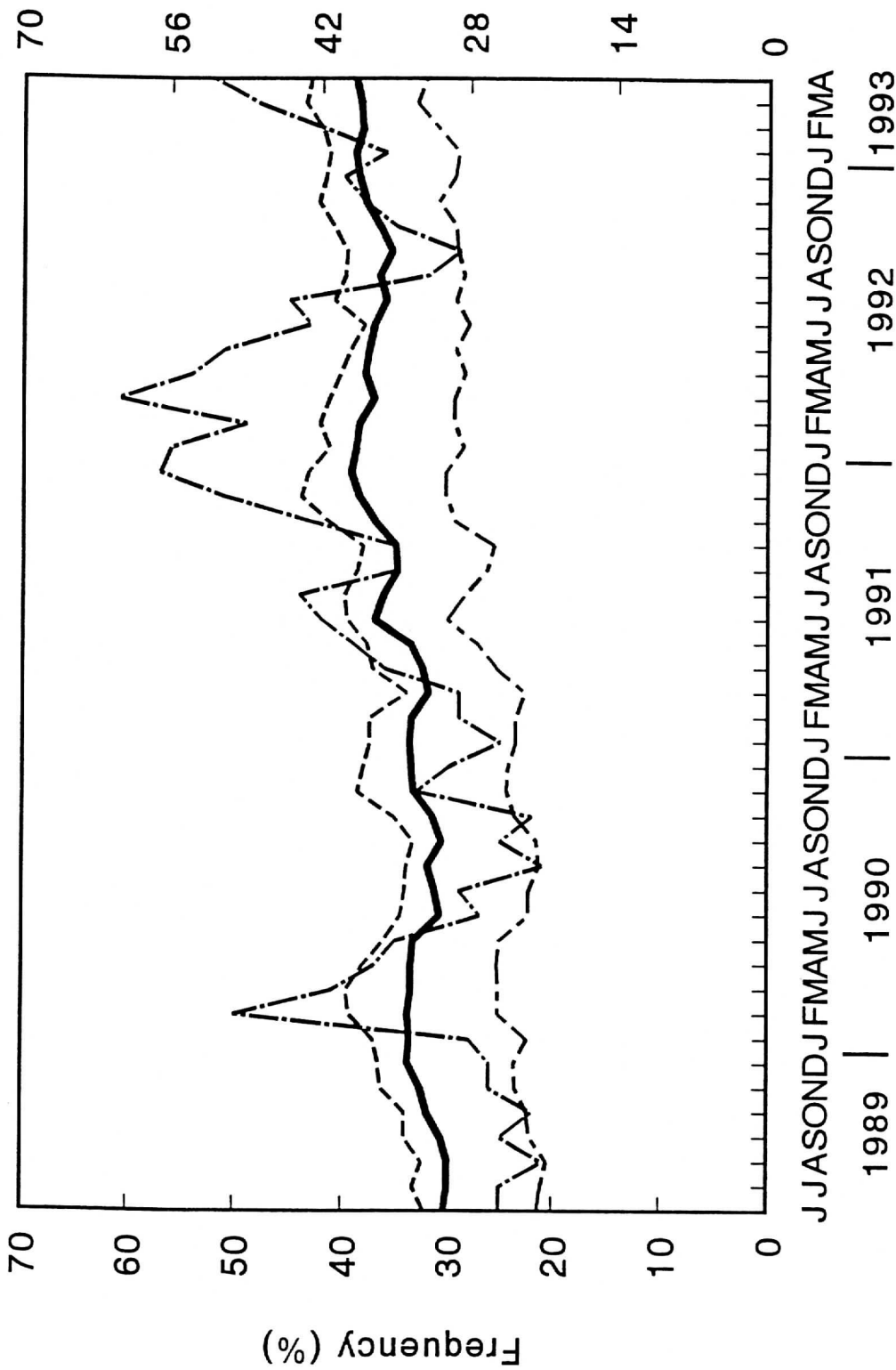


Figure 5: Monthly time series of high cloud (over 500 hPa) observations from 65 S to 65 N latitude (solid line), light cirrus with  $N_e < 0.5$ ,  $\tau < 0.7$  in the tropics from 20 S to 20 N (triple dash), all high clouds (over 500 hPa) in the tropics, 20 S to 20 N (dash), and light cirrus ( $N_e < 0.5$ ,  $\tau < 0.7$ ) in the eastern Pacific Ocean from 10 S to 10 N, 110 W to 170 W (dash dot).



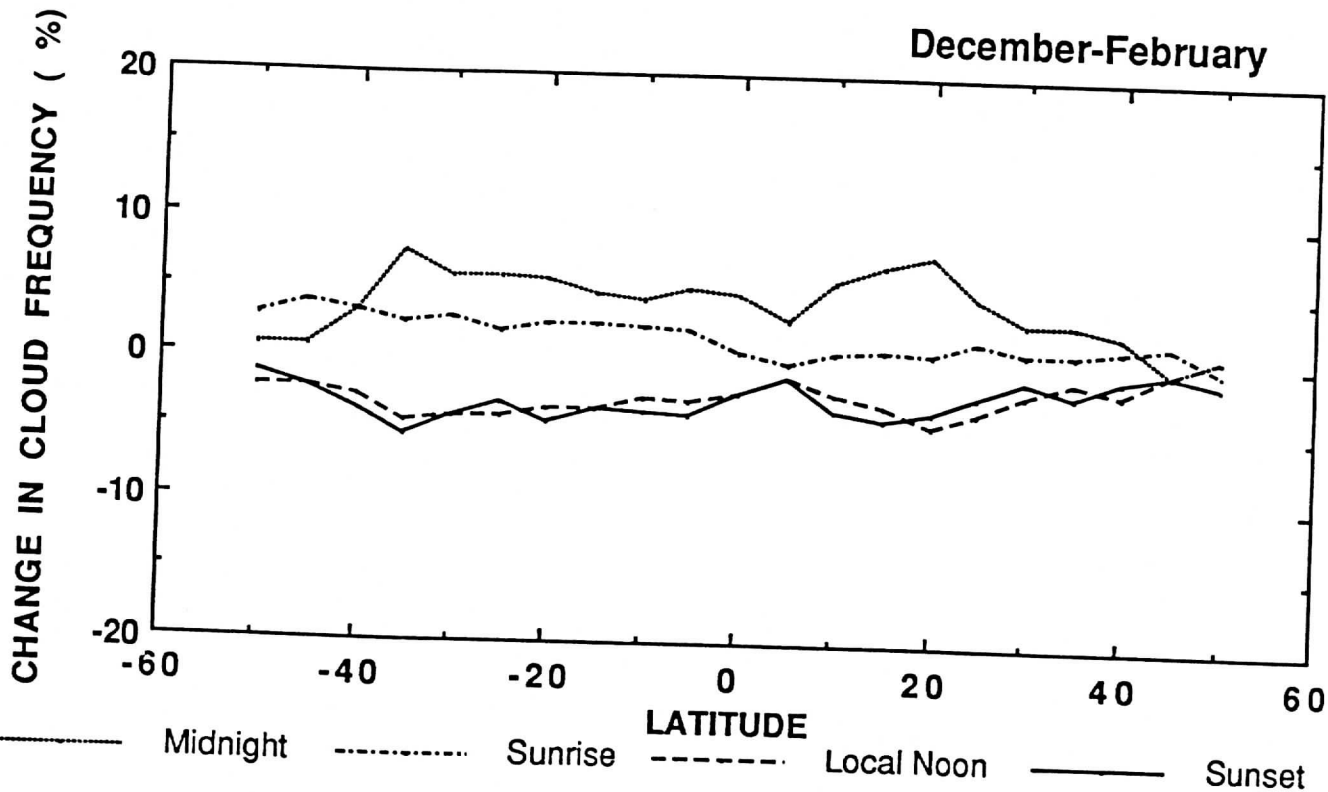
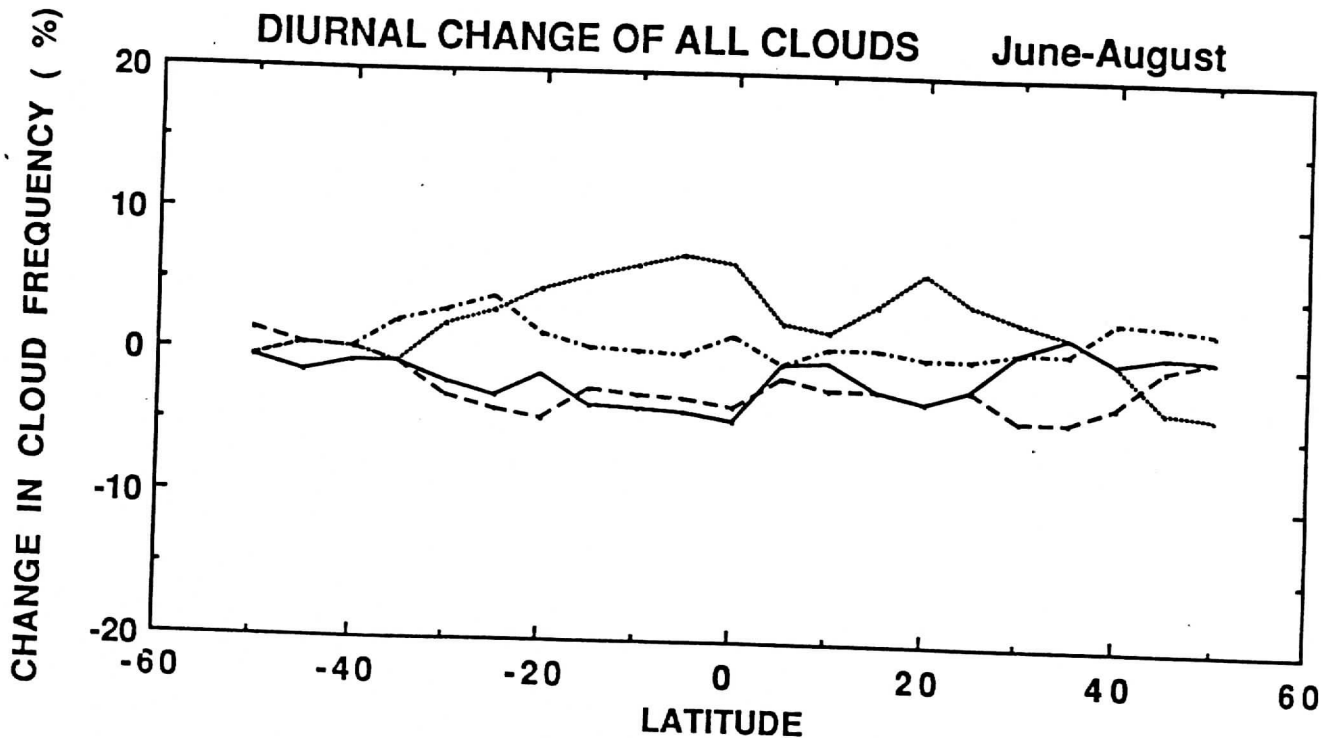


Figure 6: The diurnal change from the seasonal mean of all cloud observations expressed as a change in percentage points of the total clear and cloudy observations. Midnight represents the NOAA 11 evening pass which actually occurred between 0100 and 0300 a.m. local time. Sunrise is the morning NOAA 10 or 12 pass nominally from 0700 to 0800 a.m. local time. Local Noon is the afternoon NOAA 11 pass from 0100 to 0300 p.m. Sunset is the evening NOAA 10 or 12 pass from 0700 to 0800 p.m.

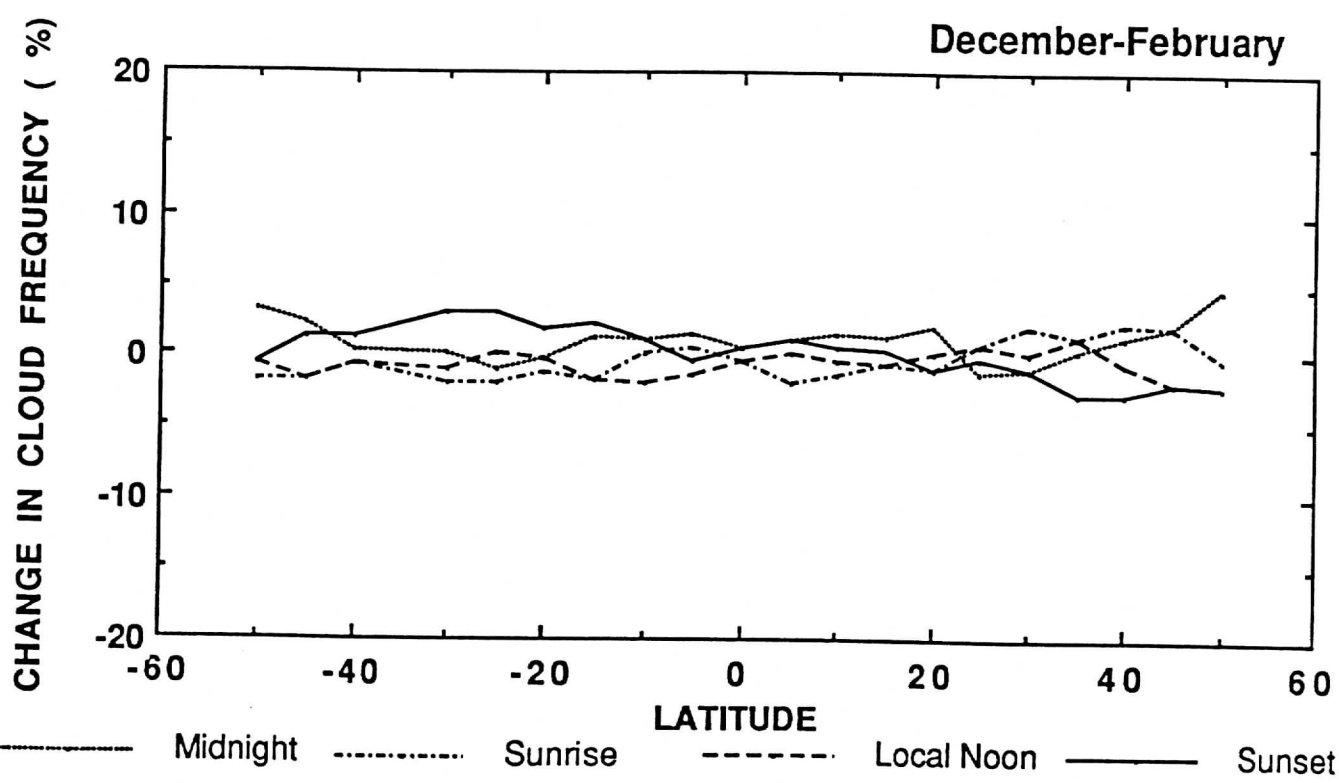
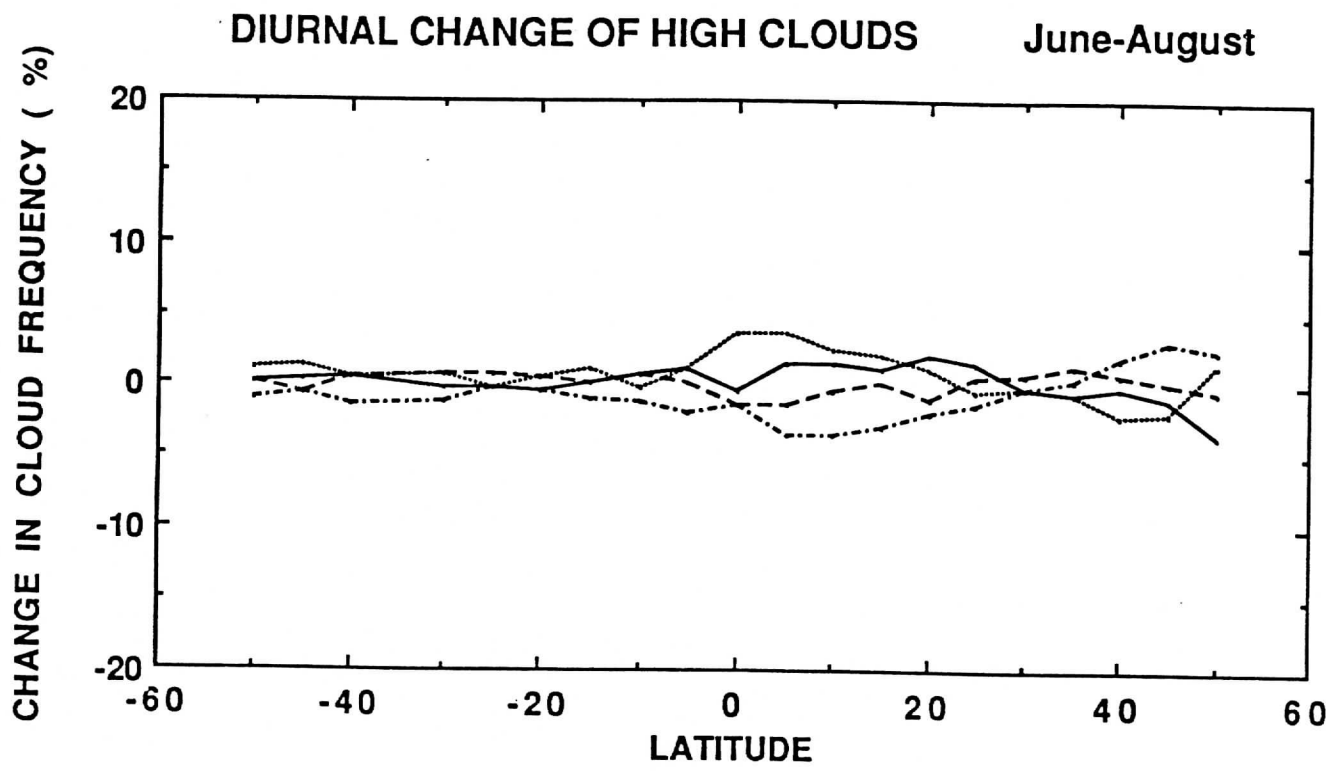


Figure 7: Same as Figure 6 for the change in the frequency of high cloud observations (pressure less than 500 hPa).

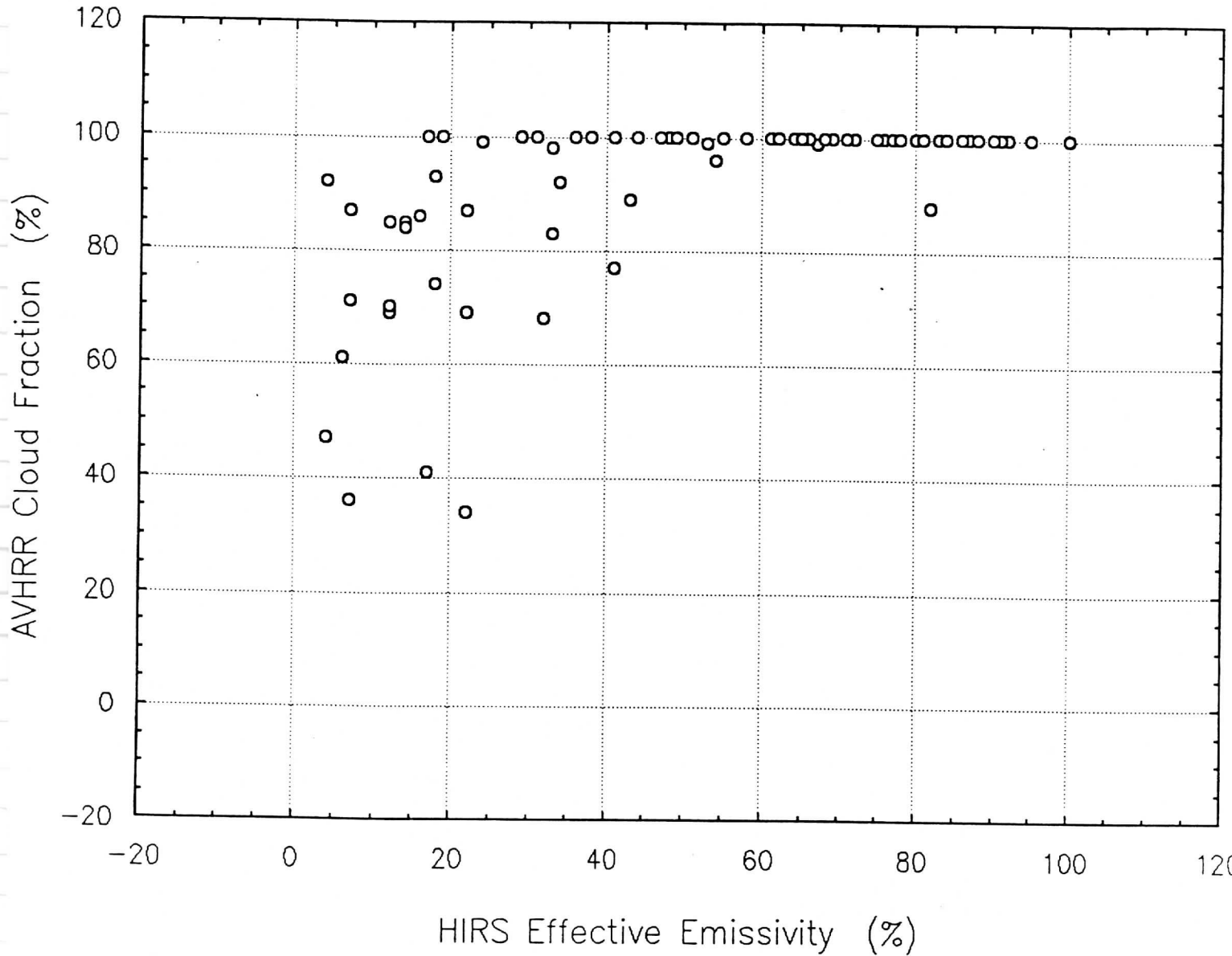


Figure 8: Plot of AVHRR cloud fraction  $N_A$  (determined from infrared brightness temperature comparison to surface temperature within a collocated HIRS FOV) versus the HIRS  $\text{CO}_2$  slicing effective emissivity  $N\epsilon_H$  for 6 and 12 January 1994 over the Atlantic Ocean.

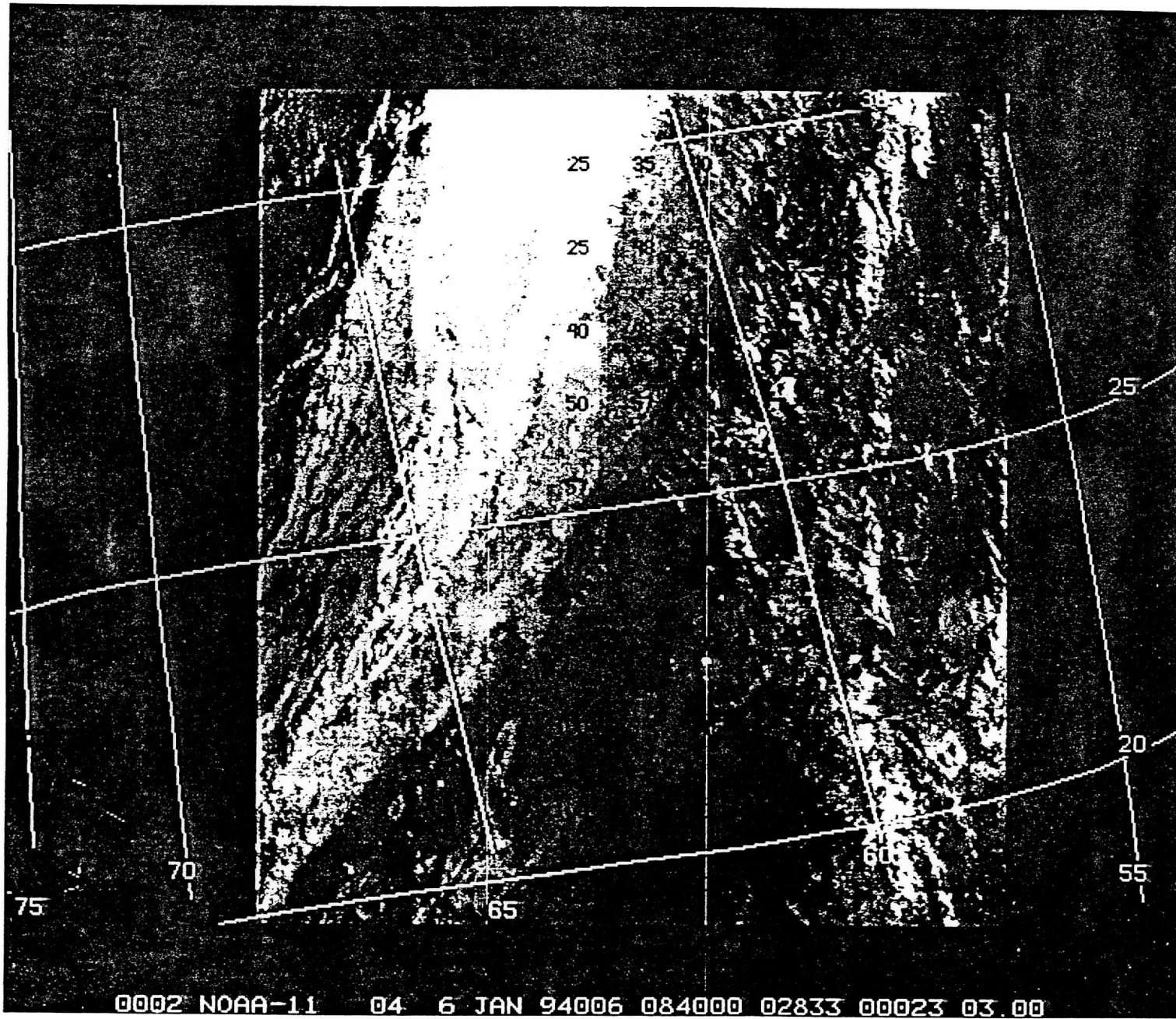


Figure 9: AVHRR infrared window image from 6 January 1994 over the Atlantic Ocean from which the cloud fraction versus effective emissivity study was made. HIRS CO<sub>2</sub> cloud pressures are indicated in hPa divided by ten.

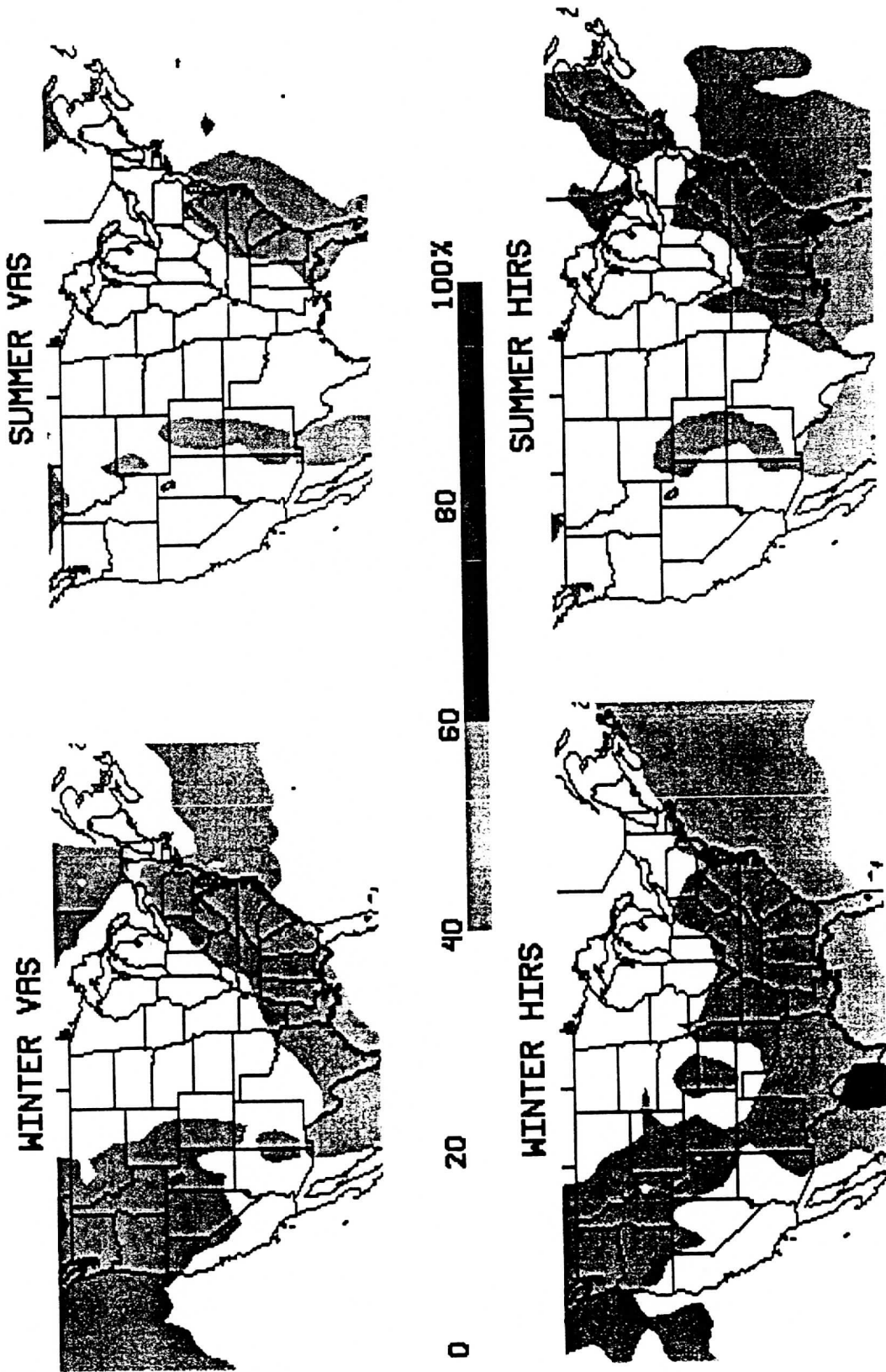


Figure 10: The frequency of high cloud observations (cirrus and opaque above 500 hPa) reported by VAS and HIRS during four years (June 1989 to May 1993) in the boreal winter months (December, January, and February) and in the boreal summer months (June, July, and August). Grey shades indicate changes of 20%.

Appendix C

UNDERSTANDING SATELLITE CIRRUS CLOUD CLIMATOLOGIES WITH  
CALIBRATED LIDAR OPTICAL DEPTHS

Donald Wylie and Paivi Piironen  
Space Science and Engineering Center  
University of Wisconsin-Madison  
Madison, WI 53706

Walter Wolf and Edwin Eloranta  
Department of Meteorology  
University of Wisconsin-Madison  
Madison, WI 53706

Submitted to  
The Journal of Atmospheric Sciences

July 1994

## Abstract

Optical depth measurements of transmissive cirrus clouds were made using coincident lidar and satellite data to improve our interpretation of recent satellite cloud climatologies. These climatologies differ in the way they detect transmissive clouds because some use solar reflectance data (ISCCP) while others use multi-spectral infrared data (CO2 Slicing). To relate these climatologies and estimate the impact of transmissive clouds on the earth's heat budget, a relationship between visible and infrared radiation properties has to be used. We examined the popular assumption that the ratio of the visible to infrared optical depths should be 2.0 because the visible extinction cross section is twice the infrared absorption cross section when cloud particles are large compared to the wavelength.

Our lidar-satellite data combination confirmed this relationship for optically thin cirrus ( $\tau_{\text{vis}} < 1$ ) that were uniform both vertically and horizontally. Deviations from the 2.0 ratio appeared to come from differences in sampling horizontally variant clouds. The lidar observed a small area ( $\approx 1$  m diameter) with the only spatial sampling being from wind advection of the cloud over the sensor while the satellite sensors sampled larger areas 1-20 km in diameter in both the along wind and cross wind directions.

Most cirrus were physically thick ( $> 1$  km) and often composed of multiple layers. Super cooled liquid water layers embedded in ice clouds were found in 32% of the cirrus examined.

For thick cirrus and multi-layered cirrus, a direct optical depth comparison was not possible because of the single layer model used in the satellite analysis. However, we simulated what the satellite infrared analysis (CO2 Slicing) would produce in complicated cirrus structures of multiple levels including a super cooled liquid water layer. The simulation used the detailed measurements of vertical extinction from the lidar for deriving the radiances that the satellite would receive on each of its infrared channels. A single cloud height solution was calculated following the CO2 Slicing method. An infrared optical depth was also calculated for this single cloud level using the satellite measured radiances in the 10.8  $\mu\text{m}$  window channel. The calculated cloud level was close to the altitude of the densest cloud layer found by the lidar. The infrared

## 1. INTRODUCTION

Predictions of global warming from the increase of CO<sub>2</sub> in the atmosphere have lacked credibility because of the need to assess the contribution of clouds to the radiation budget (Paltridge, 1980). Cirrus clouds, in particular, have the ability to either offset the CO<sub>2</sub> warming by increased solar reflection or increase the warming by the capture of terrestrial radiation. Thin cirrus in the upper troposphere will add to tropospheric warming because it allows solar insolation while capturing part of the terrestrial radiation. Thick cirrus and multiple layer cloud conditions where water clouds are present under the cirrus produce highly reflective cloud combinations that can lower albedo and solar insolation. Predictions of climate changes ultimately must include the radiative effects of these clouds. However, Stephens et al. (1990) point out that the effect of clouds on the earth's radiation budget is not understood because of the lack of data.

Global cloud and radiation data sets are presently being collected from satellites. The International Satellite Cloud Climatology Project (ISCCP, Schiffer and Rossow, 1983, and Rossow and Schiffer, 1991) has measured cloud cover and radiation for 11 years using the operational weather satellites. Wylie et al. (1994) have studied cirrus clouds from four years of polar orbiting NOAA satellite data, also Woodbury and McCormick (1983) have made a similar analysis of global cirrus from the SAGE II satellite data.

Inter-annual changes in cloud cover have been found. The Wylie et al. (1994) study reported an increase in cirrus with the recent El Nino-Southern Oscillation (ENSO) that began in 1991. A similar change in cloud cover in the 1982-83 ENSO was also found by Weare (1992) using the NIMBUS 7 data set. These studies indicate that cloud cover is linked to climatic fluctuations.

Estimates have been made of the effect of lower tropospheric clouds on the earth's heat budget by Tselioudis et al. (1993) using ISCCP data, but similar calculations for upper tropospheric clouds have not been attempted because of the complications of estimating the effects of both the visible and the infrared radiative processes together. Boundary layer and lower tropospheric clouds affect solar insolation but have little effect on infrared cooling, while cirrus



clouds affect both radiative processes. Satellite observations have usually been restricted to either the visible or the infrared. The satellite data used by Wylie et al. (1994) and Weare (1992) were from longwave infrared sensors, therefore the effect on solar radiation will have to be estimated since it was not measured. The ISCCP differs from these two studies in that it employs visible sensors for detecting transmissive cirrus clouds. The IR contribution must be estimated from the visible reflectance measurements. The 11 year record of the ISCCP (Schiffer and Rossow, 1983) will allow studies of fluctuations of cloud cover with many short term climate changes including three ENSO's. The SAGE II data set can also be used for deriving visible optical depths (Laio, et al. 1994a and b). These satellite data sets are complimentary where they overlap, but the overlap is small, about one year for each intersection. To study interannual changes, trends, and longer term fluctuations, each of these data sets will have to be used separately. Visible to infrared radiance relationships will have to be used to fully estimate the effect of cirrus changes on heat budget parameters.

Our knowledge about the relationship of the solar reflection to the infrared attenuation in cirrus clouds is limited. For particles which are large compared to the wavelength, we expect the visible scattering cross section to be twice the infrared absorption cross section when there is little visible absorption and strong infrared absorption by ice and liquid water. This implies that the ratio of the visible to the infrared optical depth should be about 2.0. Modelling of the radiative properties of ice crystals by Minnis et al. (1993) and Mitchell and Arnott (1994) support this assumption. However, variances in cloud particle size and shape could vary this ratio from 1.8 to 4.0.

In situ measurements of cirrus microphysical properties have found extremely large variances in number density, ice-water content and particle size (Dowling and Radke, 1990). The number density of cloud particles varies by 8 orders of magnitude, from  $10^{-4} \text{ L}^{-1}$  to  $10^{+4} \text{ L}^{-1}$ . The ice-water content varies over  $10 \text{ g m}^{-3}$  and the particle size can vary from 1 to  $8000 \mu\text{m}$ . With this wide range of possible microphysical variances, large variances in the radiative properties are expected.

Few measurements of cirrus have been made when data from both the visible and IR were collected simultaneously. Platt (1979) used a vertically pointing IR radiometer with a visible lidar to study a limited number of thin cirrus cases. Minnis et al. (1990) studied one case from FIRE-I (the First ISCCP Regional Experiment in October 1986) using infrared data from a satellite and visible data from a lidar. Platt (1979) found a visible to IR optical depth ratio of 2.0 while Minnis' case was slightly higher at 2.1. These cases were mostly thin single layer cirrus.

To use the global cloud climatologies, we need to understand what has been measured and how their representation of clouds depicts the radiative transfer in both the visible and the infrared. The retrieval of cloud parameters in the satellite climatologies has been based on the assumption that the clouds are a single thin layer and that they cover the Field of View (FOV) of the satellite sensor for each pixel in the image. ISCCP and Wylie et al. (1994) only solved for one cloud level in each pixel (FOV). A comparison of satellite cloud retrievals to ground based National Weather Service observations over the continental United States found that low and middle tropospheric clouds were present in 52% of the cases where the satellite cloud detection system found an upper tropospheric cloud (Menzel et al., 1992). Similar statistics on the frequency of multiple cloud layers over oceans are shown in Hahn et al. (1982). Lidar data collected at the University of Wisconsin-Madison (Figure 1) found that cirrus are often geometrically thick reaching depths up to 5 km. Thus, we expect that cirrus are more complicated than the assumed thin single layer model used in the cloud retrieval algorithms.

Because of the uncertainty of what satellite cloud retrievals represent and the need to relate the different climatologies so that longer cloud records can be compiled, we collected a data set of high quality lidar observations with coincident satellite data. The purpose of this study is twofold: 1) to assess the applicability of the "single thin layer" assumption used in satellite cloud retrievals, and 2) to assess the validity of the 2.0 visible to infrared optical depth ratio so the satellite cloud climatologies can be combined for a more complete assessment of radiative transfer processes.

## 2. MEASUREMENT TECHNIQUE

This study was initiated in 1989 using the unique measurement systems at the University of Wisconsin-Madison (Ackerman, et al., 1993). Visible optical depths of cirrus were obtained from the High Spectral Resolution Lidar (HSRL) while infrared optical depths were obtained from satellite data so that the information collected could be related to the cirrus climatologies of Wylie et al. (1994) and ISCCP.

### 2.a. The HSRL

In order to make reliable measurements of the extinction profile, the HSRL measures two signals from the 0.53  $\mu\text{m}$  transmitted pulse which can be processed to yield separate lidar returns for aerosol and molecular scattering. This separation is possible because the spectrum of the molecular lidar return is Doppler broadened by the thermal motion of the molecules while the slow moving aerosol particles generate negligible spectral broadening. The molecular scattering cross section is a function of molecular density and can be calculated from Rayleigh scattering theory and an independently measured temperature profile. The HSRL then uses molecular scattering as a calibration target which is available at each point in the lidar return.

Two lidar returns are derived; these are given by the following equations for the signal power received from molecular scattering,  $P_m(r)$ , and aerosol scattering,  $P_a(r)$ :

$$P_m(r) = E_o \frac{cA_r}{2r^2} \beta_m(r) \frac{3}{8\pi} \exp(-2\tau(r)) \quad (1)$$

$$P_a(r) = E_o \frac{cA_r}{2r^2} \beta_a(r) \frac{P(\pi,r)}{4\pi} \exp(-2\tau(r)) \quad (2)$$

$E_o$  = Laser pulse energy, J.

$c$  = Speed of light,  $\text{ms}^{-1}$ .

$A_r$  = Collecting area of the receiver,  $\text{m}^2$ .

$r$  = Range to the scattering volume, m.

$\beta_a$  = Aerosol scattering cross section per unit volume,  $\text{m}^{-1}$ .

$\beta_m$  = Scattering cross section per unit volume for air molecules,  $\text{m}^{-1}$ .

$\frac{P(\pi,r)}{4\pi}$  = Backscatter phase function,  $\text{sr}^{-1}$ .

$\tau$  = Optical depth.

Equation 1 contains two unknowns: the optical depth between the lidar and the scattering volume,  $\tau(r)$ , and the molecular scattering cross section,  $\beta_m(r)$ . Molecular scattering is described by the Rayleigh scattering equation and is directly proportional to atmospheric density,  $\rho(r)$ .

$$\beta_m(r) = C\rho(r)$$

Thus if we define a range-squared, energy corrected molecular lidar return:

$$S_m(r) = P_m(r)r^2/E_0$$

$$\ln[S_m(r)] = \text{constant} + \ln[\rho(r)] - 2\tau(r)$$

The optical depth between any two ranges,  $r$  and  $r_0$ , is given by:

$$\tau(r) - \tau(r_0) = 0.5 \ln[\rho(r)/\rho(r_0)] - 0.5 \ln[S_m(r)/S_m(r_0)] \quad (3)$$

The average extinction cross section in a layer between  $r_0$  and  $r$  can be computed from equation 3:

$$\overline{\beta_e(r,r_0)} = [\tau(r) - \tau(r_0)]/[r-r_0] \quad (4)$$

More details can be found in Grund and Eloranta (1991) and Piironen and Eloranta (1994).

## 2.b. Satellite Infrared

The satellite cloud analysis of Wylie et al. (1994) assumes that the radiative effects of the clouds occur at only one level in the troposphere. This allows a simple calculation of cloud emittance at  $10.8 \mu\text{m}$ , the longwave window channel, from the radiances measured by the satellite in the cloudy pixel ( $R_{\text{sat}}$ ), a clear pixel ( $R_{\text{clr}}$ ), and the radiance expected if an opaque cloud were present at the pixel ( $R_{\text{cld}}$ ).

$$\epsilon_{\text{ir}} = [R_{\text{clr}} - R_{\text{sat}}] / [R_{\text{clr}} - R_{\text{cld}}] \quad (5)$$

$R_{\text{sat}}$  was measured from the pixel that covered the HSRL while  $R_{\text{clr}}$  is an estimate of the radiance that would have been measured if the cloud was not present. This clear radiance estimate was derived from the nearest clear pixel by assuming that the background under the cloud was the same as at the location where  $R_{\text{clr}}$  was taken.  $R_{\text{cld}}$  was calculated from the temperature of the mid-cloud level using rawinsonde data from Green Bay, WI which was the nearest sounding to the

HSRL. To simplify the calculation, the black body temperature to the fourth power ( $T^4$ ) was used in place of R. The satellite measurements are calibrated to both radiance (R) and blackbody temperature (T). Equation 5 was expressed as:

$$\epsilon_{ir} = [T_{clr}^4 - T_{sat}^4] / [T_{clr}^4 - T_{cld}^4] \quad (6)$$

where:

- $T_{clr}$  = blackbody brightness temperature for a clear pixel
- $T_{sat}$  = blackbody brightness temperature for a cloudy pixel
- $T_{cld}$  = the air temperature at the mid-cloud height.

The mid-cloud altitude was determined from the appearance of the cloud on the HSRL backscatter vertical profile. This approximated the cloud level that the HIRS analysis reports for transmissive clouds (Wylie and Menzel, 1989).

IR optical depths were calculated from the emittances assuming no scattering at the window channel IR wavelength (10.8  $\mu\text{m}$ ) and that transmission was the compliment of emission:

$$\tau_{ir} = -\ln(1 - \epsilon_{ir}) \quad (7)$$

The infrared optical depths were also corrected for the angle of the satellite scan through the atmosphere using the cosine of the zenith angle.

### 3. DATA

HSRL data were examined for 21 separate days covering all four seasons (see Table 1). NOAA 12 overpasses of Madison, WI were available when most of the HSRL data were taken. However, on six days, GOES 7 data were compared to the HSRL because of the absence of NOAA 12 data. Comparisons were restricted to cases with visible optical depths < 3 when the HSRL probed through the entire cloud. Total cloud penetration was determined by the presence of molecular backscatter signal beyond the cloud top (Equation 1).

## 4. RESULTS

### 4.a. Visible and IR Optical Depths

To compare visible and infrared radiative properties, satellite infrared optical depths from Equation 7 were plotted with the HSRL visible optical depths from Equation 3 (see Figure 2). The 21 cases covered a variety of transmissive cirrus situations. The clouds were separated into three classes: 1) geometrically thin, covering  $< 2.5$  km, 2) geometrically thick, covering  $> 2.5$  km, and 3) multi-layered clouds. Many of the multiple level cloud cases included a thin layer of super cooled liquid water (distinguished by low values of depolarization measured by the HSRL) and often included ice crystals precipitating from the layer. Liquid water layers embedded in cirrus were found on 32% of the days that the HSRL collected cirrus data.

Error estimates for both the HSRL and satellite optical depth measurements are also included in Figure 2. For the visible optical depth (horizontal bars) the error was computed from an error analysis including photon counting statistics, error in the observed density profile, and error in system calibration. For the satellite infrared optical depths (vertical bars), the error was estimated by assuming a 2 K error in each variable in Equation 6. This is our estimate of the maximum uncertainty in determining the clear radiance ( $T_{\text{clr}}^4$ ) and the cloud level radiance ( $T_{\text{cld}}^4$ ). The largest source of clear radiance error was spatial variances or gradients in the land surface or low level aerosol density between the locations of the HSRL and where  $T_{\text{clr}}$  was obtained. The largest source of  $T_{\text{cld}}$  error was the air temperature gradient between the location of the HSRL and the rawinsonding. The satellite radiometric measurements are calibrated to 0.8 K which is a far better accuracy than the other error sources. The location of the HSRL in the satellite images was also determined to an accuracy of  $< 1$  pixel using navigation adjustments from rivers and lake shorelines.

#### **4.b. Single Layer Cirrus**

An example of a single layer cirrus cloud is shown in Figure 3 from 26 October 1993. The cirrus cloud was found between 9 and 11 km and was fairly uniform in the vertical dimension and in time as seen in the lidar time section. The NOAA satellite image (Figure 4) also showed very uniform conditions around the HSRL (black dot on the image). Brightness variations around the

HSRL were highly enhanced but span a range of only 1.5 K in blackbody temperature. The cirrus over the HSRL was part of a large air mass moving from the southwest to the northeast. The visible optical depth was 0.5 at the time of the NOAA overpass (0:30 UT). The satellite infrared optical depth was found to be 0.28, yielding a  $\tau_{\text{vis}}/\tau_{\text{ir}}$  ratio of 1.8, close to the expected 2.0.

Low level aerosols were also present from 0-3.2 km as indicated by the HSRL (Fig. 3). These aerosols were probably not included in the satellite optical depth measurement.  $T_{\text{cir}}$  in Equation 5 was taken from an area 150 km to the southeast in the satellite image where similar low level aerosols should have been present.

#### 4.c. The Effects of Multiple Cloud Layers

Multiple layers of clouds have been very common during this study. Five cases of multiple layers were examined in this study. One example is shown in Figure 5 for 11 November 1993 when the cirrus was changing during the HSRL observation. Initially, only one layer of cirrus from 7 to 10 km was present; then at 1:15 UT a second layer appeared. Depolarization measurements by the HSRL indicated that the intense backscatter levels (solid white) were liquid water particles while the rest of the cloud was ice. Visible optical depths increased from 0.4-0.6 to 1.0 at the NOAA overpass at 1:30 UT. After 1:40 UT the visible optical depth exceeded 3.0, the maximum measurable by the HSRL. The NOAA 12 IR image in Figure 6 also shows this change as dense clouds moved in from the west. Notice that the light cirrus to the east (down wind) has faint northwest-southeast striations while the denser area to the west (up wind) has orthogonal southwest-northeast striations. Both patterns are skewed to the westerly wind.

The water layer dominated the optical depth of the combined cirrus layers. The upper ice cloud maintained a nearly constant optical depth of 0.4-0.6 until 01:40 UT when the HSRL could no longer penetrate through the water layer.

The satellite measured blackbody radiance decreased from 261 K before the lower layer formed (to the east in the image), to 253 K at the HSRL location. In the dense two layer cloud it dropped to 243 K at 30 km west of the HSRL in the image.

Simulations of the HIRS radiance and cloud height measurements were made for three situations: 1) the single layer case, 2) the two layers at the NOAA 12 over pass at 1:30 UT, and 3) the point when the lower water layer first obscured the HSRL at 1:40 UT. The second and third situations represent problems to the basic assumption used in satellite cloud retrievals - the single level description of the cloud. The expected response of the multi-spectral HIRS cloud retrieval algorithm used by Wylie et al. (1994) to multi-layered clouds is that it would place the single cloud height between the two layers (Wielicki and Coakley, 1981 and Menzel et al., 1992). The single level cloud height is calculated from the mean altitude of infrared radiative divergence, similar to a center of mass concept in kinematics. However, when one cloud layer has more optical depth than the other, the multi-spectral HIRS cloud height solution is expected to move toward the denser layer. An exception to this trend occurs when the top layer is nearly opaque and obscures the view of the lower layer, forcing the HIRS solution into the top layer.

Attempts have been made to extract more than one cloud level from the multi-spectral HIRS data. However, the solution of the radiative transfer model for the HIRS sensors requires the integral of the radiation over a broad portion of the troposphere. The cloud height solution has been mis-labelled the CO2 Slicing Method from the desire that each channel would see a different "slice" of the atmosphere; however, altitude sensitivities of the channels are broad and overlap. Each HIRS channel receives radiation from 3-5 km of the troposphere. To solve for more than one cloud level, the vertical profile of the clouds must be determined. Since each HIRS sensor sees the integral of the radiation over a large depth of the troposphere, a wide variety of cloud structures could be present from which no unique solution can be made. The only tractable solution for the HIRS data is one cloud level.

The response of the multi-spectral HIRS algorithm to the cloud structures observed by the HSRL was simulated by calculating what the HIRS channels should have seen given the temperature structure and the infrared emittance and transmittance of each cloud layer. HIRS data were available for all cases where the NOAA satellites were used. The HIRS data were not used because the HIRS data were not directly over the HSRL. The HIRS pixels (FOV) do not



overlap and contain gaps between pixels that are about the same dimensions as the FOVs. For accurate comparisons to the HSRL, radiative data must come from the location of the HSRL. Spatial variance of the clouds can cause large errors. These errors are discussed in detail in section 4d.

The radiance received by each HIRS sensor was estimated using a simple model of three cloud layers.

$$\begin{aligned}
 I_i = & \int_{p_1}^0 B[i, T(p)] \{dS_i(p)/dp\} dp + S_i(p_1) \epsilon_1 B[i, T(p_1)] \\
 & + (1-\epsilon_1) \left[ \int_{p_2}^{p_1} B[i, T(p)] \{dS_i(p)/dp\} dp + S_i(p_2) \epsilon_2 B(i, T(p_2)) \right] \\
 & + (1-\epsilon_1)(1-\epsilon_2) \left[ \int_{p_3}^{p_2} B[i, T(p)] \{dS_i(p)/dp\} dp + S_i(p_3) \epsilon_3 B(i, T(p_3)) \right] \\
 & + (1-\epsilon_1)(1-\epsilon_2)(1-\epsilon_3) \left[ \int_{p_{sfc}}^{p_3} B[i, T(p)] \{dS_i(p)/dp\} dp + S_i(sfc) B(i, T(sfc)) \right]
 \end{aligned} \tag{8}$$

Where:

$B[i, T(p)]$  = the Planck function for spectral channel (i) and temperature  $T(p)$ ,  
 $S_i(p)$  = the transmittance of that radiation from level  $p$  through the atmosphere,  
 $\epsilon_x$  = the emittance for cloud layer  $x$ .

The emittance ( $\epsilon$ ) for each cloud layer was approximated from the HSRL measurements of the visible optical depth of the layer. The infrared optical depth was assumed to be one half of the visible optical depth for each cloud layer and the emittance ( $\epsilon$ ) was derived from Equation 7.

The approximated radiances for the HIRS channels were used in the algorithm described by Wylie et al. (1994) for determining a single cloud level. This cloud level was then used for determining  $T_{cld}$  from the rawinsonde data. With a new  $T_{cld}$  and the measured  $T_{sat}$  and  $T_{clr}$  Equations 6 and 7 were re-applied to give an estimate of what the HIRS algorithm would have derived for the cloud altitude and infrared optical depth ( $\tau_{ir}$ ). Note that this calculation used a combination of satellite measured radiances,  $T_{sat}$  and  $T_{clr}$  and a new radiance for the approximate single cloud level,  $T_{cld}$ .

The first situation on 11 November, was a single cirrus layer with a mean height of 8.5 km. The infrared optical depth calculated from Equations 5 and 6 was 0.25. With the HSRL visible optical depth measurement of 0.5, the  $\tau_{\text{vis}}/\tau_{\text{ir}}$  ratio of 2.0 agreed with theory.

The HIRS radiances for the second situation at 1:30 UT were calculated from Equation 8 using two cloud levels at 5 and 8.5 km. The visible optical depths of the two layers measured by the HSRL were 0.9 (lower) and 0.6 (upper). Emittances of 0.4 for the lower layer and 0.3 for the upper layer were calculated from Equation 7 by assuming that the infrared optical depths were one half of the visible HSRL measurements. The single cloud layer calculated from the Wylie et al. (1994) algorithm was 6.6 km which was between the two cloud layers. The infrared optical depth from this level and the AVHRR  $T_{\text{sat}}$  and  $T_{\text{clr}}$  measurements was 0.6. Using the HSRL measured visible optical depth of 1.0,  $\tau_{\text{vis}}/\tau_{\text{ir}}$  was 1.7, slightly lower than theory.

In the third situation at 1:40 UT the total optical depth exceeded the HSRL measurement capability. However, Equation 8 was employed to estimate HIRS radiances by assuming that the upper cloud layer remained at the same optical depth as measured at 1:30 UT and the lower cloud layer was at the level of HSRL saturation, 3.0 visible or 1.5 infrared. The single cloud level solution was 5.9 km, 0.7 km closer to the liquid water layer than the calculation from the second situation.

This is an example of how the HIRS single cloud level solution used by Wylie et al. (1994) responds to multiple level clouds. The technique is constrained to reporting only one cloud layer. For one layer of transmissive cirrus, it places the cloud level near the center of the layer as predicted by Wielicki and Coakley (1981). Similar results for a previous comparison with lidar data were reported in Wylie and Menzel (1989). For two layers, the HIRS solution was between the layers, moving toward the denser lower layer as it became the dominant layer.

We acknowledge that the estimation of HIRS infrared radiances and the calculation of infrared optical depths for the two layered cloud appears to be a circumlocution because HSRL visible optical depth measurements were used. However, the infrared optical depth calculation (Equations 6 and 7) involves more than the cloud height and the radiance ( $T_{\text{cd}}^4$ ) from this cloud

height level using the temperature sounding. The other terms in Equation 6,  $T_{\text{sat}}$  and  $T_{\text{clr}}$  came from satellite measurements independently of the HSRL measurements. Also, Equation 8 uses radiances from the sounding (the integrals) as well as the emittances of the cloud layers that came from the HSRL optical depths. To test the sensitivity of Equation 8 to the method of transforming HSRL visible optical depth measurements to infrared emittances, the calculations were repeated using  $\tau_{\text{vis}}/\tau_{\text{ir}}$  ratios of 1.0 and 4.0 on the HSRL visible optical depth measurements. These two tests differed from the original relationship by a factor of 2. These tests changed the single cloud level solution by  $\pm 0.6$  km and the derived infrared optical depth by  $\pm 0.1$ . This is smaller than the changes caused by the increase in density of the lower cloud layer.

#### 4.d. The Effects of Vertical and Horizontal Variability

Most of the deviations from the 2.0 visible to IR optical depth ratio in Figure 2 came from cirrus clouds with high horizontal variations. An example of such a cloud observed with the HSRL on 2 September, 93 is shown in Figure 7. The NOAA 12 satellite image from the 01:36 UT overpass (Figure 8) shows a small and long cirrus cloud which is partially over the HSRL (dot in the image). This cloud moved east on a  $75^\circ$  bearing. Only part of it crossed the HSRL. Larger clouds up wind crossed the HSRL at 01:55 UT. This is an example of how spatial variability affected the lidar-satellite comparison. The visible optical depth at the time of the satellite overpass was 0.2 while the infrared optical depth at the presumed HSRL location was 0.05 yielding a  $\tau_{\text{vis}}/\tau_{\text{ir}}$  ratio of 4.0, larger than predicted from theory. The satellite radiance was taken in a gradient region where any error in location could raise or lower its value. Also, for horizontally small and narrow clouds, the larger size of the satellite radiometer's FOV may have averaged more cloud area with less cloud optical depth than that viewed by the HSRL.

Most of the low optical depth cases shown in Figure 2 came from GOES satellite data which has a larger FOV than the AVHRR (10.8 km diameter GOES vs. the 1 km AVHRR). The GOES tended to find higher optical depths than predicted by the lidar, the opposite of the 2 September case previously discussed. Substantial horizontal variances were present in all of the

cases with visible optical depth  $< 0.2$ . We suspect that the satellite pixels used to determine clear radiances ( $T_{\text{clr}}^4$ ) may have had cloud contamination and thus  $T_{\text{clr}}^4$  may have been too cold which would cause higher infrared optical depths to be calculated.

Another example of a variable cloud situation was found on 15 April, 94, see Figures 9 and 10. The HSRL image of backscatter cross section (Figure 9) showed large variations in the optical depth with time while the NOAA 12 AVHRR image (Figure 10) showed cirrus clouds with a variety of shapes. An elongated cloud partially covered the HSRL at the time of the satellite overpass (00:49 UT) and moved toward the northeast on a  $80^\circ$  bearing. There were at least two layers of cirrus as indicated in Figure 9. The lower layer was more dense but highly variable in nature and contained some super cooled water. The upper layer was very thin and composed entirely of ice. The visible optical depth was 0.75 while the infrared was 1.07. This combination produced a  $\tau_{\text{vis}}/\tau_{\text{ir}}$  optical depth ratio of 0.7, far less than the theoretical 2.0.

To statistically estimate the errors of FOV size differences and possible miss-registration of the satellite image, data from the Volume Imaging Lidar (VIL) were examined. This is a 1064 nm Nd:YAG lidar with an optics system that scans from horizon to horizon. It was operated on 1 December, 1989 for two hours when transmissive cirrus were present. The VIL performed a pair of scans in 2 minute cycles. The cycle consisted of a cross wind scan (north to south) followed by an along the wind scan (east to west). Examples of images made from these scans are shown in Figures 11 and 12. The cross wind scans are the upper panel and the along wind scans are the lower panel.

The two hour period from 19:30 to 21:30 UT (13:30 to 15:30 CST) began with light broken cirrus to the north and one line of precipitating cirrus to the south (see Fig. 11). The cirrus to the north were in small patches at a variety of levels from 6.5 to 9 km in altitude. Light virga were observed. One large contrail appeared at 7.7 to 8.5 km altitude, 15 km south of the VIL (center point). A dense line of precipitating cirrus was also found 30 to 43 km south of the VIL. Later (1.25 hours) dense cirrus moved over the VIL (Fig. 12). A nearly continuous cloud from 6.5 to 9.3

km altitude was present within most of the range of the VIL. Some optically dense layers were found at 7 and 9 km.

To quantify the effects of cloud spatial variability on scanning method and FOV size, the backscatter measured by the VIL was vertically integrated from the series of slant angle scans in each cross section. Although the backscatter to extinction relationship may not be simple, we can assume that the backscatter is nearly linearly related to extinction for these optically thin clouds. The vertical integral of backscatter through the cloud is proportional to the optical depth of the cloud when the optical depth is small. The effect of this simplification is that the optical depth structural variations are most likely larger than the backscatter structural variations that are shown in Figures 13 and 14.

The cross wind scans were used to describe the areal structure of the cloud. Wind advection through each scan implied that the clouds were sampled at approximately 3 km intervals. Since the VIL cross sections have 100 m resolution along the scan, the cloud volume was sampled with a resolution of 0.1 x 3 km.

To estimate the effects of cloud structural variance on the averaged vertically integrated backscatter, two spatial averages were made. One average was made from the cross wind scans using wind advection to represent the satellite's spatial sampling. The other average was made from the along wind scans to represent the sampling of a vertically pointing lidar that uses wind advection for cloud sampling. Each average was constructed for simulated satellite FOV diameters of 1, 4, 8 and 20 km. The along wind scans have only the width of the lidar beam (<1 m) and thus the average is a line sample. The difference between these two averages of vertically integrated backscatter was used to approximate the sampling error between the satellite and stationary lidar sensors. This error is expressed as a fraction of the along wind lidar average in Figures 13 and 14. To estimate the possible error from mis-registration of the satellite image, the cross wind sampled segment was shifted from the center position of the VIL, see Figures 13 and 14.

The error between line and areal averaged measurements is the left most point in Figures 13 and 14. This error ranged from 5 to 29%. It was higher for the light and scatter cirrus simulating a 20 km FOV (Figs. 11 and 13) than the smaller simulated FOVs and the denser cirrus (Figs. 12 and 14). In the denser cirrus, the line vs. area sampling error ranged from 20 to 25 % (Fig 14).

The misalignment test shows that the area-line error increases with cross wind misalignment. The light cirrus (Fig. 13) have very large errors because of the spacing between cirrus features of 12-20 km and close alignment of the structures with the direction of the wind. The error or difference from the cross wind average often exceeded the along wind average (error > 100 %). These errors were smaller in the denser cirrus (Fig. 14). Operational satellites have typical image registration errors of 12 to 20 km. A 12 km misalignment when compared to a ground based sensor can cause an error of 50 % or greater. For larger FOV sizes of 8 and 20 km, this error decreases slightly. Because of this problem, special effort was made to align the satellite images to a one pixel accuracy.

## 5. DISCUSSION

In general, our observations of cirrus conformed to the expected relationship of the visible optical depth being twice the infrared optical depth. The scatter around the  $\tau_{\text{vis}}/\tau_{\text{ir}} = 2.0$  optical depth ratio mostly came from the differences between the lidar and satellite methods of probing the clouds. The high spatial variability of the clouds and the difficulty of evaluating small optical depths from satellite imagery were found to be the largest sources of error in this comparison. The thin line sampling of the HSRL vs. the areal scan of the satellite sensors could cause differences of 20-25% in measurements of the same variable. Any mis-registration of the location of the HSRL in the satellite image caused potentially larger errors and had to be corrected in this study. The initial evaluation of the HSRL and satellite data had more scatter than shown in Figure 2. This gave the impression that variations in cloud structure and microphysical content were

causing variations in the visible-infrared optical depth relationship. Re-analysis of the data with an intensive effort to remove location uncertainties reduced the scatter in Figure 2.

The satellite measurement of  $\tau_{ir}$  for optically thin clouds also had a bias because of the way in which the numerator of Equation 6 ( $T_{clr}^4 - T_{sat}^4$ ) was evaluated. This required a measurement of the difference between the clear and cloudy radiances in the satellite image. For optically thin clouds, variations in the underlying land surface were of nearly the same magnitude as ( $T_{cld} - T_{sat}$ ). The precision and noise characteristics of the satellite sensors require that the numerator terms in Equation 6 be at least 0.8 K different ( $T_{clr} - T_{sat} > 0.8K$ ) for the cloud to be distinguished on the satellite image. This forces a minimum of 0.03-0.05 for  $\tau_{ir}$ . Any error in the terms in Equation 6 from spatial variance tend to increase  $\tau_{ir}$  because errors that would reduce  $\tau_{ir}$  make cloud detection impossible. This is possibly why 7 of the 9 points in Figure 2 with  $\tau_{vis} < 1$  appear above the 2.0 line. It also indicates that the minimum optical depth (infrared) detectable in a satellite image is about 0.05.

Optically thin cirrus ( $\tau_{vis} < 1$ ) best conformed to the assumption made by most satellite cirrus cloud detection algorithms that cirrus clouds can be described as a single thin layer even though they span depths of 1-3 km. This assumption is possible when the clouds have little vertical variance in radiative properties.

For dense cirrus with optical depths  $\tau_{vis} > 1$  ( $\tau_{ir} > 0.5$ ), the cirrus were often over 3 km thick and in two or more layers. Vertical variations in optical density were common and liquid water layers were often present inside the ice clouds. The retrieval of a single cloud layer from the HIRS data to describe the infrared characteristics of these clouds appears to work as a first approximation of infrared divergence. More detail in the vertical would be helpful for the development of radiative transfer models. But the fact that the infrared optical depth calculated from the single cloud level solution followed the theoretical relationship of being nearly one half of the visible optical depth is very useful for inter-relating cloud climatologies. Development of radiative transfer algorithms for global numerical models requires global data sets on clouds and their radiative properties. Satellites are currently the best source of this data.

We found super cooled liquid water layers in 32% of the 48 cirrus cases measured by the HSRL which was more frequent than we expected. These case include an extra 25 days which were not analyzed with satellite data. This data set may not be large enough to state the frequency of liquid water in all cirrus clouds. The HSRL was operated mostly during NOAA 12 overpasses at dusk and after dusk. Cirrus data could only be obtained when obstructions from lower water clouds were not present or minimal enough to permit the view of the cirrus. Cirrus (ice clouds) obviously exist above low altitude liquid water clouds but we have little data from these cirrus because of low cloud obscurations.

## 6. CONCLUSIONS

The assumption of a single cloud level used by the satellite cloud climatologies is applicable to a large portion of the satellite data. The manner in which optical depths are calculated from the 10.8  $\mu\text{m}$  window channel measurements appears to approximate the vertically averaged optical depths for a variety of cloud structures which are far more complicated than one layer.

The cirrus climatologies derived from different satellite data, visible and infrared 10.8  $\mu\text{m}$  window, can be related using the 2.0 optical depth ratio to form longer records of cirrus cloud cover and describe inter-annual changes. This work is needed to asses the relationship of cirrus clouds to climatic changes and their role in the earth's heat budget. This study used clouds of visible optical depths ranging from 0.25 to 3.0. According to Wylie et al. (1994), these clouds cover 32% of the earth which is a significant part of the earth's cloud cover.

Super cooled liquid water layers are common inside ice clouds and can easily change the radiative characteristics of these clouds. They were found in nearly one third of our cirrus data. Their impact on radiative processes needs to be evaluated and models of radiative processes in clouds need to include them.

The problem of matching point or line sensors (lidars) to areal scanners (satellites) is an obstacle to field programs and the use of their data with global cloud climatologies. Miss-matches in sampling and scanning can lead to large errors when data sets are compared and these errors



can be mistaken for variances in radiative properties of the clouds. Scanning sensors and a large number of cases are needed from these field programs to define cloud radiative properties.

## 7. REFERENCES

- Ackerman, S. A., E. W. Eloranta, C. J. Grund, R. O. Knuteson, H. E. Revercomb, W. L. Smith and D. P. Wylie, 1993: University of Wisconsin Remote Sensing Pilot Experiment. Bull. A.M.S., **74**, 1041-1049.
- Dowling, D. R., and L. F. Radke, 1990: A summary of the physical properties of cirrus clouds., J. Appl. Meteor., **29**, 970-978.
- Grund, C. J. and E. W. Eloranta, 1991, University of Wisconsin high spectral resolution lidar., Optical Eng., **30**, 6-12.
- Hahn, C. J., C. S. Warren, J. London, R. M. Chervin and R. Jenne, 1982: Atlas of simultaneous occurrence of different cloud types over the oceans., NCAR Tech. Note NCAR TN-201+STR, National Center for Atmospheric Research, Boulder, CO, 212 pp.
- Klett, J. D., 1980: Stable analytical inversion solution for processing lidar returns., Appl. Optics, **20**, 211-220.
- Laio, X., W. B. Rossow, and D. Rind, 1994a: Comparison between SAGE II and ISCCP high-level clouds, Part I: Global and zonal mean cloud amounts., submitted to J. Geophys. Res.
- \_\_\_\_\_ b: Comparison between SAGE II and ISCCP high-level clouds, Part II: Locating cloud tops., submitted to J. Geophys. Res.
- Menzel, W. P., D. P. Wylie, and K. I. Strabala, 1992: Seasonal and diurnal changes in cirrus clouds as seen in four years of observations with the VAS., J. Appl. Meteor., **31**, 370-385.
- Minnis, P., D. F. Young, K. Sassen, J. M. Alvarez and C. J. Grund: 1990: The 27-28 October 1986 FIRE IFO Cirrus Case Study: Cirrus parameter relationships derived from satellite and lidar data., Mon. Wea. Rev., **118**, 2402-2425.
- Minnis, P., K. N. Liou and Y. Takano, 1993: Inference of cirrus cloud properties using satellite-observed visible and infrared radiances. Part I: Parameterization of radiance fields., J. Atm. Sci., **50**, 1279-1304.
- Mitchell, D. L. and W. P. Arnott, 1994: A model predicting the evolution of ice particle size spectra and radiative properties of cirrus clouds. Part II: Dependence of absorption and extinction on ice crystal morphology., J. Atm. Sci., **51**, 817-832.
- Paltridge, G. W., 1980: Cloud-radiation feedback to climate., Quart. J. R. Met. Soc., **106**, 895-899.
- Piironen, P. and E. W. Eloranta, 1994: Demonstration of high-spectral-resolution lidar based on an iodine absorption filter., Optics Letters, **19**, 234-236.

- Platt, C. M. R., 1979: Remote sounding of high clouds: I. Calculation of visible and infrared optical properties from lidar and radiometer measurements., J. of Appl. Meteor., **18**, 1130-1143.
- Rossow, W. B. and A. A. Lacis, 1990: Global and seasonal cloud variations from satellite radiance measurements. Part II: Cloud properties and radiative effects., J. Climate, **3**, 1204-1253.
- Rossow, W. B., and R. A. Schiffer, 1991: ISCCP cloud data products., Bull. Am. Meteor. Soc., **72**, 1-20.
- Schiffer, R. A., and W. B. Rossow, 1983: The International Cloud Climatology Project (ISCCP): The first project of the World Climate Research Programme., Bull. Am. Meteor. Soc., **64**, 779-784.
- Shiple, S. T., D. H. Tracy, E. W. Eloranta, J. T. Trauger, J. T. Sroga, F. L. Roesler, and J. A. Weinman, 1983: High spectral resolution lidar to measure optical scattering properties of atmospheric aerosols. 1: Theory and instrumentation., Applied Optics, **23**, 3716-3724.
- Stephens, G. L., S. C. Tsay, P. W. Stackhouse, and P. J. Flatau, 1990: The relevance of the microphysical and radiative properties of cirrus clouds to climate and climatic feedback., J. Atm. Sci., **47**, 1742-1753.
- Tselioudis, G., W. B. Rossow and D. Rind, 1992: Global Patterns of cloud optical thickness variation with temperature., J. of Climate, **5**, 1484-1497.
- Weare, B. C., 1992: Variations in Nimbus-7 cloud estimates. Part I: Zonal averages., J. Climate, **5**, 1496-1505.
- Wielicki, B. A., and J. A. Coakley, 1981: Cloud retrieval using infrared sounder data: Error analysis., J. Appl. Meteor., **20**, 157-169.
- Woodbury, G. E., and M. P. McCormick, 1983: Global distributions of cirrus clouds determined from SAGE data., Geophy. Res. Letters, **10**, 1180-1183.
- Wylie, D. P. and W. P. Menzel, 1989: Two years of cloud cover statistics using VAS. J. Clim. Appl. Meteor., **2**, 380-392.
- Wylie, D. P., W. P. Menzel, H. M. Woolf and K. I. Strabala, 1994: Four years of global cirrus cloud statistics using HIRS., J. Climate, in press.

**TABLE 1:** The dates and times of the satellite-lidar comparisons.

<u>Month/Date/Year</u>	<u>Time</u>	<u>Satellite</u>	
08/24/93	01:30 UTC	NOAA 12	Multiple layers
09/02/93	01:37	NOAA 12	Thin and variable
09/08/93	01:08	NOAA 12	Multiple layers
09/09/93	00:46	NOAA 12	Thick cirrus
10/02/93	00:51	NOAA 12	Thick cirrus
10/12/93	00:36	NOAA 12	Thin
10/25/93	00:57	NOAA 12	Thin and variable
10/26/93	00:35	NOAA 12	Uniform layer
10/28/93	01:32	NOAA 12	One thick layer
11/10/93	00:12	NOAA 12	Two layers
11/11/93	01:31	NOAA 12	Two layers
02/04/94	00:06, 00:36, 01:06 and 01:36	GOES	One thick layer
02/15/94	01:06	GOES	Thin layer
02/17/94	01:06	GOES	Thin layer
03/04/94	01:06	GOES	Thin layer
03/08/94	01:09	NOAA 12	Two layers
03/17/94	01:09	GOES	Thin layer
03/26/94	00:06, 00:36, 01:06 and 01:36	GOES	Thick layer
04/07/94	00:22	NOAA 12	Thin layer
04/11/94	00:36	NOAA 12	Thick layer
04/15/94	00:49	NOAA 12	Two layers

## LIST OF FIGURES

Figure 1: The physical thickness vs. the visible optical depth of semi-transparent clouds observed by the HSRL in 1993 and 1994.

Figure 2: Scatter plot of the visible and infrared optical depths measured by the combination of the HSRL lidar (visible optical depth at  $0.53 \mu\text{m}$ ) and NOAA and GOES satellite data (infrared  $10.8 \mu\text{m}$  window channel). The diagonal line is a ratio of 2.0 (visible/IR). Error bars are shown on each data point.

Figure 3: Time-height image of the backscatter cross section  $\beta_a(r) \frac{P(\pi,r)}{4\pi}$  (see Eq. 2) from the HSRL (upper panel). The lower panel is the visible optical depth integrated from 8.5 to 12 km altitude on 26 October 1993.

Figure 4: NOAA 12 1 km HRPT image from AVHRR Channel 4 ( $10.8 \mu\text{m}$ ) from 26 October 1993. This image was remapped into an equal distant latitude-longitude projection. The location of the HSRL is indicated by the black dot.

Figure 5: Time-height image of the backscatter cross section  $\beta_a(r) \frac{P(\pi,r)}{4\pi}$  (see Eq. 2) from the HSRL (upper panel). The lower panel is the visible optical depth integrated from 4 to 10 km altitude on 11 November, 1993. The extremely white layers between 5 and 5.5 km were liquid water as determined from depolarization measurements (not shown).

Figure 6: NOAA 12 1 km HRPT image from AVHRR Channel 4 ( $10.8 \mu\text{m}$ ) from 11 November 1993. This image was remapped into an equal distant latitude-longitude projection. The location of the HSRL is indicated by the black dot.

Figure 7: Time-height image of the backscatter cross section  $\beta_a(r) \frac{P(\pi,r)}{4\pi}$  (see Eq. 2) from the HSRL (upper panel). The lower panel is the visible optical depth integrated from 7 to 11 km altitude on 2 September, 1993.

Figure 8: NOAA 12 AVHRR Channel 4 infrared image from 2 September, 1993.

Figure 9: Time-height image of the backscatter cross section  $\beta_a(r) \frac{P(\pi,r)}{4\pi}$  (see Eq. 2) from the HSRL (upper panel). The lower panel is the visible optical depth integrated from 3.5 to 11 km altitude on 15 April, 1994.

Figure 10: NOAA 12 AVHRR Channel 4 infrared image from 15 April, 1994.

Figure 11: The cross wind (top panel) and along the wind (bottom panel) images of range corrected backscatter from the Volume Imaging Lidar for 19:50 UT (13:50 CST) on 1 December 1989 at Madison, WI.

Figure 12: Same as Fig. 11 for 20:07 UT (15:07 CST) on 1 December 1989.

Figure 13: Error or difference in vertically integrated backscatter for an area vs. a line average, plotted as a function of separation distance between the locations of the area and line averaged volumes for the period of 19:30 to 20:30 UT, 1 December, 1989.

Figure 14: Same as Fig. 12 for the period, 20:30 to 21:30 UT, 1 December, 1989.

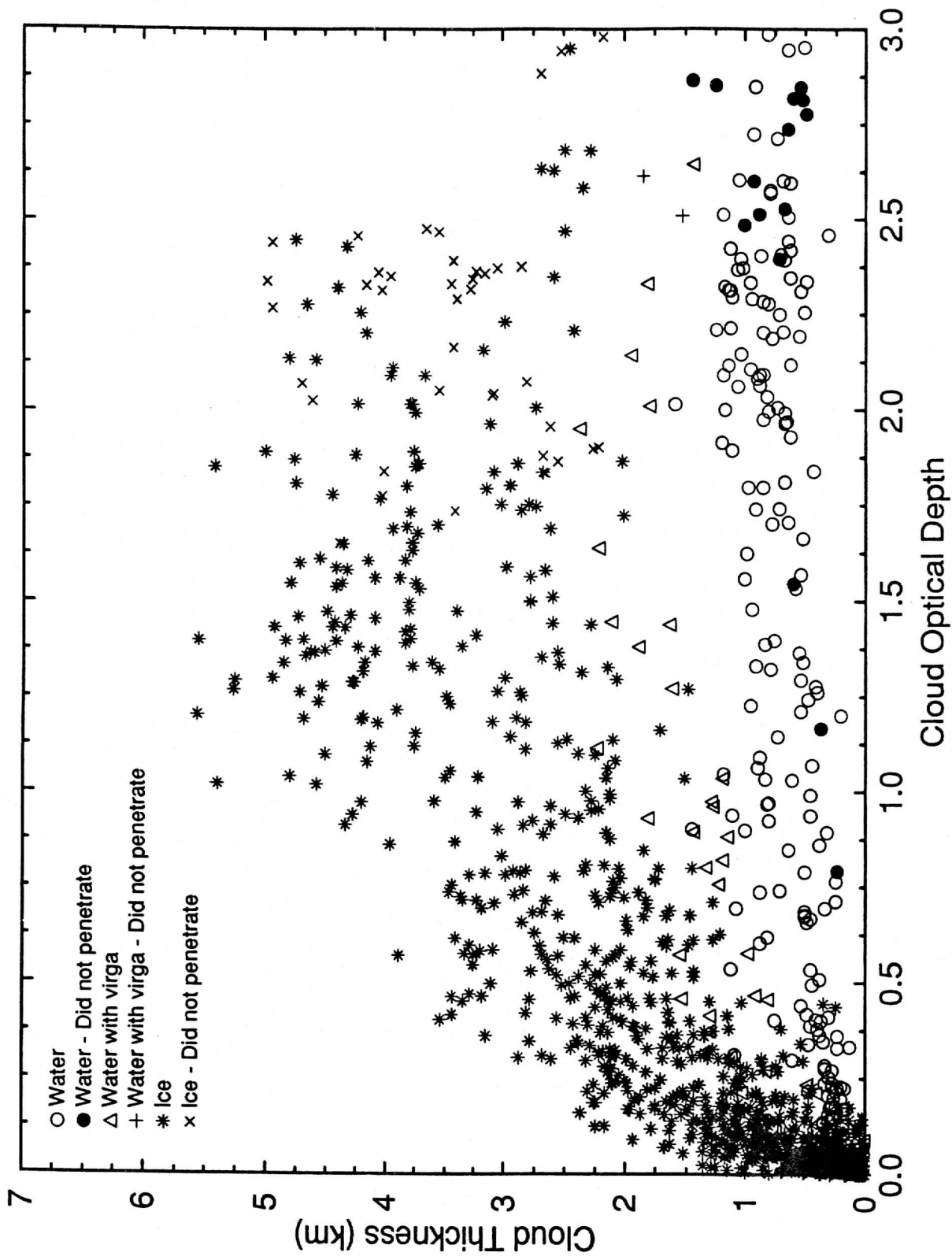


Figure 1: The physical thickness vs. the visible optical depth of semi-transparent clouds observed by the HSRL in 1993 and 1994.

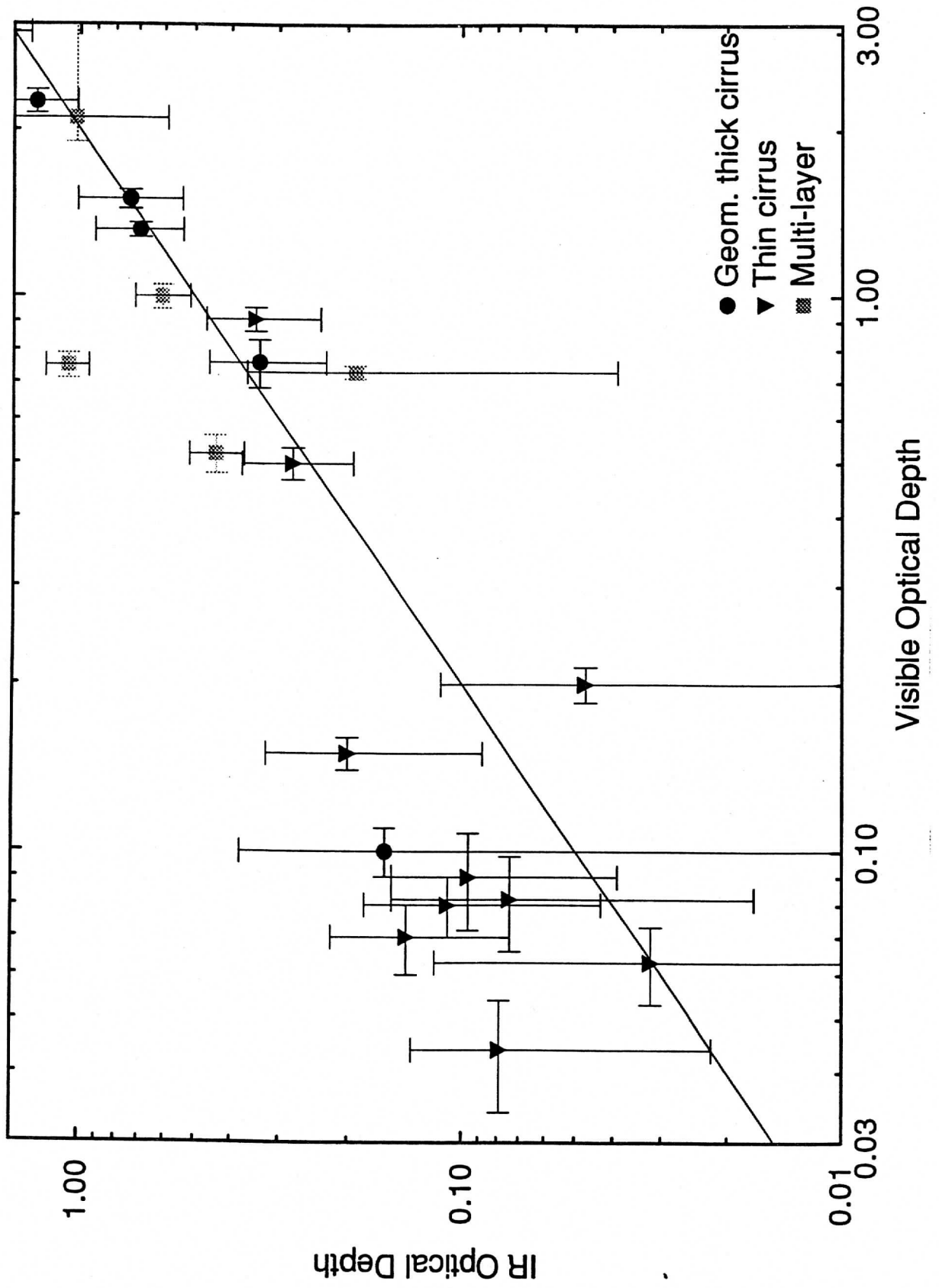


Figure 2: Scatter plot of the visible and infrared optical depths measured by the combination of the HSRL lidar (visible optical depth) and NOAA and GOES satellite data (infrared 10.8  $\mu\text{m}$  window channel). The diagonal line is a ratio of 2.0 (satellite/IR) to 1.0 (lidar/IR).

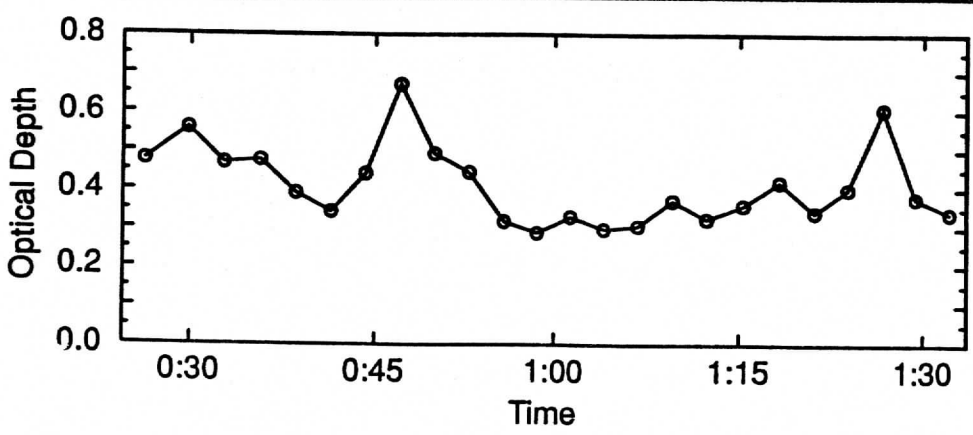
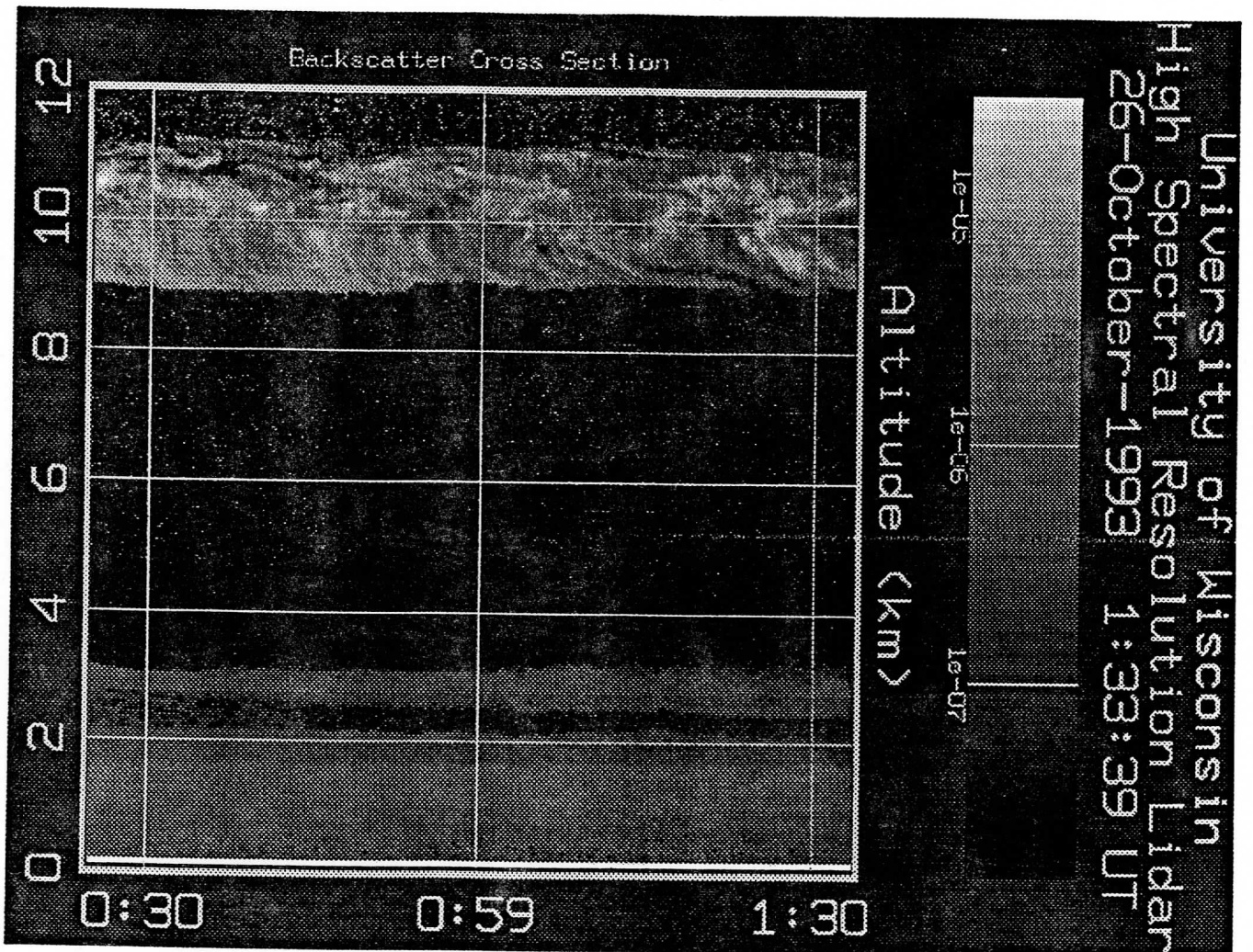


Figure 3: Time-height cross section of backscatter (upper panel) and visible optical depths between 8.5 and 12 km (lower panel) from the HSRL on 26 October 1993.



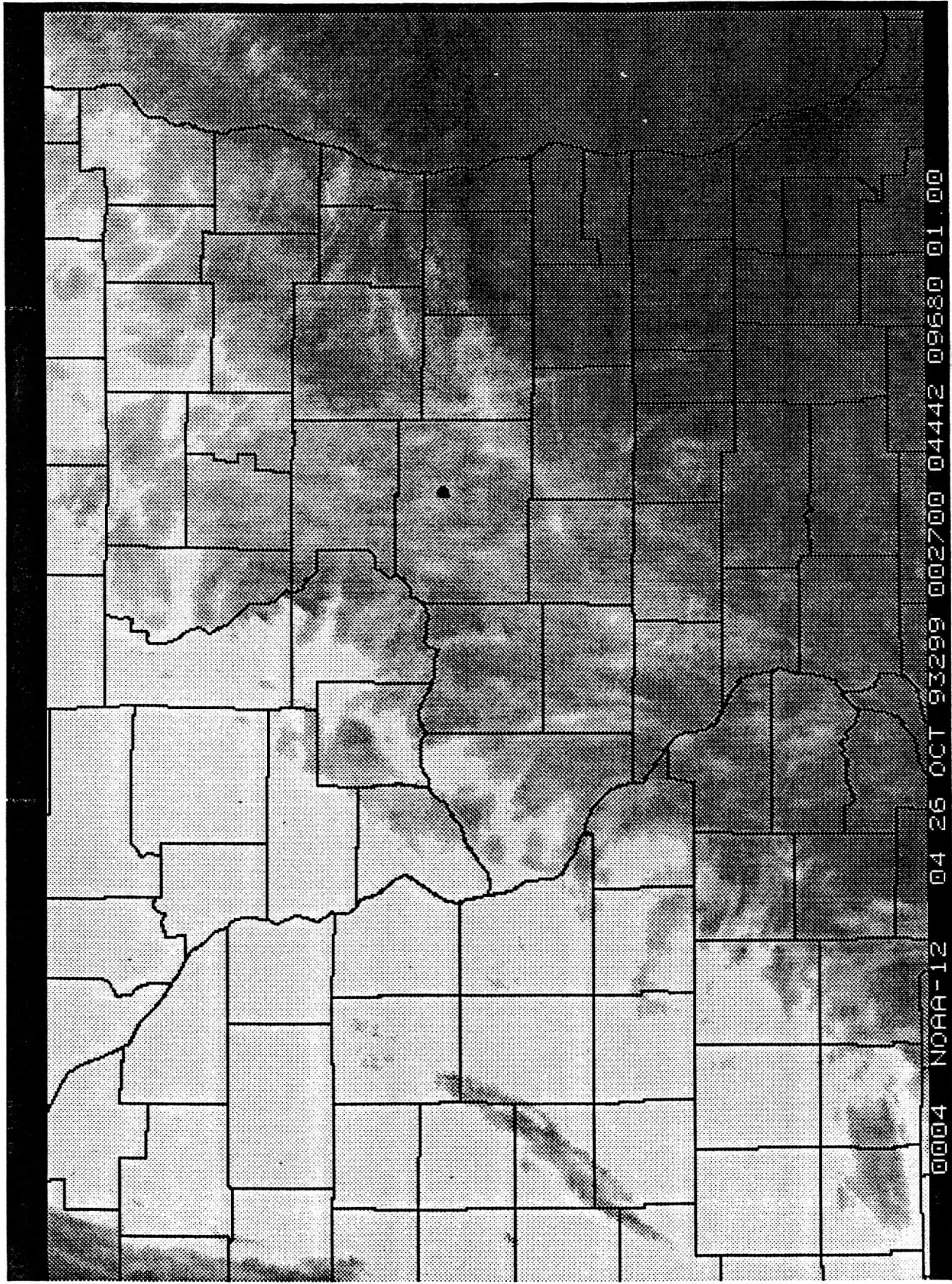


Figure 4: NOAA 12 1 km HRPT image from AVHRR Channel 4 (10.8  $\mu\text{m}$ ) from 26 October 1993. This image was remapped into an equal distant latitude-longitude projection. The location of the HSRL is indicated by the black dot.

University of Wisconsin  
High Spectral Resolution Lidar

11-November-1993 2:13:05 UT

3:28-05 1e-05 3:28-05 1e-05 3:28-07 1e-07

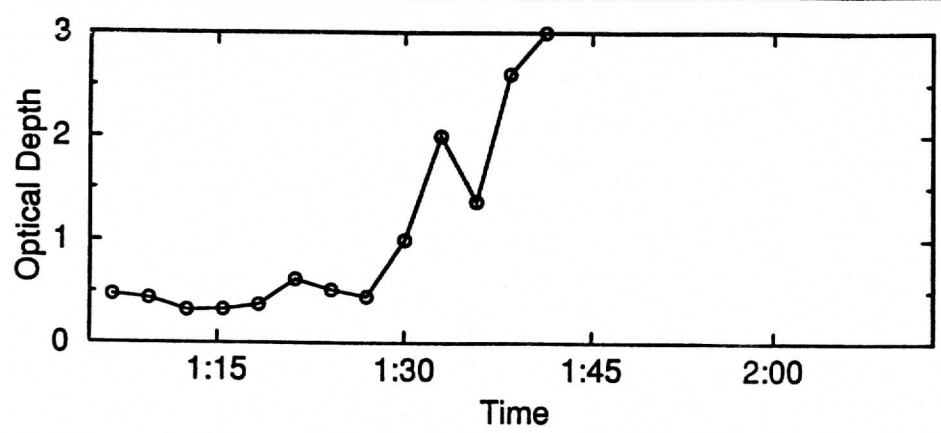
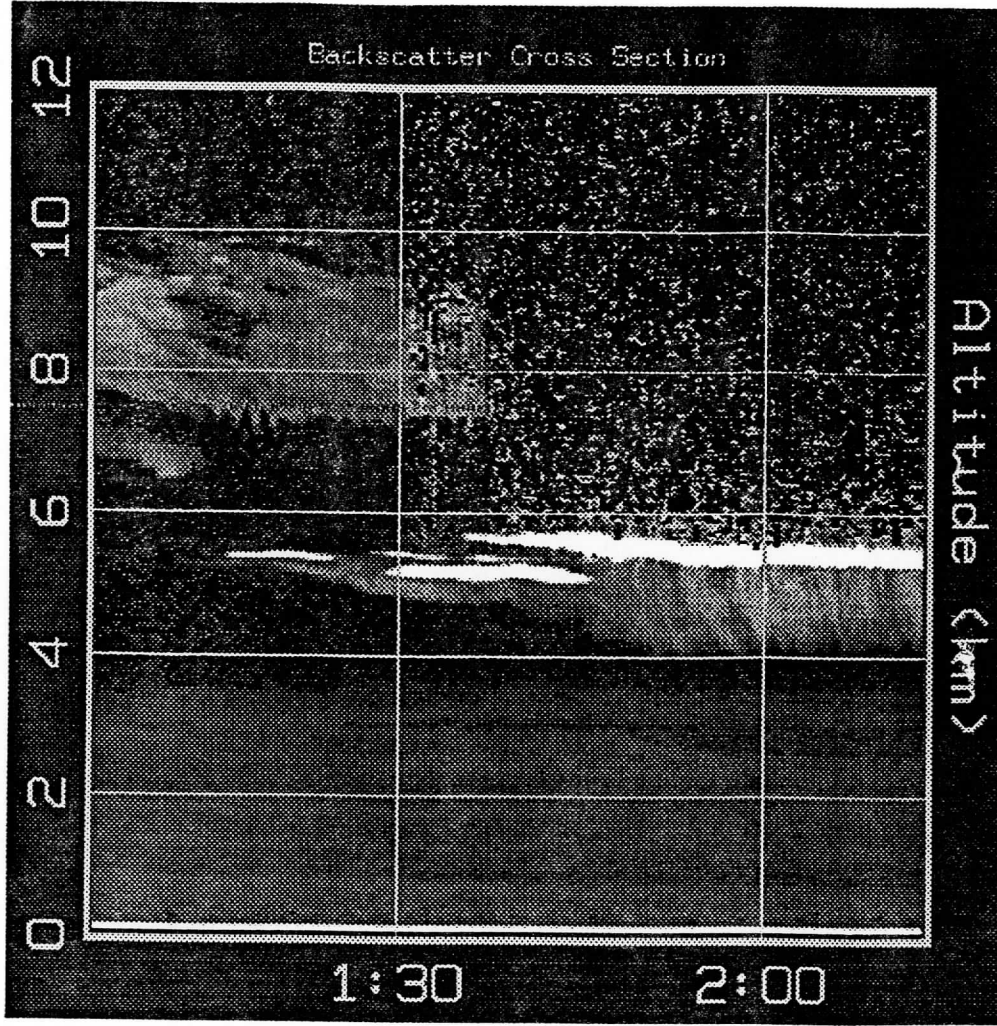


Figure 5: Time-height cross section of backscatter (upper panel) and visible optical depth between 4 and 10 km from the HSRL on 11 November 1993. The extremely white layers between 5 and 5.5 km were liquid water as determined from depolarization measurements (not shown).

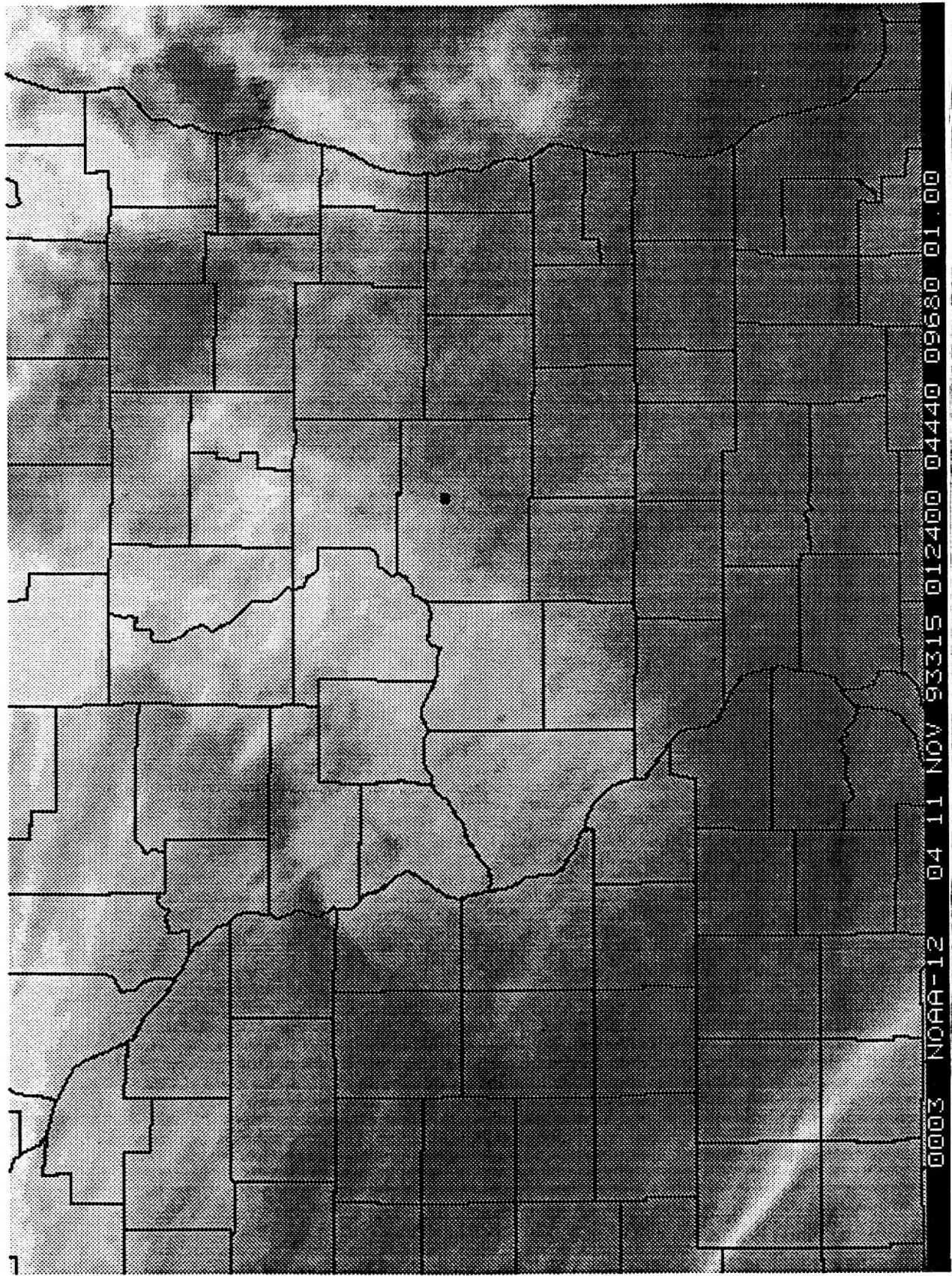


Figure 6: NOAA 12 1 km HRPT image from AVHRR Channel 4 (10.8  $\mu\text{m}$ ) from 11 November 1993. This image was remapped into an equal distant latitude-longitude projection. The location of the HSRL is indicated by the black dot.

University of Wisconsin  
High Spectral Resolution Lidar  
2-September-1993 3:04:17 UT

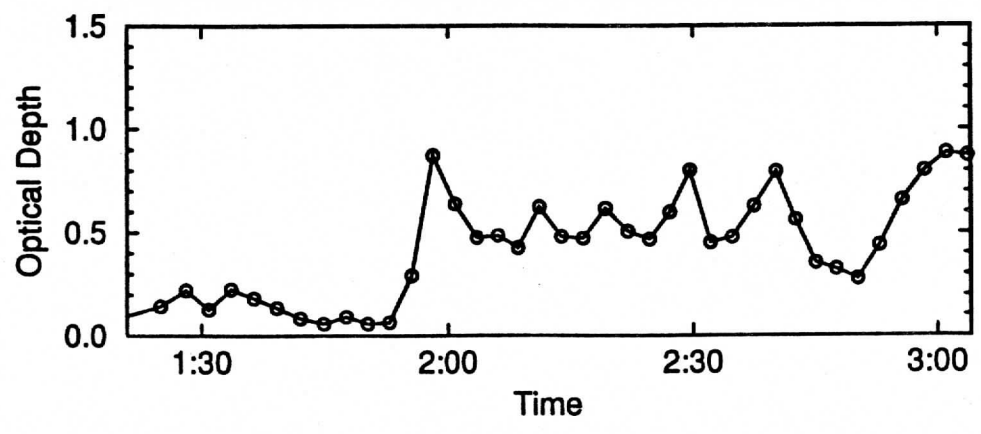
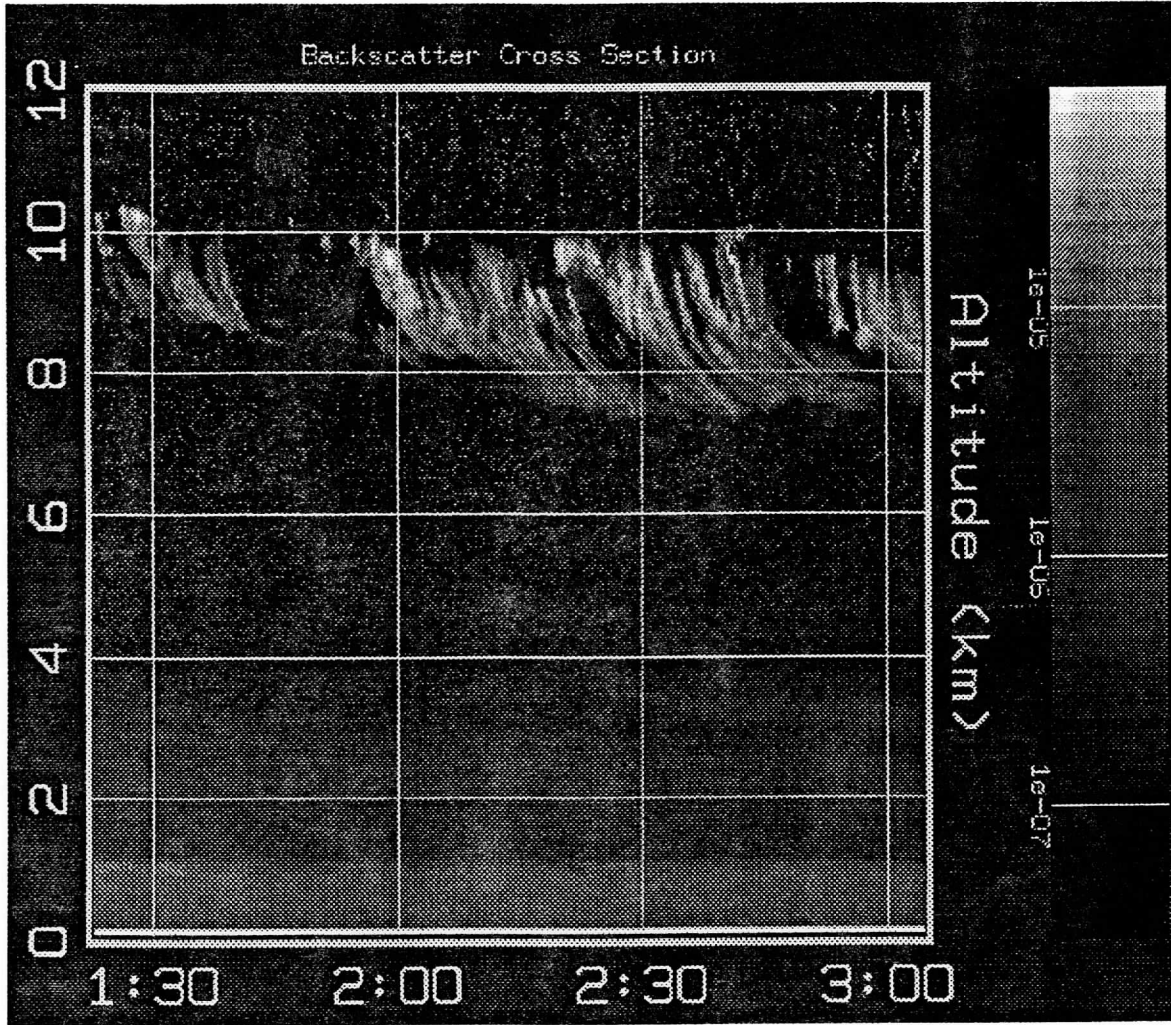


Figure 7: Time-height cross section of backscatter (upper panel) and visible optical depth between 7 and 11 km (lower panel) from 2 September, 1993, measured by the HSRL.

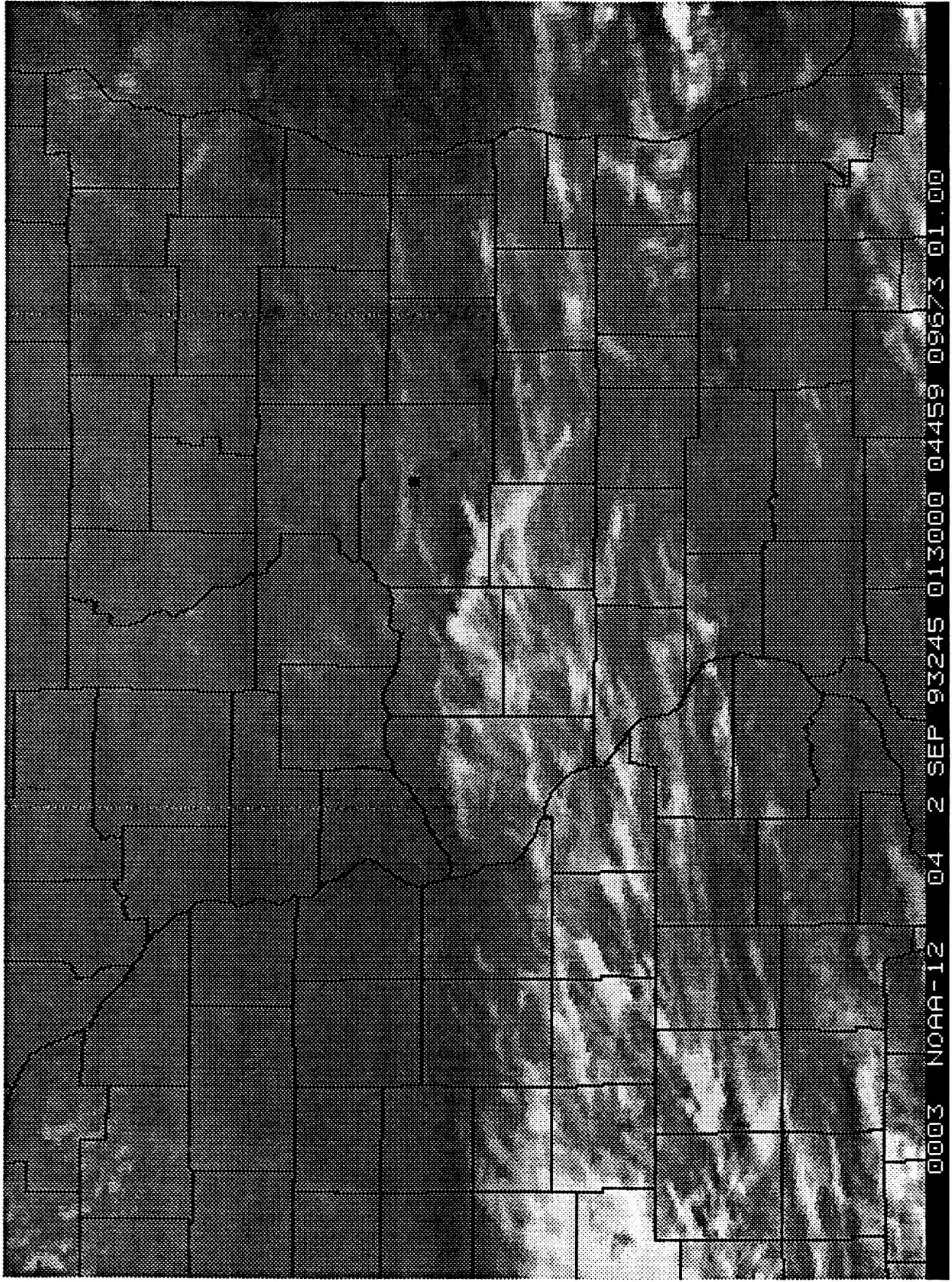


Figure 8: NOAA 12 AVHRR Channel 4 infrared image from 2 September, 1993.

University of Wisconsin in  
High Spectral Resolution Lidar  
15-April-1994 2:23:28 UT

Altitude (km)

5.28-05 1e-05 3.28-05 1e-05 3.28-07

Backscatter Cross Section

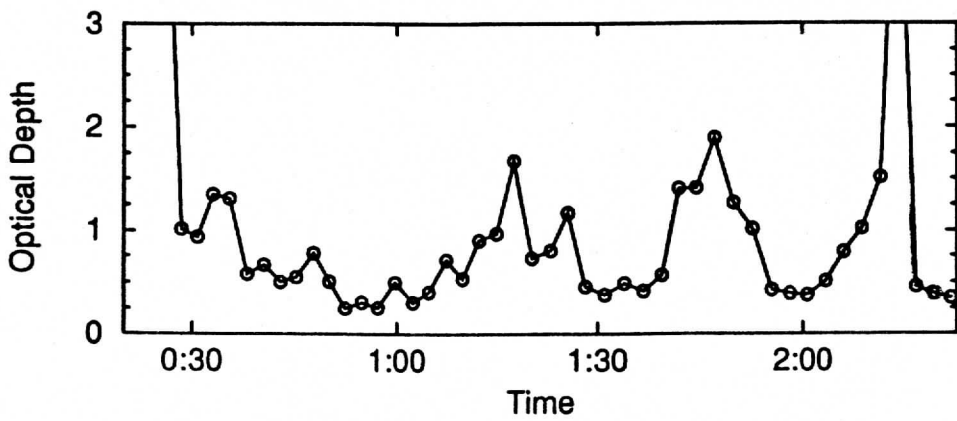
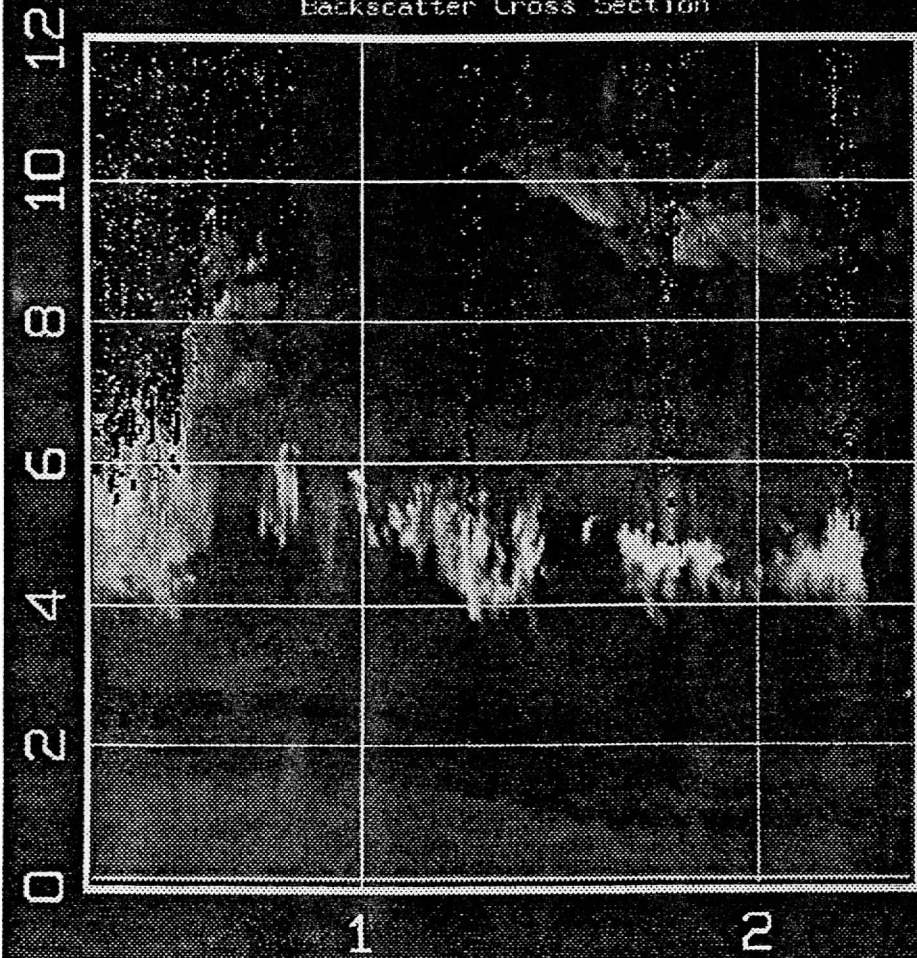


Figure 9: Time-height cross section of backscatter (upper panel) and visible optical depth between 3.5 and 11 km (lower panel) from 15 April, 1994, measured by the HSRL.

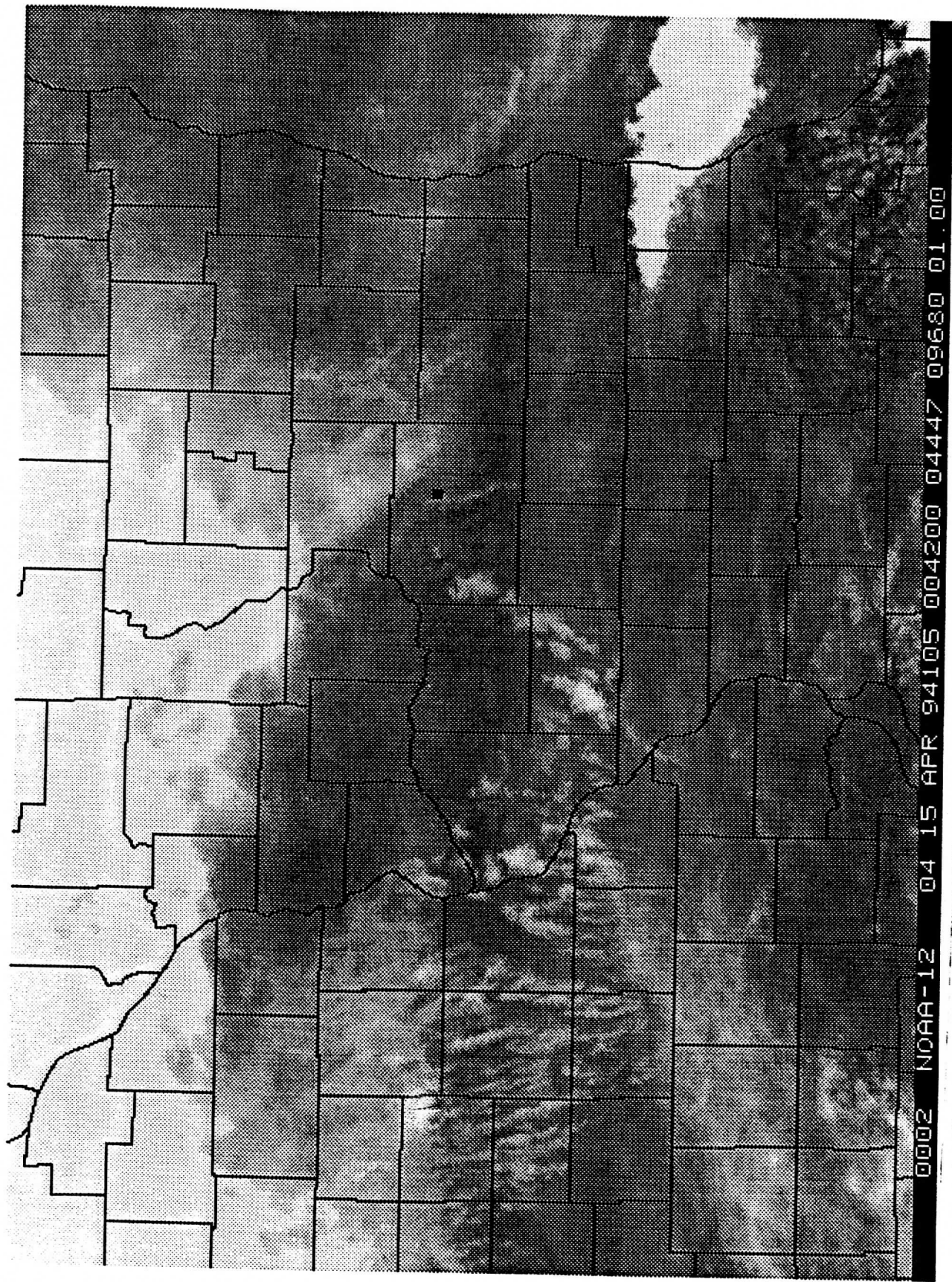


Figure 10: NOAA 12 AVHRR Channel 4 infrared image from 15 April, 1994.

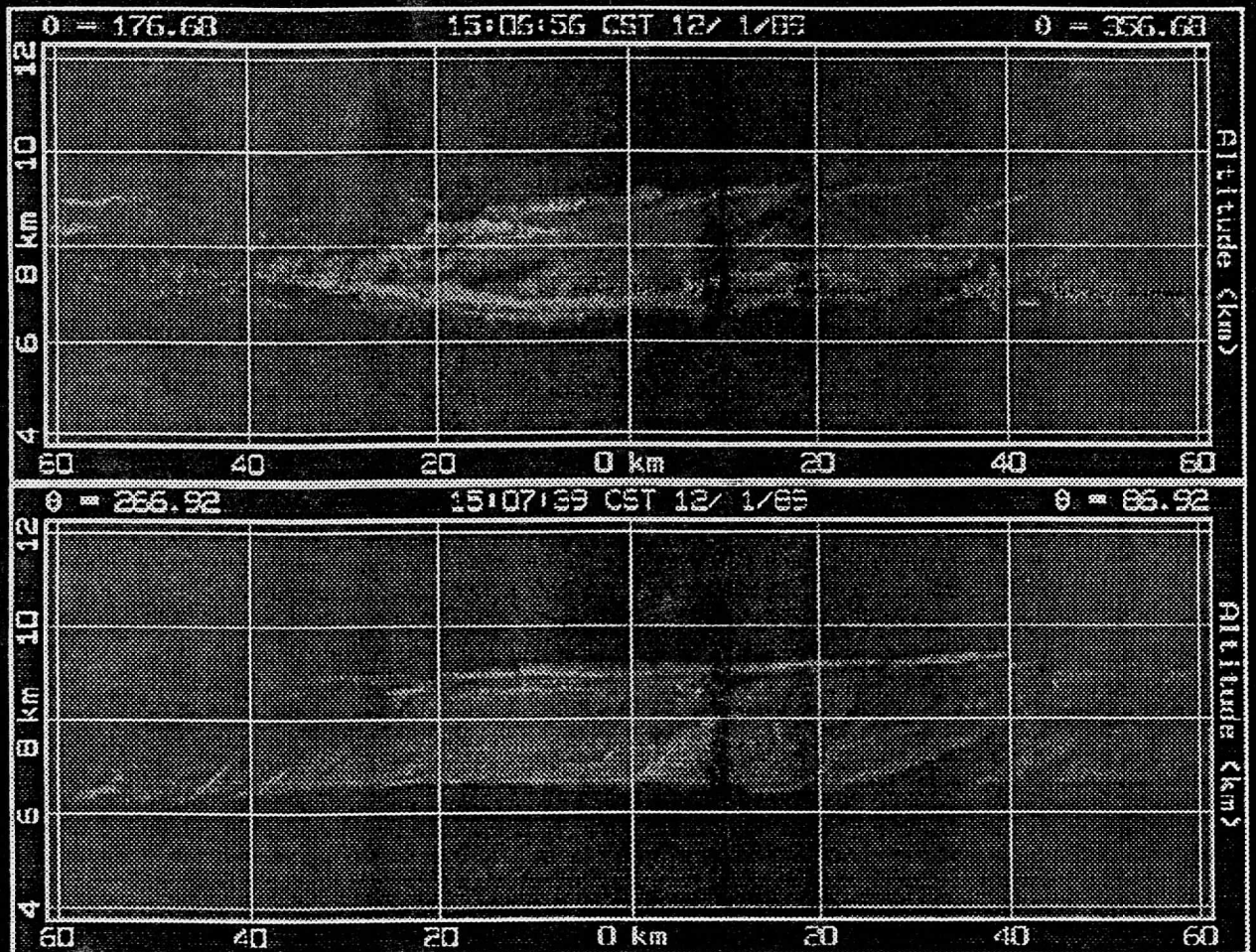


Figure 12: Cross wind (top panel) and along the wind (bottom panel) cross sections from the Volume Imaging Lidar backscatter data at 20:07 UT (15:07 CST) on 1 December 1989.



# Line Average vs. Area Average

December 1, 1989 (19:29 - 20:25 GMT)

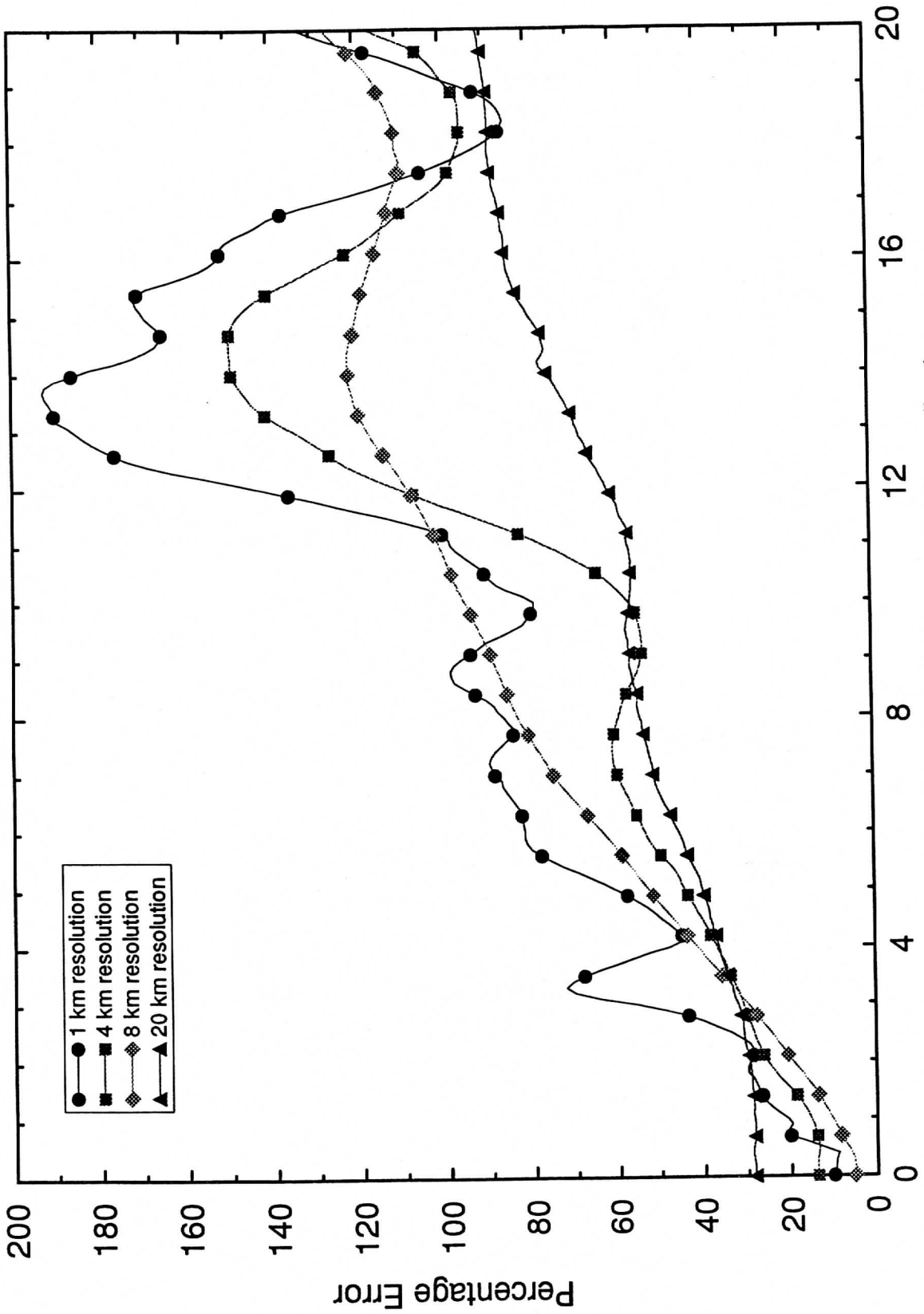


Figure 13: Error or difference in vertically integrated backscatter averages for an areal vs. a line average plotted as a function of separation distance (Along Wind Navigation Misalignment) in the clear the wind direction for the period of 19:30 to 20:30 U.T. 1 December, 1989.

# Line Average vs. Area Average

December 1, 1989 (20:25 - 21:20 GMT)

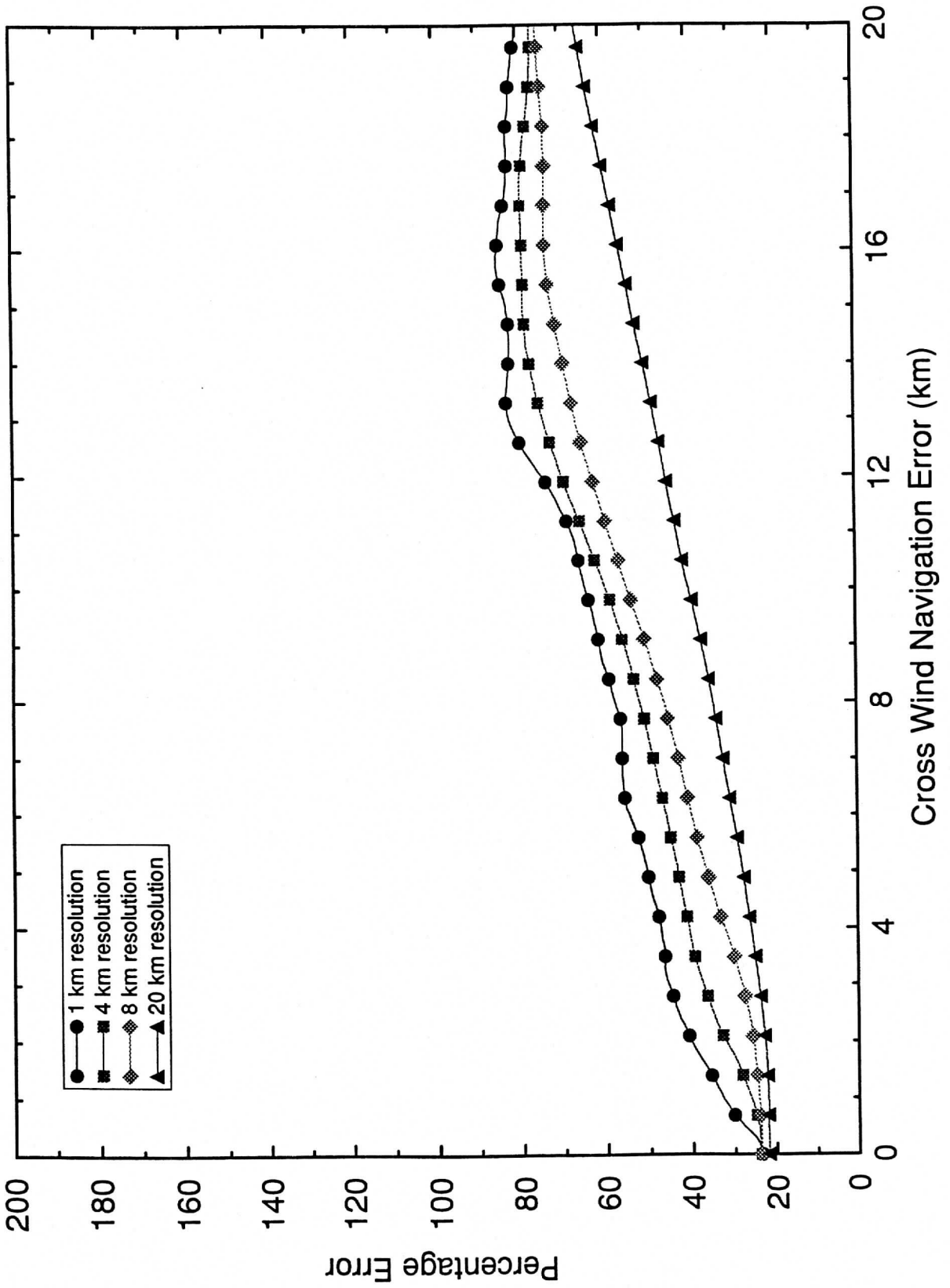


Figure 14: Same as Fig. 12 for the period, 20:30 to 21:30 UT, 1 December, 1989.